Fallpipe dispersion model for subsea stone installation

Carried out for 'Great Lakes Dredge & Dock Company, LLC'

T.K.F.J. Hogenhuis

Thesis report

TU Delft

This page has been intentionally left blank

Fall Pipe Dispersion Model

Master thesis

by

T.K.F.J. Hogenhuis

Master of Science
to obtain the degree of Master of Science
in Offshore & Dredging Engineering at the Delft University of Technology,
to be defended publicly on
September 20, 2023 at 15.00

Student number:	4370392	
Project duration:	September 6, 2022 – September 20, 2023	
Graduation committee:	Prof.dr.ir. Cees van Rhee	TU Delft, Supervisor
	Dr.ir. Geert Keetels	TU Delft, Supervisor
	Dr. ir. Said Alhaddad	TU Delft
	Michael Beton	GLDD

An electronic version of this thesis is available at `http://repository.tudelft.nl/`.

GREAT LAKES DREDGE & DOCK COMPANY, LLC

TU Delft

This page has been intentionally left blank

Preface

This graduation thesis was conducted at Delft University of Technology as part of the Offshore & Dredging Engineering master's program. The research involved a comprehensive literature review and the development of a model in collaboration with Great Lakes Dredge Dock Corporation. The model was created using various software tools, including Matlab, OpenFOAM, and SALOME.

I would like to express my sincere appreciation to Prof. Dr. Ir. Cees van Rhee and Dr. Ir. Geert Keetels, my supervisors from TU Delft, for their guidance and support throughout my thesis research. Their valuable feedback and constructive criticism have played a crucial role in refining this thesis to its final form. I am truly grateful for their mentorship and academic assistance.

I would also like to extend my appreciation to Michael Beton, my supervisor from Great Lakes Dredge & Dock, for his exceptional dedication, continuous guidance, and insightful discussions. His extensive expertise and experience in the dredging field have been very helpful in the successful completion of this thesis. I deeply appreciate his valuable contributions to this research.

I would like to acknowledge the strong interest demonstrated by GLDD in my project and their ongoing support. Their collaborative spirit and commitment to advancing the offshore wind industry are truly commendable, and I consider it a privilege to have collaborated with them.

Lastly, I want to express my gratitude to my friends and family for their unwavering support and encouragement. Their belief in my capabilities has been a constant source of motivation throughout this journey. I am deeply grateful for their understanding and patience during the demanding phases of my research.

Thank you for taking the time to read this preface. I invite you to delve into the subsequent chapters of this thesis, where you will find detailed discussions on the research methodology, analysis, and findings. It is my sincere hope that this work contributes meaningfully to the academic discourse in this field.

August 29, 2023

Tim Hogenhuis

Abstract

The development of a US Flagged stone installation vessel with an inclined fall pipe by Great Lakes Dredge & Dock Corporation marks a significant step in advancing the future of the US offshore wind industry. Subsea stone installation plays a crucial role in protecting offshore structures and pipelines from scour. To support this project, new engineering and physics-based production models need to be developed, enabling more accurate estimation and baseline expectations for future operations.

This thesis aims to enhance the understanding of stone dispersion during subsea stone installation. Specifically, a physics-based model is designed to describe the trajectories of stones after they exit a diagonal fallpipe. In order to accurately reflect stone dispersion, the model integrates the influence of the lift force, induced by vortex shedding, and the influence of turbulence present in the fluid field.

The model allows for the calculation of stone distribution on the seabed under various conditions, including the presence of ambient ocean currents or nearby obstacles. The model is validated by comparing it to small-scale laboratory experiments, which provide promising validation results. However, further research is necessary to validate the model on a larger scale, as fluid simulations at a small scale tend to exhibit more laminar behavior in comparison to larger-scale scenarios, and the availability of experimental data for validation is limited.

Additionally, the research highlights the sensitivity of the resulting seabed distribution to the initial conditions and external factors, such as ambient currents or the presence of a monopile, which can significantly influence the flow, resulting in a changing dispersion pattern. Despite the large sensitivity, the developed model shows promising accuracy in estimating stone dispersion.

Overall, the findings of this research provide valuable insights into the dispersion of stones during subsea stone installation. By enhancing our understanding of stone dispersion, this study contributes to the development of more accurate dispersion models and supports the advancement of the US offshore wind industry.

List of Figures

List of Tables

Nomenclature

Greek variables ..

α	Percentage of the equilibrium fall velocity	[%]
α_s	Angle of the current with respect to the longitudinal axis of the ship	$[rad]$
β	Bed angle	$[rad]$
β_{height}	Bed height	$[m]$
Δ	Relative density	$[-]$
Δr	Horizontal displacement of a stone relative to the mean of the stone group	$[m]$
κ	Shape factor	$[-]$
μ	Kinematic viscosity of fluid	$[m^2/s]$
μ_t	Eddie viscosity	$[m^2/s]$
$\mu_{C_D,n}$	Mean drag coefficient	$[-]$
ν	Shape factor	$[-]$
ω	Radial frequency	$[1/s]$
ϕ	Falling angle	$[rad]$
ρ	Density	$[kg/m^3]$
ρ_f	Fluid density	$[kg/m^3]$
ρ_s	Density of the stone	$[kg/m^3]$
ρ_w	Density of the water	$[kg/m^3]$
σ	Standard deviation	$[-]$
$\sigma_{C_D,n}$	Mean standard deviation	$[-]$
τ	Particle relaxation time	$[s]$
τ_e	Characteristic lifetime of an eddy	$[s]$
θ_{pipe}	Angle of the fallpipe	$[Degrees]$
ε	Turbulent dissipation rate	$[m^2/s^3]$
ξ	Shape factor	$[-]$
ζ	Shape factor	$[-]$

Roman variables

a	Acceleration	$[m/s^2]$
A_L	Reference area	$[m^2]$
A_s	Frontal area of the stone facing the flow direction	$[m^2]$
C_D	Drag coefficient	$[-]$
C_L	Lift coefficient	$[-]$
c_v	Volumetric concentration	[%]
CoR	Coefficient of Restitution	$[-]$
D	Diameter	$[m]$
d	Minimum distance between two points	$[m]$
D_n	Nominal diameter	$[m]$
D_s	Equivalent sphere diameter	$[m]$
D_{n50}	50% Nominal diameter	$[m]$
F_b	Buoyancy force	$[N]$
F_d	Drag force	$[N]$
F_g	Gravitational force	$[N]$
F_L	Lift force	$[N]$
g	Gravitational constant	$[m/s^2]$
h	Water depth	$[m]$
I	Turbulence intensity	[%]
k	Turbulent kinetic energy	$[m^2/s^2]$

L	Maximum distance between two points	$[m]$
l_e	Eddie length scale	$[m]$
l_m	Mixing length	$[m]$
M	Mass	$[kg]$
M_a	Added mass	$[kg]$
N	Number of directional changes	$[-]$
n	Current time step	$[-]$
n_{HS}	Hindered settling exponent	$[-]$
P	Production	$[kg/s]$
Re	Reynolds number	$[-]$
$s_{\Downarrow}$	Vertical distance traveled	$[-]$
St	Strouhal Number	$[-]$
T	Period of separation of vortices	$[m/s]$
t	Time	$[s]$
T_L	Fluid Lagrangian integral time	$[s]$
t_{cross}	Particle eddie crossing time	$[s]$
U	Relative velocity	$[m/s]$
u'	Gaussian distributed random fluctuating velocity	$[m/s]$
$u_{current}$	Velocity of the current	$[m/s]$
u_{exit}	Exit velocity of the stone at the fallpipe	$[m/s]$
u_{f_x}	Horizontal velocity component of the fluid in x direction	$[m/s]$
u_{f_y}	Horizontal velocity component of the fluid in y direction	$[m/s]$
u_{ref}	Reference flow speed	$[m/s]$
u_{s_x}	Horizontal velocity component of the stone in x direction	$[m/s]$
u_{s_y}	Horizontal velocity component of the stone in y direction	$[m/s]$
u_{SSM}	Velocity component introduced by the SSM model	$[m/s]$
u_s	Velocity of the stone	$[m/s]$
u_w	Velocity of the water	$[m/s]$
V	Volume	$[m^3]$
v_f	Vertical velocity of the fluid	$[m/s]$
v_s	Vertical velocity component of the stone	$[m/s]$
w	Terminal velocity (equilibrium fall velocity)	$[m/s]$
w_s	Hindered settling velocity	$[m/s]$
x	Depth at which the α% of the equilibrium fall velocity is achieved	$[m]$
x_s	Coordinate of the stone in x direction	$[m]$
y_s	Coordinate of the stone in y direction	$[m]$
z_s	Coordinate of the stone in z direction	$[m]$

Table of Contents

1 Introduction

1.1. Background

Whenever a structure is placed offshore in an area with loose soil, scour must be considered. Over the last few decades, there has been a considerable amount of research conducted on the phenomenon of scour around piles in steady currents. This research has led to a relatively well-developed understanding of the fluid mechanics involved in scour. The formation of a horseshoe vortex around the pile just above the bed has a large influence on the scouring process (Sumer et al. 1992). This vortex is created due to the rotation present in the incoming velocity profile and is capable of eroding a significant amount of sediment from the vicinity of the pile. Due to the eroding of the particles around the structure, as can be seen in Figure 1.1, a structure can become unstable. This has to be avoided at all costs.

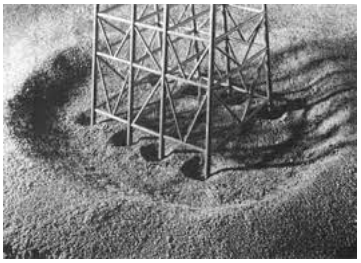

Figure 1.1: Example of scour around a jacket structure

To protect a structure from scour or other types of erosion on the seabed (Zhai & Christensen, 2022), different stone layers can be placed on top of the seabed to prevent the seabed from eroding. Placing stone layers as a protection measure is often used, for instance, for the construction of breakwaters or subsea pipeline protection. The stones can then be installed using different stone installation methods. The focus of this research will be on a vessel with a changeable angle fallpipe. Stone dispersion during subsea stone installation has previously been researched using probabilistic methods and experiments by Konter (1983), Slack (1963), De Reus (2004), Cregten (1995), Manni and Vrijling (1995), Kevelam (2016) and others. However, installing the stone using an inclined fallpipe under an angle has not been researched before. While installing the stones on the seabed a minimum layer thickness is required to maintain the stability of the stone layer. Preferably this layer thickness is uniform and shouldn't contain too many irregularities, which occur when the layer thickness is below the appropriate level. If, during installation, the stones are not deposited evenly, the layer thickness may not be uniform. Therefore additional material is frequently deposited, which would require more material and is cost- and time-wise inefficient.

1.2. Problem statement

Great Lakes Dredge & Dock Corporation has announced that it is moving forward with the design and development of the first US Flagged inclined fall pipe vessel for subsea stone installation. This vessel represents an advancement in building the future of the new U.S. offshore wind industry. With GLDD's decision to move into the offshore wind industry, several technical engineering challenges must be overcome. For the vessel, new engineering and physics-based production models need to be developed. The development of these models will allow for more accurate estimating and baseline expectations for future operations. The models required follow from the installation process which can be divided into three independent processes (De Vos, 2004):

1. The process of loading the stones from the loading deck into the fallpipe until the stones exit the pipe.
2. The falling behavior of the stones as they travel through the water.
3. The behavior of the stones after they hit the seabed.

The first process establishes what kind of flow occurs inside the pipe, based on this the bed height, concentration and the velocity of the stones can be calculated (Vehmeijer, 2022). The second process determines where the stone will end up on the seabed by studying the dispersion of the stones during their fall after they have exited the pipe, and the third process considers the seabed displacement and settlement interaction. This year a dispersion model has to be developed based on the second process for the accurate placement of stones.

1.3. Objectives

The objective of this thesis is to gain more insight into the physics of the falling behavior of stone groups in water and to create a physics-based dispersion model. The model will consist of a combination of a turbulence model and a model based on the Single Stone Model by Manni and Vrijling (1995) and uses a Monte Carlo-like approach, where a large number of random walks are used to provide an approximation of the final solution. The turbulence model uses a Discrete Random Walk approach, as described by ANSYS, INC. (2021), where random fluctuating velocity components are added to the mean velocity components of the stone. These fluctuating velocity components are calculated based on the turbulent characteristics, namely the turbulent kinetic energy and the turbulent dissipation rate, present in the fluid field. The model based on The Single Stone Model calculates a fluctuating horizontal velocity component resulting from the lift force induced by vortex shedding to determine the fall trajectory of the stone. As a result, it is a computational model used to study the movement of individual stones in water. It considers factors such as stone size, water depth, and lift force to predict the stone's trajectory and final resting position.

The combined model will be used to model stone dispersion with different circumstances, such as a varying ambient current or the presence of obstacles nearby altering the flow. It will be used to create a benchmark for future operations by GLDD's first stone installation vessel. Consequently, the main research question of this thesis is defined as:

How to model the dispersion of stones using a diagonal fallpipe during subsea stone installation?

Due to the dispersion being influenced by many different variables and processes and to be able to create a physics-based model, the main research question is divided into several sub-questions. The following list presents these sub-questions:

1. What is the influence of the initial parameters used in the model, such as the angle of the fallpipe, the bed height, or the stone characteristics on the dispersion?

2. How does the lift force, induced by vortex shedding, affect the trajectory of stones as they exit the fallpipe during subsea stone installation?
3. What is the influence of the forces acting on a stone, as a result of turbulence in the fluid field, on the stones' trajectory and the dispersion?
4. Does the combined model, which is based on the Single Stone Model and turbulence model, accurately represent the dispersion of stones in real-world subsea stone installation scenarios?
5. What is the effect of nearby obstacles, such as a monopile, on the ambient flow, and, consequently, on the dispersion pattern of stones after they exit the fallpipe?
6. How do ambient ocean currents impact the dispersion of stones on the seabed during subsea installations?
7. Is the model scalable?

To increase the predictability of the stone dispersion, it is important to analyze and comprehend each of these processes. Last year a physics model for the fall pipe was created based on experiments. The output of this model will be used as the initial input for the model created during this research. Furthermore, previous year's experiments can be used to gain a greater understanding of the fall process of stones and they can be used to validate the model results.

1.4. Main report outline

The report consists of 4 chapters (2,3,4 and 5) containing literature and two chapters (6 and 7) describing the development of the model and an application of the model. The aim of the literature is to provide a comprehensive overview of the processes and physics associated with stone dispersion, after which a model is designed based on this literature. A summary of the main content covered in each chapter is presented below.

- **Chapter 2** examines various processes that impact the accurate installation of stones by a stone installation vessel. Consequently, this chapter contains, among other things, information about the installation process, stone characteristics, and the fallpipe model by Vehmeijer (2022).
- **Chapter 3** aims to describe the falling behavior of a single stone in water by analyzing the forces acting on a single stone that occur due to various effects.
- **Chapter 4** gives an overview of the falling process of a group of stones and the different phases occurring during the descent of stone groups.
- **Chapter 5** discusses two different turbulence models used in computational fluid dynamics to close the Reynolds-averaged Navier-Stokes (RANS) equations and gives a brief introduction to the basics of numerical modeling.
- **Chapter 6** describes each step taken for designing the physics-based model. First, a model is designed based on the Single Stone Model by Manni and Vrijling (1995) describing the fall trajectory of a single stone while influenced by a lift force caused by vortex shedding. Secondly, the turbulence model is designed, which uses a Discrete Random Walk approach as described in ANSYS, INC. (2021), where the kinetic turbulent energy and the turbulent dissipation rate are used to create a random fluctuating velocity component in each direction to account for the influence of turbulence. Lastly, the individual models are combined to ensure a comprehensive representation of the physics involved. At the end of the chapter, the model validation takes place.
- **Chapter 7** contains the results of the application of the model, where a monopile and an ambient uniform current are added to the model.
- **Chapter 8** will present the final conclusions and recommendations for further research.

2

Stone installation using an inclined fallpipe

This chapter examines various processes that impact the accurate installation of stones by a stone installation vessel. The aim of this chapter is to gain a better understanding of the installation process and the possible impact of different processes on the final dispersion at the seabed. This chapter was written on the basis of several reports by van der Wal (2002),Konter (1983), De Reus (2004), Cregten (1995), Manni and Vrijling (1995), Bouwdienst RWS (1991), De Groot (1989a), De Groot (1989b) and Vehmeijer (2022)

2.1. Stone installation vessel

The vessel that will be used by GLDD is designed to accurately place stones on the seabed by using a fallpipe. A schematic top-and-side view, as well as a 3D rendering, of the side stone dumping vessel that GLDD will use are shown in Figure 2.1.

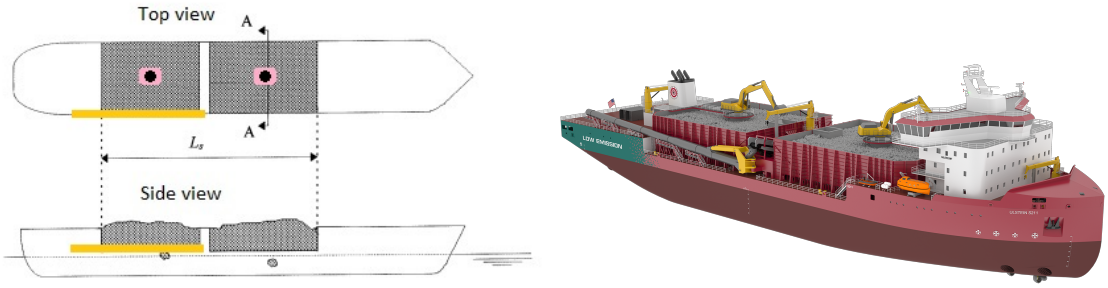

(a) Top- and side view Cregten (1995)

(b) 3d Rendering

Figure 2.1: Great Lakes Dredge & Dock rock installation vessel

The essential components of the vessel can be characterized by looking at the schematic overview (Figure 2.1a) of the side stone vessel that was previously detailed by Cregten (1995). where the gray areas shows the location of two large containers containing stones aboard the vessel. To move the stones onto the conveyor belt, which operates in between the containers, two cranes are located at the center of each stone container. These cranes are depicted in pink on the schematic overview. From the conveyor belt stones are loaded into the fallpipe, which is indicated by the yellow rectangle. The fallpipe is then used to accurately place the stones on the seabed at the designated area.

2.2. Stone installation

The stone installation operation of a side stone installation vessel is described by Cregten (1995). In his report Cregten (1995) distinguished two different ways of using a stone installation vessel. Installing the stones while the ship is moving and installing while the ship is stationary. If all the variables are constant, the expectation is that, when the ship is stationary, the stones will form a normally distributed pile on the seabed below the released location. When the ship is moving at a constant speed, the stones will either form a uniform Gaussian or triangular profile on the seabed. In reality, of course, due to external factors such as irregular loading of the stones onto the conveyor belt or an ambient current, the stones will not be uniformly distributed and irregularities will occur. The article mentions that currents have a large influence on the distribution and also concludes that the influence of irregular installation is significant and should be considered for an accurate model.

2.2.1. Stone characteristics

While the stones descend through the water, different falling behavior in the water may occur depending on the shape, mass density, and size of the stones. Heavier stones tend to fall at a higher velocity compared to smaller ones primarily due to their mass (Manni & Vrijling, 1995). The mass of a heavier stone also results in higher inertia, making it more resistant to changes in motion. As a result, heavier stones require more force to accelerate or decelerate, leading to a higher velocity during free fall and less dispersion. However, it's important to note that other factors, such as the shape of the stones and the influence of the (ambient) flow, can also affect their fall velocity and trajectory. Describing the stone characteristics involves several parameters, including the mean nominal stone diameter D_{n50}, the sort width, and the stone grading $\frac{D_{85}}{D_{15}}$. These parameters provide valuable information about the size distribution and variability of the stones within a certain stone group. Therefore, to ensure a consistent dispersion pattern prior to dumping the stones in water, it is very important to perform a number of tests to identify the characteristics of the stones.

Stone dimensions and weight

The dimensions of a stone can sometimes be difficult to determine because of its irregular shape. Therefore its shape is often quantified by the axial ratios: Maximum distance between two points L, Minimum distance between two points d, and the size of the smallest square hole the stone can fit through w. Both L/w and L/d ratios can be used to characterize the stone. However, in practice, the L/d ratio is used the most often. For an average stone, with a weight of 0.5 to 10 kg, the average L/d ratio is approximately 2.2 (Ravelli, 2009).

The nominal equivalent cube diameter D_n and the equivalent sphere diameter D_s are two different measures that can be used to describe the size of the stones. The difference between the two measures is that the nominal equivalent cube diameter D_n is based on the dimensions of a cube with the same volume as the stone, where D_m represents the length of the diagonal of the cube that has the same volume as the stone. The equivalent sphere diameter D_s is based on the diameter of a sphere with the same size as the size, where D_s represents the length of the diameter of the sphere that has the same volume as the stone. Both the nominal equivalent cube diameter D_n and the equivalent sphere diameter D_s are given by, respectively (van der Wal, 2002):

$$D_n = 1.0 \cdot (M/\rho)^{1/3} \tag{2.1}$$

$$D_s = 1.24 \cdot (M/\rho)^{1/3} \tag{2.2}$$

Where M is the mass of the stone and ρ is its mass density. By combining these two equations it also becomes possible to write a relation between both equivalent diameters: $D_n = 0.806 \cdot D_s$.

The nominal diameter can further be used to describe the stones below a certain threshold. For instance, the 50% nominal diameter D_{n50} describes the stones that are smaller than 50 mass percent of the stone group and is given by:

$$D_{n50} = 1.24 \cdot (M_{50}/\rho)^{1/3} \tag{2.3}$$

Converting the 50% nominal diameter D_{n50} to the median sieve size D_{50} can either be done by using an experimentally determined conversion factor 0.84. This would give the relation: $D_{n50}/D_{50} = 0.84$. Another way to describe the stone would be by using a shape factor. This Shape Factor is described by the following relation (van der Wal, 2002):

$$SF = (\frac{D_{n50}}{D_{50}})^{1/3} \tag{2.4}$$

Where SF is the shape factor which varies depending on the type of rock used or its size. Typically this value lies between 0.34 and 0.72.

As a result of the stones having irregular shapes and sizes, the drag coefficient, which describes the amount of drag force experienced as the stone moves through the water, is also influenced. The relation between the L/d ratio and the drag coefficient C_D is shwon in Figure 2.2.

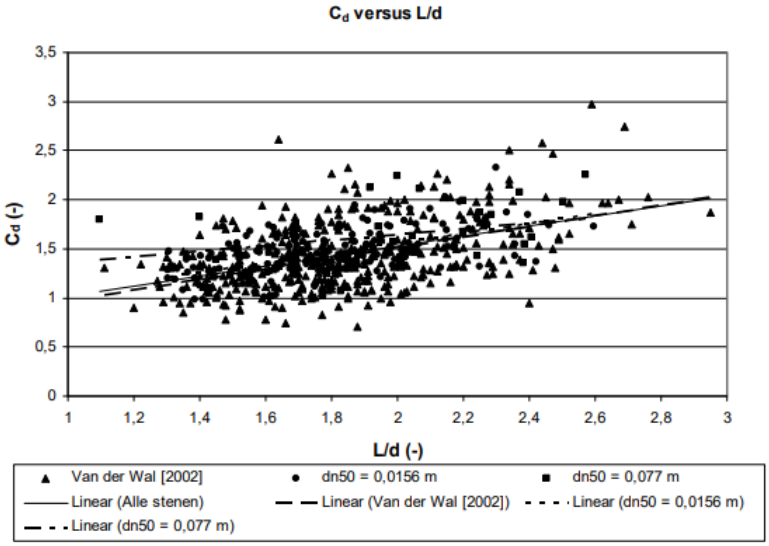

Figure 2.2: Regression lion C_d versus L/d with all data points from De Reus (2004) & van der Wal (2002)

From Figure 2.2 it can be observed that by increasing the L/d ratio (more irregular shape of a stone), the drag coefficient also increases. Consequently, it would be preferable to have a group of stones where all stones have dimensions that result in a similar L/d ratio to minimize the differences in drag coefficient between the stones.

Stone grading

The distribution of various stone sizes within a group of stones is referred to as stone grading. It is described by a percentage that indicates how many percent of the total mass of the distribution has a size smaller than the indicated size, where the center point of the distribution is given by D_{50}, indicating that 50% of the total mass of the stone group is comprised of stones smaller than the D_{50} diameter. The grading width is expressed by the ratio M_{85}/M_{15}, also known as the uniformity coefficient, and can also be described by looking at the steepness of a mass cumulative curve. The coefficient of uniformity is calculated as the ratio between the particle diameter D_{85} and D_{15}, where, respectively, 85% and 15% of the mass are smaller than the indicated size. When the coefficient has a value that lies between 1.7 & 3

the batch of stones is called single-sized and when this ratio lies between 3.4 & 16 they are widely graded (CUR 169, 1995).

2.2.2. Fallpipe

During stone installation, the stones will travel through a fallpipe. As a result of the variable angle of this fallpipe, stones can either fall through the pipe or form a sliding bed flow (Vehmeijer, 2022). The angle at which the transition to a sliding bed flow takes place is not entirely clear but was estimated by Vehmeijer (2022) to be around 70 degrees. Using this estimation he designed two models. The first model he created is called the sliding bed model (SBM) which can provide particle velocities in 5% accuracy from a pipe angle of 48° up to 86° for stone sizes from 10-25 mm. Because this model takes into account a sliding bed, the stone mixture also has a certain bed height inside the pipe, which can be described by the angle of the bed height β, see figure 2.4. The second model is called the vertical fall model (VFM). This model provides results within 10% accuracy for a vertical pipe of 90° down to a pipe under an angle of 70°.

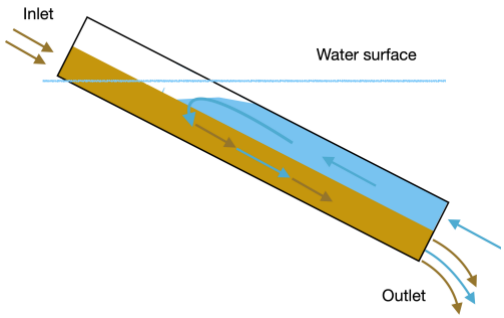

Figure 2.3: Flow directions in a fallpipe under an angle (Vehmeijer, 2022)

Figure 2.3 shows the flow directions inside a fallpipe that is positioned under an angle. At the inlet of the pipe, the interaction between stones and water results in the water filling the pores being dragged out of the pipe. This process requires the water needed to occupy the pore spaces between stones to be obtained from an external source. Given that the opening of the pipe is positioned above water, the necessary water supply comes from the side of the pipe that is underwater. As the stones force the water out of the pipe, the water level within the pipe decreases, creating a pressure differential between the internal and external regions of the pipe. This imbalance in pressure causes water to flow in the opposite direction of the sliding bed movement, referred to as the "backflow" by Vehmeijer (2022), from the outlet of the pipe.

This backflow contributes to the increased stone velocity at the outlet of the pipe, which has an impact on the stones' trajectories. Besides the backflow, due to the stones traveling at a high velocity when they exit the pipe, a 'jet' consisting of a mixture of stones and formed is formed at the outlet of the pipe (Kevelam, 2016). The stones, during their free fall, largely maintain the velocity they developed inside the fallpipe when they stay inside this 'jet'. In addition, due to increased turbulence (caused by high-velocity differentials), some stones will experience a large increase in kinetic energy, which can cause the stones to accelerate or decelerate in any direction. As soon as a stone manages to drop out at the bottom of this 'jet', it will start to decelerate and eventually follow a path described by the single stone model by Manni and Vrijling (1995), which is based on vortex shedding (Chopra & Mittal, 2019). The fluid field characteristics, the stones' characteristics, and their relative velocity/rotation all affect the stones' falling trajectory in the water and can give them a certain offset. The offset is the distance between the point where the stone starts to fall freely (in this case where it exits the fallpipe) and its position once it reaches the bottom of the seabed.

Pipe dimensions
The dimension of the pipe, as used by Vehmeijer (2022), are shown in figure 2.4. Most notably is the parameter β, which describes the angle of the bed height of the sliding bed flow.

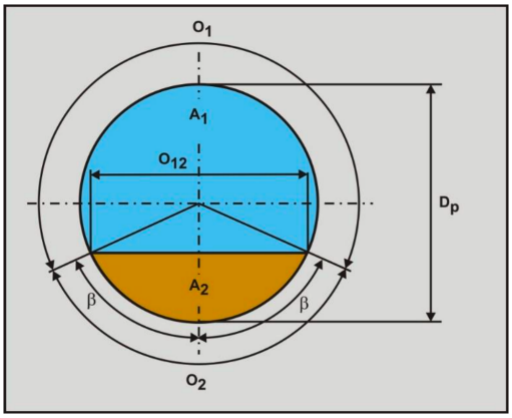

Figure 2.4: Schematic view cross section pipe (Vehmeijer, 2022)

Parameter	Description	Equation
β	Angle of the bed height [Rad]	[−]
O_1	Contact arc-length water and pipe [m]	$O_1 = D_p \cdot (\pi - \beta)$
O_2	Contact arc-length bed and pipe [m]	$O_2 = D_p \cdot \beta$
O_{12}	Width contact bed and water in pipe [m]	$O_{12} = D_p \cdot \sin(\beta)$
A_p	Cross sectional area pipe $[m^2]$	$A_p = \frac{\pi}{4} \cdot D_p^2$
A_2	Cross sectional area bed $[\mathrm{m}^2]$	$A_2 = \frac{D_p^2}{4} \cdot (\beta - \sin(\beta) * \cos(\beta)$
A_1	Cross sectional area water above bed $[m^2]$	$A_1 = A_p - A_2$
V_1	Velocity of water above bed $[m^2]$	$V_1 = \frac{A2 \cdot (1 - C_{vb}) \cdot V_2}{A1}$
V_2	Velocity of sliding bed $[\mathrm{m}^2]$	See eq 4 – 4

Initial offset
The initial offset in subsea stone installation can be influenced by various external factors, such as the angle of the fall pipe, stone sizes, and production rates. The influence of these factors on the offset has been researched by, among others, De Reus (2004) and reports by Bouwdienst RWS (1991) & De Groot (1989a). In De Groot (1989a) it was concluded that the diameter of the stone has minimal effect on the shift in the center of gravity of the stone group on the seabed. However, the shape ratio (L/d) of the stones did play a significant role in determining their falling trajectory. Additionally, the horizontal velocity of the stones can be influenced by the ambient current. The influence of the ambient current on the trajectory of a stone persists throughout the water depth until the difference between the velocity of the stones and the velocity of the current diminishes. The findings of De Groot (1989a) are summarized by Bouwdienst RWS (1991) in figure 2.5.

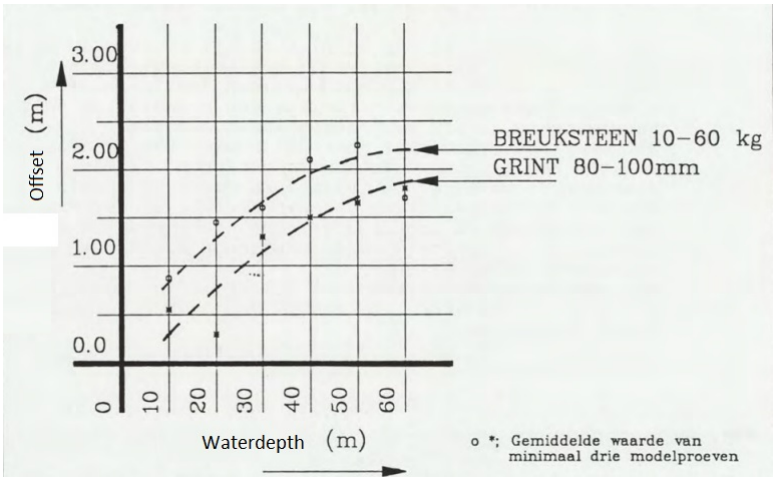

Figure 2.5: Influence of the depth on the offset (Bouwdienst RWS, 1991)

Figure 2.5 shows that for an increasing water depth the offset increases. It can also be observed that the heavier stone also has a larger initial offset.

2.2.3. Waves' impact on displacement

During stone installation operations, the presence of waves can result in ship movements. However, a study conducted by (Konter, 1983) on the falling of stones in a wave field suggests that the waves have minimal impact on the horizontal displacement of the stones compared to the influence of the flow velocity. The irregular breaches caused by the ship's back-and-forth motions and the distribution of falling rocks in the water tend to average out, leading to a negligible influence of the ship movements induced by the waves (Konter, 1983).

2.3. Concluding remarks

In conclusion, this chapter has provided an in-depth examination of the stone installation process using an inclined fallpipe on a stone installation vessel. By analyzing various processes and factors that affect stone dispersion, we have gained a better understanding of the installation operation and its potential impact on the seabed. The stone installation vessel used by GLDD, as depicted in the schematic diagrams, plays a crucial role in accurately placing stones on the seabed. We have discussed the characteristics of stones, including their dimensions, weight, and grading, which influence their falling behavior in water. Additionally, the fallpipe, with its variable angle and the transition between stone falling and sliding bed flow, has been described. The backflow and the formation of a stone 'jet' at the pipe outlet contribute to the stones' velocity and trajectory. The relative velocities, rotations, and fluid field characteristics further influence the stones' falling trajectory and offset from the point of exit. Overall, understanding these processes and considering the effects of external factors such as irregular loading and ambient currents is crucial for accurate modeling and successful stone installation projects.

3

Falling behavior of a single stone in water

This chapter aims to describe the falling behavior of a single stone in water by looking at the different forces acting on said stone. The first part describes the falling and deceleration as previously researched by Mazijk (1982). Subsequently, the vertical and horizontal forces acting on the stone, which have the potential to change the stone's trajectory will be discussed.

3.1. Falling acceleration and deceleration

The falling process refers to the free fall of a stone through water, spanning from the moment it exits the fall pipe until it reaches the seabed or an existing pile of stones, where the stone descends under the influence of gravity and interacts with the surrounding fluid environment. During this process, there are two phases that can be distinguished (Gelderen, 1999):

- The first phase consists of the stone either accelerating or decelerating until it reaches its terminal fall velocity.
- The second phase is characterized by the stone reaching its terminal fall velocity, resulting in the stone experiencing a constant rotation or form of movement.

For a stone, that is either accelerating or decelerating, the water depth should be sufficient to be able to achieve its terminal fall velocity. In the study performed by Mazijk (1982), an equation was found that describes the relationship between the vertical distance traveled and the proportion of the terminal fall velocity achieved by a stone. The experiments involved submerging the stones prior to release, thereby eliminating any initial velocity. The equation proposed by Mazijk (1982) describing the depth x at which a certain percentage of the terminal fall velocity is achieved is given by:

$$x = -\frac{1}{\beta} \cdot \ln\left(1-\alpha^2\right), \quad \text{with } \beta = 1.5 \cdot \frac{C_D}{D} \cdot \frac{\rho_f}{\rho_s} \tag{3.1}$$

where,

α: Percentage of the equilibrium fall velocity [%]

C_D: Drag coefficient [−]

D: Diameter of the stone [m]

ρ_f: Mass density of the fluid [kg/m^3]

ρ_s: Mass density stone [kg/m^3]

The relation was also studied in (WL M995, 1971), where they performed experiments using concrete blocks. These blocks were given an initial velocity to determine when the terminal fall velocity was achieved. During the experiments it was found that, by dropping concrete blocks at different heights above the surface, a terminal fall velocity was achieved after traveling a distance of 7-8 times the mean concrete block's diameter D_{50} through the water. This is in line with the formula 3.1 derived by (Mazijk, 1982), which states that, for α=99% and C_d=1, the stones also have to travel 7-8 times the diameter of the object. This means that his equation can also be used for accelerating or decelerating stones that have an initial velocity. Consequently, after the stones leave the fall pipe, their velocity should decelerate until it reaches the terminal fall velocity according to equation 3.1 proposed by Mazijk (1982).

According to (Meermans, 1997), an important observation contradicts the proposition made by Mazijk (1982) regarding the start of the second phase, where stones achieve a constant rotation. Meermans' research, which relied on video images obtained from Van Oord (1995), revealed that the blocks used by them reached their terminal fall velocity after approximately 8-9 times the diameter D_{50}, which is consistent with Mazijk (1982). However, it was found that a consistent rotation was only achieved after 20 times the diameter, indicating a discrepancy with Mazijk's earlier conclusion.

3.2. Forces on a falling stone

There are multiple forces that act on a stone during its fall trajectory, both in horizontal and in vertical direction. These forces include the buoyancy force (F_b), gravitational force (F_g), drag force (F_d), and lift force (F_L). Figure 3.1 illustrates the representation of these forces acting on a submerged stone during its descent through the water.

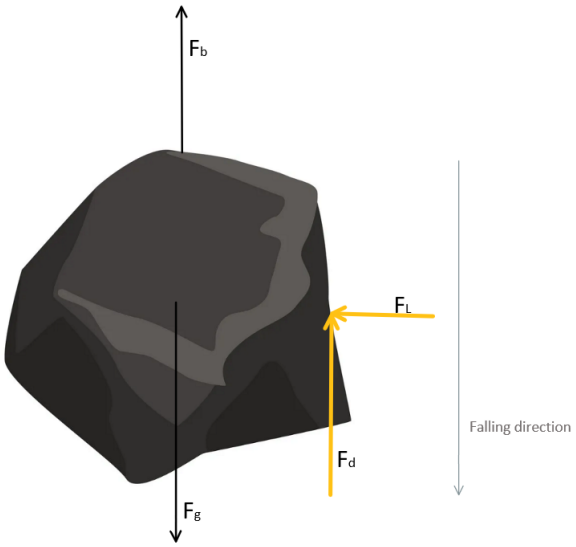

Figure 3.1: Forces on a falling stone in water

The forces acting on a stone can be categorized into vertical and horizontal components. In this chapter, initially, the vertical forces acting on the stones will be discussed. Subsequently, the horizontal forces will be examined and their various causes will be examined.

3.2.1. Vertical forces

Two forces are always acting on the stone while it is submerged in water, gravitational force F_g and buoyancy force F_b. Furthermore, if the stone or the ambient fluid is moving, it will also experience a drag force F_d in the opposite direction of the motion. The drag force endured depends on the drag

coefficient of the stone and therefore also on the shape of the stone. Respectively, the gravitational force F_g and the buoyancy force F_b can be described by the following equations:

$$F_g = \kappa_1 \cdot D^3 \cdot \rho_s \cdot g \tag{3.2}$$

$$F_b = \kappa_1 \cdot D^3 \cdot \rho_f \cdot g \tag{3.3}$$

Where the diameter of the stone is given by D, the density of the water and the stone is given by ρ_f, ρ_s, and the gravitational acceleration by g. The shape factor is given by κ_1, this variable can change depending on the shape of the stones, for a sphere this factor is $\frac{\pi}{6}$. It has to be noted that the use of shape factors might lead to confusion when utilizing or rewriting equations containing different shape factors. Therefore, $\kappa_1 \cdot D^3$, which describes the volume of the stone, can also simply be written as the volume V.

The other vertical force acting on the stone, the drag force, is of importance when there is motion with respect to the ambient fluid. This force depends on the flow around the stone, either due to a laminar or a turbulent boundary layer, which in its turn depends on the Reynolds' number. The drag force F_d is given by:

$$F_d = \frac{1}{2} \cdot C_D \cdot A_s \cdot \rho_f \cdot (u_f - u_s) \cdot |u_f - u_s| \tag{3.4}$$

Where C_D is the drag coefficient and A_s is the frontal area facing the flow direction. u_f and u_s are, respectively the velocity of the fluid and the velocity of the stone, which, since we are considering vertical forces, are both oriented in the vertical direction.

Each of the three vertical forces acting on the stone can be combined using Newton's second law ($F = ma$) to find a differential equation for the vertical fall velocity:

$$F_g + F_b + F_d = M \cdot \frac{dv_s}{dt} \tag{3.5}$$

With F_g, F_b, and F_d as the forces described above, M is the mass of the object, and $\frac{dv_s}{dt}$ is the vertical acceleration of the stone. When this differential equation is solved, the fall velocity can be written as a function of time. For a perfect sphere, without an initial fall velocity, the equation becomes:

$$v_s(t) = \sqrt{\frac{4 \cdot g \cdot D \cdot (\rho_s - \rho_f)}{6 \cdot C_D \cdot \rho_f}} \cdot \tanh\left(\sqrt{\frac{3 \cdot C_D \cdot g \cdot \rho_f}{8 \cdot D \cdot (\rho_s - \rho_f)}} \cdot t\right) \tag{3.6}$$

Where t is the time traveled from the moment of release. This equation can also be solved as a function of the vertical distance traveled (Miedema, 1981). By using the same initial conditions, the vertical velocity is then expressed as:

$$v_s(x) = \sqrt{\frac{4 \cdot g \cdot (\rho_s - \rho_f) \cdot D}{3 \cdot \rho_f \cdot C_D} \cdot \left(1 - e^{\frac{-3 \cdot \rho_f \cdot C_D \cdot x}{\rho_s \cdot D \cdot 2}}\right)} \tag{3.7}$$

Where x is the vertical distance traveled from the point of release. Equation 3.7 can be simplified to obtain the terminal fall velocity w. After the stone has traveled a certain distance the forces acting on the stone start to reach an equilibrium. As a result, the exponential on the right side of the equations starts to approach 0. Consequently, the remaining part of the equation is called the terminal fall velocity w and is given by:

$$w = \sqrt{\frac{4 \cdot g \cdot (\rho_s - \rho_f) \cdot D}{3 \cdot \rho_f \cdot C_D}} \tag{3.8}$$

Given the varying sizes and shapes of stones, it is necessary to consider that the terminal fall velocity may differ from that of a perfect sphere. Therefore, the expression for the terminal fall velocity can be generalized as follows:

$$w = \sqrt{2 \cdot \frac{V \cdot g \cdot \Delta}{A_s \cdot C_D}}, \quad \text{with } \Delta = \frac{\rho_s - \rho_f}{\rho_f} \tag{3.9}$$

where,

V =	Volume of the stone	$[m^3]$
A_s =	Frontal area	$[m^2]$
C_D =	Drag coefficient	$[-]$
D =	Stone diameter	$[m]$

3.2.2. Horizontal forces

The descent of a stone is influenced not only by vertical forces but also by horizontal forces, which can result in horizontal displacement in different directions. The impact of these forces on the displacement has been extensively discussed in studies such as De Groot (1989b), De Groot (1989a), van der Wal (2002) & De Reus (2004). These horizontal forces arise from interactions with the ambient flow, including factors such as turbulence, ocean currents, and the lift force generated by vortex shedding.

Ocean currents

The influence of ocean currents on the horizontal displacement of a stone descending through water will be researched in this subsection using the derivations of the displacement formulas that were developed by (De Groot, 1989b) and corrected by (De Reus, 2004). First, the horizontal acceleration of the stone in the x direction is calculated by applying Newton's 2^{nd} law on the lift force F_L acting on a stone, which is given by the following equation.

$$F_L = ma = V_{stone}\left(\rho_s - \rho_f\right)\frac{du_{s_x}}{dt} \tag{3.10}$$

Where V_{stone} is the volume of the stone, ρ_f and ρ_s are, respectively, the density of the fluid and the density of the stone. Furthermore, the horizontal lift force F_L acting on the stone is defined as follows:

$$F_L = \frac{1}{2}\rho_f A_s C_L \left(u_{\text{current}} - u_{s_x}\right)^2 \tag{3.11}$$

where,

ρ_f: Density of the water $[kg/m^3]$

A_s: Surface area of the stone facing the flow direction $[m^2]$

C_L: Horizontal drag coefficient $[-]$

$u_{current}$: Horizontal velocity of the current $[m/s]$

u_{s_x}: Horizontal velocity of the stone $[m/s]$

The horizontal lift force, denoted as F_L and described by equation 3.11, is subsequently substituted into equation 3.10, resulting in the following expression:

$$\frac{1}{2}\rho_f A_s C_L \left(u_{\text{current}} - u_{s_x}\right)^2 = V_{stone}\left(\rho_s - \rho_f\right)\frac{du_{s_x}}{dt} \tag{3.12}$$

Equation 3.12 is then rewritten for $\frac{du_{s,x}}{dt}$, which gives the differential equation for the horizontal acceleration of the stone under water:

$$\frac{du_{s_x}}{dt} = \frac{A_s}{2V_s}\frac{\rho_f}{\rho_s - \rho_f} C_L \left(u_{s_x} - u_{\text{current}}\right)^2 \tag{3.13}$$

The differential equation above can be used to determine the stone's horizontal velocity before the stone reaches the ambient fluid velocity. However, upon solving the differential equation, it becomes evident that the stone's horizontal velocity approaches the ambient fluid velocity within a relatively short time period compared to the overall duration of the fall. Figure 3.2 provides a schematic illustration of a stone's descent within a current.

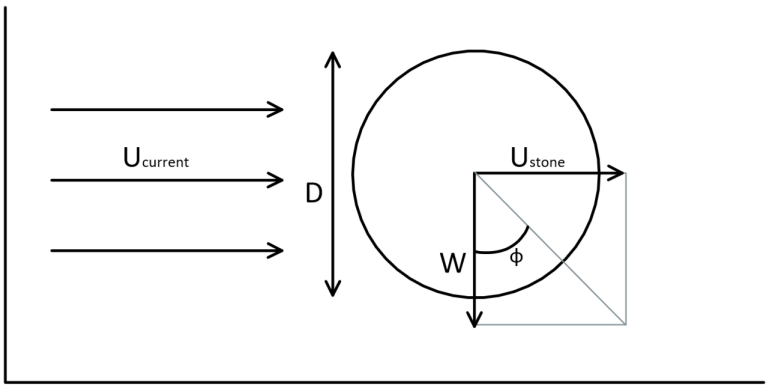

Figure 3.2: Horizontal current on a single stone

As can be seen in figure 3.2, the angle ϕ can be used to describe a relation between the equilibrium falling velocity w and the velocity of the current $u_{current}$. During equilibrium, $u_{s_x} = u_{current}$, the following equation describes the trajectory of a falling stone (De Groot, 1989b):

$$\tan\phi = \frac{u_{s_x}}{w} = \frac{u_{\text{current}}}{w} \tag{3.14}$$

Or, by filling in the equation for the terminal velocity (w) in equation 3.14, $\tan(\phi)$ can also be described by:

$$\tan\phi = \frac{u_{\text{current}}}{w} = C \cdot \frac{u_{\text{current}}}{\sqrt{\Delta g D}} \tag{3.15}$$

where,

Δ: Relative density ($\frac{\rho_s - \rho_f}{\rho_f}$) [$-$]

g: Gravitational constant [m/s^2]

D: Diameter [m]

C: Coefficient [$-$]

Based on equation 3.15, De Reus (2004) was able to describe the displacement of the center of gravity from the stone piles on the seabed in both the x- and y-direction with respect to the point where the stones enter a terminal vertical fall velocity while a current applies under a certain angle with the following equations:

$$x = \sin(\alpha_s) \cdot \frac{h u_{\text{current}}}{\sqrt{\Delta g D}} \sqrt{0,45 C_d \cos^2(\alpha) + 0,5 C_d \sin^2(\alpha_s)} \tag{3.16}$$

$$y = \cos(\alpha_s) \cdot \frac{h u_{\text{current}}}{\sqrt{\Delta g D}} \sqrt{0,45 C_d \cos^2(\alpha) + 0,5 C_d \sin^2(\alpha_s)} \tag{3.17}$$

where,

x, y: Offset [m]

h: Water depth [m]

u_{current} : Current velocity $[m/s]$

C_D: Drag coefficient $[-]$

α_s: Angle of the current with respect to the longitudinal axis of the ship $[rad]$

Lift force
An asymmetric flow field around the stone results in a lift force. This force acts on the stone in a direction perpendicular to the motion. When the fall direction is vertical, as we assume in this case, the lift force will be horizontal. The lift force F_L is given by:

$$F_L = \frac{1}{2} \cdot C_L \cdot A_s \cdot \rho_f \cdot (u_f - u_{s_x}) \cdot |u_f - u_{s_x}| \tag{3.18}$$

Where A_s is the surface area of the stone facing the flow direction (frontal area), u_f,u_{s_x} are, respectively, the horizontal velocity of the flow and the horizontal velocity of the stone and C_L is the lift coefficient. Three factors that contribute to the lift coefficient which causes the movement of the falling stone are the Magnus effect, Vortex-shedding, and asymmetrical separation of the boundary layer surrounding the stone. These processes will be described in more detail in the upcoming paragraphs.

Magnus effect
The Magnus effect is observed when an object undergoes rotation, resulting in friction between the surrounding fluid and the object itself. This effect arises due to the difference in fluid velocity on both different sides of the object. This difference in flow rate causes the boundary layer to persist for a longer duration on the side where the rotational direction opposes the direction of movement, while it separates earlier on the side where the rotational direction aligns with the motion direction. Consequently, the asymmetric pressure distribution results from the asymmetric separation of the boundary layers. The resulting lift component that is caused by this pressure differential is then pointed in the direction with the smallest difference in velocity between the edge of the falling object and the moving water, which is perpendicular to the fall direction.

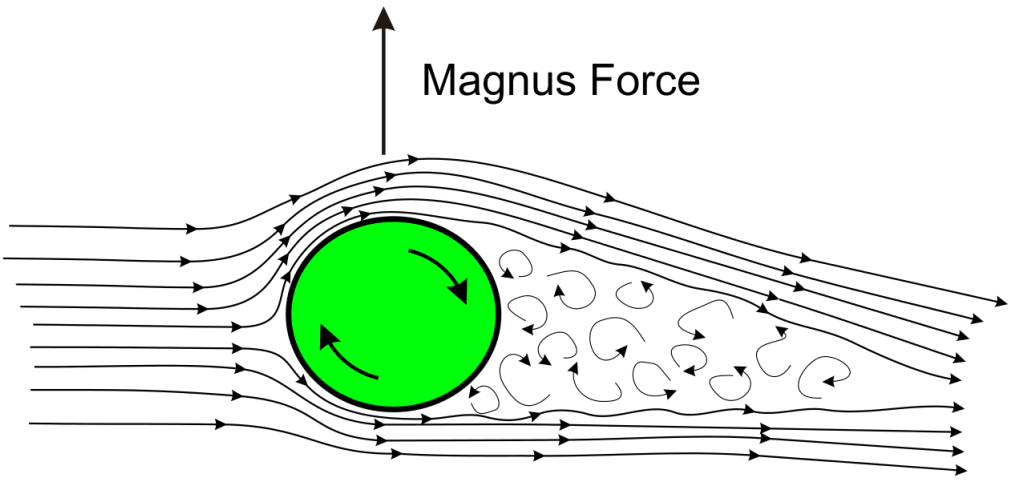

Figure 3.3: Lift force ('Magnus force') caused by the Magnus effect

Asymmetrical separation of the boundary layer
If an object has a surface that is smoother on one side and somewhat rough on the other side, asymmetrical separation of the boundary layer can occur. The laminar boundary layer flow on the "smooth" side will release earlier than the flow over the "rough" side. This asymmetrical separation causes an asymmetric pressure distribution that causes a lift force. When the resulting lift force does not pass through its center of gravity it causes the object to rotate, the previously mentioned Magnus effect then occurs.

Vortex shedding
Vortex shedding refers to the oscillating flow pattern that occurs when an object moves through a fluid, such as water. It is characterized by the formation of vortices at the rear of the object. When the Reynolds number, a dimensionless parameter representing the fluid flow regime, exceeds a certain threshold (typically around 1000), these vortices start detaching alternately from either side of the object, resulting in periodic shedding. The behavior of vortex shedding can be quantified using the Strouhal number, which describes the relationship between the shedding frequency, the characteristic length of the object (diameter), and the velocity of the fluid flow. In two-dimensional form, the Strouhal number can be expressed as follows:

$$St = \frac{\omega \cdot D}{w} = \frac{2\pi}{T}\frac{D}{w} \tag{3.19}$$

where,

ω: Radial frequency of vortex separation $[1/s]$

D: Diameter $[m]$

w: Terminal velocity $[m/s]$

T: Period of vortex separation $[s]$

When vortices are shed alternately from different sides of an object, they create a series of alternating low-pressure and high-pressure regions in the fluid. These pressure fluctuations can exert a force on the object, causing it to move in different horizontal directions. The force exerted on the object is known as the lift force, which is usually directed perpendicular to the direction of the flow. This force can vary both in magnitude and direction leading to a horizontal displacement and is illustrated in 3.4.

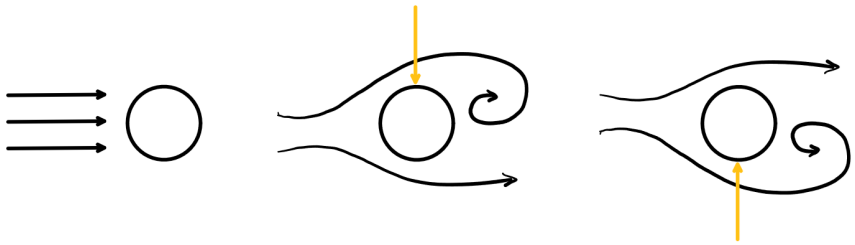

Figure 3.4: Vortex shedding can cause displacement of the object in multiple directions. The black arrows indicate the flow of the fluid and the yellow arrows indicate the lift force

The influence of this lift force on the fall trajectory of the stone was researched by Manni and Vrijling (1995). In their study, a model called the Single Stone Model was designed that describes the random walk followed by a single stone and its resulting distribution at the seabed. The model takes into account various different factors, including the shape and size of the stone, the properties of the fluid, and the water depth. For a comprehensive understanding of the Single Stone Model and the underlying physical background, refer to Appendix A and chapter 6.3 of the document. These sections provide detailed information on the model and its background.

The derivation for the horizontal displacements as previously described by Manni and Vrijling (1995) is given below.

When there is a constant fall velocity and a constant stone diameter, the Strouhal number is also constant. Assuming Strouhal's number can also be defined in 3D it becomes possible to use equation 3.19 to describe the period between each vortex separation by combining it with an equation for the terminal fall velocity (equation 3.8). The period is then described by:

$$T = \frac{2\pi}{St\sqrt{2\Delta\frac{g}{C_D}}}\sqrt{D} \tag{3.20}$$

The horizontal distance ($s_{\Rightarrow}$) that the stone travels during the time (T) can be described by neglecting possible resistances in the direction of the lift force. It is given by:

$$s_{\Rightarrow} = \frac{1}{2}a_{\Rightarrow}T^2 = C_L D\frac{\rho_f}{\rho_s}\frac{\gamma'}{St^2} \tag{3.21}$$

Where $a_{\Rightarrow}$ is the horizontal acceleration $[m/s^2]$, that follows from rewriting the lift force using Newton's second law. γ' is a constant that is derived from combining multiple shape factors and is, therefore, dependent on the shape of the stone. The complete derivation, including that of this term, can be found in Appendix A. Besides the horizontal displacement during time (T), the vertical displacement $s_{\Downarrow}$ of the stones can also be described and is given by:

$$s_{\Downarrow} = wT = \frac{2\pi}{St}D \tag{3.22}$$

Where the terminal velocity (w) follows from rewriting equation 3.19. Finally, depending on the water depth h, the number of horizontal directional changes (N) that the stone experiences during its fall is described (and can be estimated) by:

$$N = \frac{h}{s_{\Downarrow}} \approx \frac{h}{2\pi D}St \tag{3.23}$$

3.3. Concluding remarks

This chapter focused on the falling behavior of a single stone in water and examined the forces acting on the stone during its descent. The falling process was divided into two phases: acceleration or deceleration until reaching the terminal fall velocity, and constant rotation or movement at the terminal fall velocity. The depth at which a certain percentage of the terminal fall velocity is achieved was described using an equation derived by Mazijk (1982). However, Meermans (1997) found differences at the start of the second phase, indicating that a constant rotation was achieved after a greater distance than previously concluded.

The forces acting on the stone were categorized into vertical and horizontal components. The vertical forces included gravitational force, buoyancy force, and drag force. The equations for these forces were derived, taking into account factors such as the shape of the stone, drag coefficient, and fluid velocity. The differential equation for the vertical fall velocity was obtained by combining these forces using Newton's second law. The fall velocity as a function of time and vertical distance traveled was derived for a perfect sphere without an initial fall velocity.

In addition to vertical forces, horizontal forces acting on the stone during its descent were also discussed, specifically the lift force. The impact of the lift force as a result of ocean currents, the Magnus effect, asymmetrical separation of boundary layers, and vortex shedding on the horizontal displacement of the falling stone was examined. An equation for the lift force, dependent on the density of the water, surface area of the stone facing the flow direction, drag coefficient, and current velocity, was derived. This equation was used to obtain insights into the horizontal acceleration and thus the displacement of the stone.

4

Falling behavior of stone groups

The falling behavior of a group of stones, which are simultaneously deposited in water, is described by Slack (1963) and van der Wal (2002). Slack (1963) describes the two-phase principle, which consists of a thermal phase (where the fluid is comparable to a cloud) and the so-called 'swarming phase'. It is important to note that these phases describe stones that are free-falling without the influence of a fallpipe (or a jet).

4.1. Two phase principle

The two-phase principle, as described by Slack (1963), was created after doing multiple tests with a large amount of very small glass spheres that were dropped simultaneously in an air environment. It was observed that, first, the spheres fell in a circular group where the fall velocity of the group of stones was larger than the individual terminal velocity of the spheres. Furthermore, it was observed that the spheres rotated in a circular motion within the cluster ('cloud') of spheres, with a tendency towards the center. This phase was called the **'thermal phase'** and can be compared to a cloud where hot air rises from the middle and then drops on the sides.

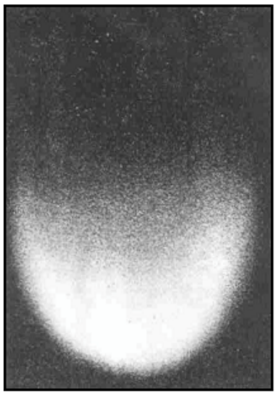

Figure 4.1: Bowl-like appearance of a falling group of spheres in air by (Slack, 1963)

Stones dropped in water behave similarly to the glass spheres that were used by Slack (1963). During their fall, the terminal velocity of individual stones within a group is exceeded by the terminal velocity of the group of stones (van der Wal, 2002), and the stones will rotate around the center. However, it has to be noted that there must be a sufficient quantity of stone to properly observe this group's behavior. According to van der Wal (2002) this is the case for a group of at least 50 to 100 stones that are all dropped simultaneously. Furthermore, during the thermal phase, the water flowing through the gaps between the falling stones travels at the same velocity as the stones themselves. As a consequence,

there is an expansion in the volume of the stone group, resulting in a deceleration. However, entrainment occuring at the rear of the stone group partially compensates for this deceleration by creating an undeveloped wake, which lowers the drag coefficient of the entire group. As a result, the increase in volume has less of an impact on the decrease in fall velocity. Initially, the shape of the group is spherical, however, as the group accelerates it will take on a bowl-like appearance, with larger stones at the bottom of the cloud. This is shown in figure 4.1.

The second phase is called the **'swarming phase'**. In this phase, the width of the swarm increases with the square root of the depth, and the velocity of the stone group ('swarm') approaches the individual velocity of the largest stones, which are at the bottom. Additionally, the water is no longer carried along by the swarm and the larger stones pull the smaller stones with them in their wake.

4.2. Five different falling phases

When the water depth is sufficient it becomes possible to distinguish more phases than the two described by Slack (1963). As such, van der Wal (2002) came up with the five-phase principle which describes these different phases. Each of them is described below:

Acceleration of the stone group
In accordance with the stone's mass, shape and pore content, the group velocity increases. Within this stone group, water gets trapped and can be considered as added mass. This water is added at the rear of the group. This phase only takes place when the total number of stones in the group is high enough and the initial pore content is low enough.

Deceleration of the stone group
After reaching the maximum group velocity in the first phase the group starts to decelerate. This deceleration lasts until the largest stones in the group reach their terminal velocity. In this phase, the added mass (water) decelerates together with the falling stones.

Stone front of larger stones
The largest stones in a stone group begin to separate from the group after the velocity of the stone group has decreased to a level that is equivalent to their terminal velocity. The added mass (water) is left behind, and the ambient water uses up its kinetic energy to dissipate it. The stones are now falling through the water hardly taking any of the water with them along their path. The smaller stones in the stone group follow in the wake of the larger stones that are in front of them.

Falling according to the single stone model
The stones fall according to the Single Stone Model by Manni and Vrijling (1995) when they are spaced out so far that they are no longer influenced by one another. The Single Stone Model is described in chapter 6.3 and Appendix A and can be used to describe the falling behavior of a single stone descending in water. In accordance with this model, the individual stones descend at their own terminal velocity following a random walk due to a varying lift force., resulting in the stones moving in different horizontal directions. If the water depth is sufficient, the stones will reach the seabed according to a normal distribution.

Radial runoff
When phase 3, a stone front of larger stones, is not reached before the bottom is reached it indicates that the stone group still contains a significant amount of water in the form of added mass. This water will radially flow along the bottom and can take stones with it along its path if it is strong enough. The distance the stones will travel along the bottom depends on the group velocity, group mass+added mass (water), the mass of the individual stones and the surface roughness.

4.3. Hindered settling

Besides the different falling phases, described by Slack (1963) and van der Wal (2002), hindered settling occurs. This phenomenon was described by Richardson and Zaki (1997) and occurs when a group of particles is continuously dumped into stagnant water where the presence of hindering effects limits the particles' ability to descend. One of these effects may be an increase in drag coefficient brought on by the presence of other particles nearby, as well as an up-flow of water caused on by the displacement of the falling particles. Consequently, the volumetric concentration of the stones has a significant impact on these hindered effects. The hindered settling velocity can therefore be calculated for concentrations of up to 30% by using the following equation (Richardson & Zaki, 1997):

$$w_s = w \cdot (1 - c_v)^m \tag{4.1}$$

Where w is the terminal velocity, c is the volumetric concentration of solids within the fluid and m is an empirical exponent related to the particle Reynolds number Re_p. The approximate value for exponent m is given by:

$$m = \frac{4.7 + 0.41 \cdot Re_p^{0.75}}{1 + 0.175 \cdot Re_p^{0.75}}, \quad \text{with } Re_p = \frac{w \cdot D}{\mu} \tag{4.2}$$

4.4. Concluding remarks

This chapter examined the falling behavior of simultaneously deposited stone groups in water. The two-phase principle, described by Slack (1963) and van der Wal (2002), revealed a thermal phase where the stones form a circular group, rotate inward, and experience deceleration due to expanded volume. The swarming phase follows, characterized by the widening of the stone group and the influence of larger stones on smaller ones. The hindered settling effect, outlined by Richardson and Zaki (1997), occurs when hindering effects interfere with the descending particles. These insights are valuable for modeling the dispersion of a group of stones.

5

Numerical modeling

This chapter discusses two different turbulence models used in computational fluid dynamics (CFD) and gives a brief introduction to the basis of numerical modeling. Both of these models, the k-ε by Jones and Launder (1973) and the k-ω model by Wilcox et al. (1998), are frequently used and both have their strengths and weaknesses.

5.1. Background of numerical modeling

Numerical modeling is often used to approximate real-world flows governed by partial differential equations (PDEs). However, as a result of the numerical models only being approximations of the real solution, they can have errors due to discretization errors, limited computing power, etc.

A particular set of partial differential equations (PDEs), also known as the Reynolds Average Navier-Stokes (RANS) equations, is used to describe the motion of a viscous fluid. The equations can be obtained by time-averaging the Navier-Stokes equations. They describe the conservation of energy, mass and momentum. The RANS equations are described in equation 5.1.

$$\frac{\partial(\rho \boldsymbol{U})}{\partial t} + \nabla \cdot (\rho \boldsymbol{U}\boldsymbol{U}) = -\nabla p + \nabla \cdot \left[\mu\left(\nabla \boldsymbol{U} + (\nabla \boldsymbol{U})^T\right)\right] + \rho \boldsymbol{g} - \nabla\left(\frac{2}{3}\mu(\nabla \cdot \boldsymbol{U})\right) - \underbrace{\nabla \cdot \left(\overline{\rho \boldsymbol{U}' \boldsymbol{U}'}\right)}_{\text{Reynolds-stress}} \tag{5.1}$$

In the RANS equations, there is an additional term called the Reynolds stress on the right-hand side. The Reynolds stress describes the turbulent transport of momentum, which is the force that causes an object to move. This term arises as a result of applying the Reynolds averaging process to the product of the two fluctuating velocity components and subsequently taking the divergence of the resulting term. The Reynolds stress is an unknown in the RANS equation. To obtain equations containing only the mean velocity (U) and pressure, the RANS equations need to be closed by calculating the Reynolds stress term. This is also known as the closure problem. The most popular way of solving this is by using the Boussinesq hypothesis.

$$\underbrace{-\overline{\rho \boldsymbol{U}' \boldsymbol{U}'}}_{\text{Reynolds stress}} = \mu_t \underbrace{\left(\nabla \boldsymbol{U} + (\nabla \boldsymbol{U})^T\right)}_{\text{Mean Velocity Gradients}} - \frac{2}{3}\rho k \boldsymbol{I} - \frac{2}{3}(\nabla \cdot \boldsymbol{U})\boldsymbol{I} \tag{5.2}$$

Equation 5.2 above describes the Boussinesq hypothesis. It relates the Reynolds stress term to the mean velocity gradients in a fluid flow through a dynamic eddy viscosity or turbulent viscosity term, denoted as μ_t. Specifically, the Reynolds stress is related to the mean velocity gradients, as indicated by the under brace term in the equation, by using the eddy viscosity term in the Boussinesq approximation. Once the eddy viscosity term μ_t is calculated, it can be used to express the Reynolds stress term in the Reynolds-Averaged Navier-Stokes (RANS) equations and to close the system of

equations. This eddy viscosity term can be calculated or computed using different turbulence models.

Previous RANS turbulence models, prior to the developments of the k-ϵ and the k-ω model, used a mixing length approach to calculate what the eddy viscosity term is. The mixing length is commonly denoted by l_m and represents an indication of the size of turbulent eddies in the fluid flow. A large amount of turbulence or energy will result in a large mixing length which will also result in a large eddy viscosity.

The Prandtl mixing length hypothesis provides a way to estimate the eddy viscosity μ_t as a function of density ρ, mixing length l_m and the velocity gradient $\frac{\partial U}{\partial y}$:

$$\mu_t = \rho l_m^2 \left| \frac{\partial U}{\partial y} \right| \tag{5.3}$$

where,

$$l_m = \kappa y, \qquad \kappa = 0.41 \tag{5.4}$$

The Prandtl mixing length hypothesis states that when eddies are located at a certain distance to a wall then the maximum size of the eddies is constrained by the presence of the wall. As one moves closer to the wall, the maximum size of the eddies that can exist in the flow decreases. Conversely, as one moves away from the wall, the maximum size increases, since the dissipation effect of the wall is weaker. Therefore, Prandtl proposed a hypothesis that says the mixing length is proportional to this distance y multiplied by a constant κ, which has a value of 0.41.

An improvement on this Prandtl hypothesis is the van Driest mixing model (Van Driest, 1956) which states that, as the wall is approached, the influence of viscosity is also going to dampen the eddies. Based on the van Driest mixing model, the mixing length is calculated as follows:

$$l_m = \kappa y \left[1 - \exp\left(-\frac{y^+}{A^+} \right) \right] \quad A^+ = 26.0 \tag{5.5}$$

Where $A+$ has a constant value of 26. The use of a damping function allows for a more accurate representation of the velocity near the walls. This function is nonlinear over the distance of the wall and varies depending on the type of flow and the specific parameters.

Early eddy viscosity models specify the mixing length algebraically, which means that it depends solely on the distance to the nearest wall. Therefore, for a certain geometry, the distance to the nearest wall is predetermined throughout the entire domain, except when the geometry moves. Since the distance to the nearest wall is constant, the mixing length and, consequently, the eddy viscosity remain unchanged as well. However, this model needs to be improved because turbulence is not static as it diffuses and convects through the fluid instead of being fixed at a specific distance from the wall. Therefore a transport equation for the turbulent variables (kinetic energy and the dissipation rate) has to be solved. The upcoming sections will discuss both the k-ε and the k-ω model.

5.2. k-ε model

For simulating turbulent flow conditions and determining the mean flow characteristics of turbulent flow, the k-ε turbulence model by Jones and Launder (1973) is the most commonly used one in computational fluid dynamics (CFD). The k-ε model assumes that the turbulent flow can be modeled as a combination of large-scale eddies and small-scale eddies. The large-scale eddies are responsible for the transport of kinetic energy, while the small-scale eddies are responsible for the dissipation of that energy into heat. The model provides a comprehensive depiction of turbulence by using two transport equations. The first turbulent variable used is the turbulent kinetic energy (k), and the second variable is the rate of dissipation of turbulent kinetic energy (ε). Both are obtained, respectively, from the following transport equations (ANSYS, INC., 2021):

$$\frac{\partial}{\partial t}(\rho k) + \frac{\partial}{\partial x_i}\left(\rho k u_i\right) = \frac{\partial}{\partial x_j}\left[\left(\mu + \frac{\mu_t}{\sigma_k}\right)\frac{\partial k}{\partial x_j}\right] + G_k + G_b - \rho\varepsilon - Y_M + S_k \tag{5.6}$$

and

$$\frac{\partial}{\partial t}(\rho\varepsilon) + \frac{\partial}{\partial x_i}\left(\rho\varepsilon u_i\right) = \frac{\partial}{\partial x_j}\left[\left(\mu + \frac{\mu_t}{\sigma_\varepsilon}\right)\frac{\partial \varepsilon}{\partial x_j}\right] + C_{1\varepsilon}\frac{\varepsilon}{k}\left(G_k + C_{3\varepsilon}G_b\right) - C_{2\varepsilon}\rho\frac{\varepsilon^2}{k} + S_\varepsilon \tag{5.7}$$

As a result of the mean velocity gradients, G_k represents the production of turbulent kinetic energy. This term is be defined as (ANSYS, INC., 2021):

$$G_k = -\rho\overline{u_i' u_j'}\frac{\partial u_j}{\partial x_i} \tag{5.8}$$

Furthermore, as stated in ANSYS, INC. (2021), G_b is the generation of turbulence kinetic energy due to buoyancy, Y_M represents the contribution of the fluctuating dilatation in compressible turbulence to the overall dissipation rate, $C_{1\varepsilon}C_{2\varepsilon}$ and $C_{3\varepsilon}$ are constants. σ_k and σ_ε are the turbulent Prandtl numbers for k and ε, respectively. S_k and S_ε are user-defined source terms. The model coefficients have evolved through time, however, the coefficients used by Launder and Sharma (1974) are still the most frequently used ones in the standard $k-\varepsilon$-model. In the table below some different model constants are listed.

Model	σ_k	σ_ϵ	$C_{1\varepsilon}$	$C_{2\varepsilon}$	C_μ
Jones & Launder (1972)	1.0	1.3	1.55	2.0	0.09
Launder & Spalding (1974)	1.0	1.3	1.44	1.92	0.09
Launder & Sharma (1974)	**1.0**	**1.3**	**1.44**	**1.92**	**0.09**

In cases where the turbulent transport terms are negligible and the Reynolds number is high, the mixing length l_m can be modeled as a function of the turbulent dissipation rate ϵ and the turbulent kinetic energy k (Launder & Spalding, 1974):

$$l_m = \frac{C_\mu k^{3/2}}{\epsilon} \tag{5.9}$$

Using the mixing length l_m calculated in 5.9 the eddy viscosity μ_t can now be computed by combining both the turbulent kinetic energy k and the turbulence dissipation rate ε (Launder & Spalding, 1974):

$$\mu_t = C_\mu \rho k^{1/2} l_m \tag{5.10}$$

Now that the eddy viscosity is known, it can be inserted into the Boussinesq hypothesis (eq. 5.2) which can then be used in the RANS equations (eq. 5.1) which then closes the system of equations.

5.3. k-ω model

The k-ε model is not accurate when it comes to predicting boundary layers with adverse pressure gradients. It is even worse in cases of supersonic flow. Therefore many models have been proposed that should give a better performance for these adverse pressure gradients, such as Spalart-Allmarar, Johnson-King, or the k-ω model. This section will only focus on the k-ω model as it's still one of the most popular models used to this date. Important to note is that there are many different versions of the k-ω model that have been proposed through time, all of which are slightly different. The model is based on the model by Wilcox et al. (1998), which includes modifications for lower Reynolds number effects such as shear flow spreading or compressibility (ANSYS, INC., 2021). It is an empirical model based on the turbulent kinetic energy (k) and the specific dissipation rate (ω). Both are obtained, respectively, from the following transport equations (ANSYS, INC., 2021):

$$\frac{\partial}{\partial t}(\rho k) + \frac{\partial}{\partial x_i}\left(\rho k u_i\right) = \frac{\partial}{\partial x_j}\left(\Gamma_k \frac{\partial k}{\partial x_j}\right) + G_k - Y_k + S_k \tag{5.11}$$

and

$$\frac{\partial}{\partial t}(\rho\omega) + \frac{\partial}{\partial x_i}\left(\rho\omega u_i\right) = \frac{\partial}{\partial x_j}\left(\Gamma_\omega \frac{\partial \omega}{\partial x_j}\right) + G_\omega - Y_\omega + S_\omega \tag{5.12}$$

As indicated in ANSYS, INC. (2021), G_k denotes the generation of turbulence kinetic energy resulting from mean velocity gradients and is given by equation 5.8. G_ω denotes the production of ω.Γ_k and Γ_ω represent the effective diffusivity of, respectively, k and ω. The variables Y_k and Y_ω represent the dissipation of k and ω caused by turbulence. Furthermore, the terms S_k and S_ω are user-defined source terms. For a full derivation of these terms and the transport equations refer to ANSYS, INC. (2021). The model constants used in the standard k-ω model are listed in the table below:

Constant	α^*_∞	α_∞	α_0	β^*_∞	β_i	R_β	R_k	R_ω	λ^*	M_{t0}	σ_k	σ_ω
Value	1	0.52	1/9	0.09	0.072	8	6	2.95	1.5	0.25	2.0	2.0

The eddy viscosity μ_t can be calculated using,

$$\mu_t = \alpha^* \frac{\rho k}{\omega} \tag{5.13}$$

The coefficient α^* dampens the turbulent viscosity for low-Reynolds numbers. For high Reynolds numbers, it has to be noted that $\alpha^* = \alpha^*_\infty = 1$. This damping coefficient is given by (ANSYS, INC., 2021):

$$\alpha^* = \alpha^*_\infty \left(\frac{\alpha^*_0 + Re_t/R_k}{1 + Re_t/R_k}\right), \quad \text{with } Re_t = \frac{\rho k}{\mu\omega}, \quad \alpha^*_0 = \frac{\beta_i}{3} \tag{5.14}$$

The main weakness of the k-ω model is that it is dependent on the freestream turbulence conditions. The reason for this dependency is still not entirely clear. Some authors have suggested that the k-ω model is missing a cross-diffusion term, which is present in the $k-\omega SST$ by Menter (1994). Whereas other authors have suggested that the model coefficients are not tuned correctly. As the reason is still unclear, to this day, the current recommendation is to use the $k-\omega$ SST Model as it doesn't have this free stream turbulence dependency.

5.4. Comparison

In Computational Fluid Dynamics (CFD), both the $k-\varepsilon$ and $k-\omega$ turbulence models are widely used. However, there are differences between the models in how they model the dissipation of turbulence and the near-wall behavior.

The k-ε model independently evaluates the turbulent kinetic energy (k) and its dissipation rate (ε). Therefore, the model assumes that turbulence is isotropic with the same statistical properties in every direction. Consequently, the k-ϵ model is well suited for modeling turbulent flows that consist of separated flows and strong pressure gradients.

In contrast to the k-ε model, the k-ω model uses a single equation for the calculation of the specific dissipation rate (ω) to model both the turbulent kinetic energy and its dissipation rate. This allows the model to more accurately represent anisotropic turbulence, which means that the statistical properties of turbulence differ in every direction. The k-ω model predicts the near-wall behavior of turbulent flows better than the k-ε model. If one is not interested in near-wall flow behavior, the k-ε model would be the preferred option.

6

Model

In this chapter, a physics-based model will be designed to calculate the dispersion of stones exiting a diagonal fallpipe. The trajectory of a stone will be modeled using an iterative process whereby the equations of motion are solved for each time step. First, the fall trajectory will be modeled based on the Single Stone Model by Manni and Vrijling (1995), then the trajectory will be modeled using a turbulence model, and finally, both models will be combined to create a physics-based model.

6.1. Methodology

The methodology can be divided into several different parts. These parts consist of modeling in MATLAB, creating a mesh, running a CFD simulation in OpenFOAM, validating the models, combining the models, and expanding the model by means of a current or obstacle.

1. The first part consists of designing a model based on the Single Stone Model by Manni and Vrijling (1995). This model aims to describe the fall trajectory of a single stone in water following a random walk that occurs due to a lift force acting on the stone caused by vortex shedding. The model is created in Matlab and the physical background behind the model can be found in chapter 3.2.2 and Appendix A. After successfully designing the model, this model is validated using the experimental tests performed by Gelderen (1999).

2. The turbulence model is created using both MATLAB and OpenFOAM. However, first, a geometry and a mesh have to be generated. For this, SALOME is used for different pipe angles, bed heights, and water depths. Additionally, the mesh must contain information about the walls, inlets, outlets, and the atmosphere, which represents the open ocean surrounding the geometry. After generating the mesh it can be exported to OpenFOAM, where the initial and boundary conditions are set to create a simulation. With the DriftFluxFoam solver, different simulations can be performed for different mixture concentrations and initial velocities. The fluid field characteristics are then exported to MATLAB where they can be used to study the influence of the flow on falling stones and model their fall trajectories.

3. Both the model based on the Single Stone Model and the turbulence model are then combined in MATLAB. Additionally, a varying starting location of each stone based on the bed height is added, to create a more realistic model of the stone installation process. The results are then validated by comparing them to the small-scale lab experiments performed by Vehmeijer (2022).

4. After the combined model is validated, the model is expanded by adding additional obstacles, such as a monopile, or an ambient current. Their influence on the flow and the dispersion is then studied.

6.2. Equations of motion

Modeling the falling trajectory of a stone starts with the equation of motion. The relevant forces and their contributions are discussed in chapter 3.2 and the equation of motion is given in equation 3.5. It should be noted, however, that during the descent of the stone it accelerates. As a result of this, an additional term is required in the equation of motion to add extra inertia to the system. This is due to the fact that an accelerating object displaces the surrounding fluid as it moves through it causing the fluid the exert an additional force on the object which results in the object appearing to have a greater mass than it actually has. The added mass term is usually modeled as a fraction of the mass of the fluid displaced by the stone depending on its size, shape, or Reynolds number. For a sphere the added mass (M_a) used for this model is given by (Ravelli, 2009):

$$M_a = \frac{1}{12}\pi\rho_f D^3 \tag{6.1}$$

The motion equation describing the trajectory of the falling stone, as previously described in equation 3.5, can now be modified by adding the added mass term. As a result, the new motion equations can be expressed by the following equations.

$$(M + M_a) \cdot \frac{dv}{dt} = F_g + F_b + F_d \tag{6.2}$$

$$(M + M_a) \cdot \frac{du}{dt} = F_L \tag{6.3}$$

By substituting the equations for the gravitational force (F_g), buoyancy force (F_b), and drag force (F_d), the differential equations for both the vertical velocity (v_s) and the horizontal velocities (u_{s_x} & u_{s_y}) can be expressed, respectively, as (Kevelam, 2016):

$$(M + M_a)\frac{dv_s}{dt} = \frac{1}{8}A_s C_D \rho_f |\vec{u}| \left(\overline{v_f} - v_s\right) + V\left(\rho_s - \rho_f\right) g \tag{6.4}$$

$$(M + M_a)\frac{du_{s_x}}{dt} = \frac{1}{2}A_L C_L \rho_f |\vec{u}| \left(\overline{u_{f_x}} - u_{s_x}\right) \tag{6.5}$$

$$(M + M_a)\frac{du_{s_y}}{dt} = \frac{1}{2}A_L C_L \rho_f |\vec{u}| \left(\overline{u_{f_y}} - u_{s_y}\right) \tag{6.6}$$

where,

ρ_s	=	density of rock	$[kg/m^3]$
ρ_f	=	density of the fluid	$[kg/m^3]$
g	=	gravitational constant	$[m/s^2]$
C_D	=	Drag coefficient	$[-]$
C_L	=	Lift coefficient	$[-]$
D	=	Diameter	$[m]$
A_s, A_L	=	Reference area	$[m^2]$
V	=	Volume	$[m^3]$

The drag coefficient,C_d, and the lift coefficient, C_L, are different for each stone. In the model, the drag coefficient is therefore defined by a normal distribution, where mean value and standard deviation are calculated using a relation previously described by van der Wal (2002):

$$\mu_{C_D,n} = 0.54 \cdot \frac{L}{d} + 0.42 \tag{6.7}$$

$$\sigma_{\mathrm{C_D},n} = 0.30 \tag{6.8}$$

Where L is the largest distance between two ends of a stone and d is the minimal distance between two ends. The ratio $\frac{L}{d}$ then describes the shape of the stone causing different values for the drag coefficient.

To further account for the irregular shape of the stone the lift coefficient (C_L) is estimated using the expressions proposed by (De Reus, 2004), given by:

$$C_L = \sqrt{0.5 C_D} \tag{6.9}$$

Lastly, the absolute velocity $\vec{u}$ is defined as:

$$\vec{u} = \sqrt{\left(u_{f_x} - u_{s_x}\right)^2 + \left(u_{f_y} - u_{s_y}\right)^2 + \left(v_f - v_s\right)^2} \tag{6.10}$$

Where the mean component of the horizontal and vertical fluid velocities, denoted as $\overline{u_{f_x}}$, $\overline{u_{f_y}}$ and $\overline{v_f}$, respectively, is determined by the fluid field. The horizontal and vertical velocities of the stone are denoted as u_{s_x}, u_{s_y}, and v_s, respectively.

6.3. Single Stone Model

This section aims to model the trajectory of stones descending in water without an initial velocity based on the Single Stone Model by Manni and Vrijling (1995). First, the background of the model is elaborated, the complete physical background behind this model can be found in Appendix A.

6.3.1. Background

In practice, when stones are installed, they are usually irregular in shape and have differences in roughness or smoothness. These properties have the consequence, due to different physical processes occurring as described in chapter 3.2.2, that the stones have to endure different 'random' forces that lead to an acceleration in a random direction. As a result of this, the trajectory that the stones will follow can be described as a random walk. The falling trajectory of a single stone is described in the Single Stone Model (Cregten, 1995). Figure 6.1 displays the random walk that a single stone can follow, the numbers displayed indicate the number of possibilities at which the stone can reach each point. An important note is that each incremental displacement step Δh is directionally independent of the previous step. This means that, if a large amount of stones is released at the same starting location, a normal distribution will be formed at the seabed with a mean displacement of 0.

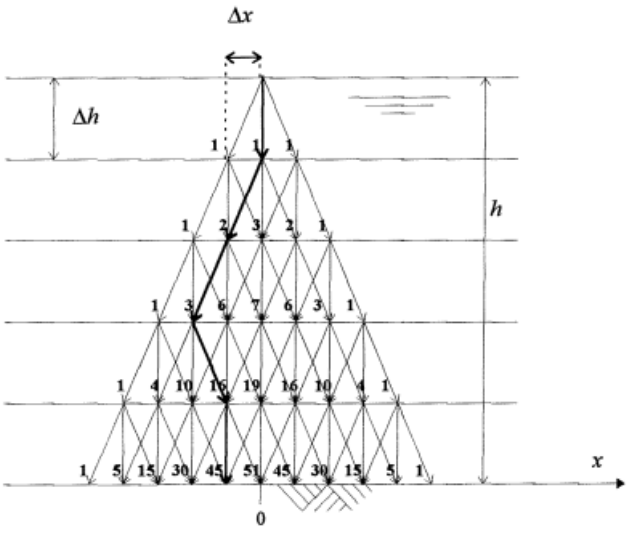

Figure 6.1: Schematic representation of the random walk model by Cregten (1995)

The number of changes in the direction of the "horizontal" acceleration during the fall of the stone over the water depth is approximately (Manni & Vrijling, 1995):

$$N \approx \frac{h}{s_{\Downarrow}} \quad \text{or:} \quad N \approx \frac{h \cdot St}{2\pi D} \tag{6.11}$$

in which,

N = number of directional changes of the "horizontal" acceleration during the stone's fall over the water depth

h = water depth

The central limit theorem (CLT) in probability theory states that when a large number of independent random variables are summed up and then normalized, the resulting distribution will tend toward a normal distribution even when the original variables are not normally distributed. Based on this theorem it can be stated that the stones, which are traveling along a random path, are normally distributed. The stochastic variable is, in this case, the horizontal displacement of the stone for one step. This displacement is the same for each step. The resulting probability density function of the stones reaching the seabed is described by:

$$f_X(x) = \frac{1}{\sqrt{2\pi} \cdot \sigma_N} * e^{-\frac{1}{2}\left(\frac{x-\mu_x}{\sigma_N}\right)^2}, \quad \text{with } \sigma_N = c' \sqrt{h \cdot D_{n50}} \tag{6.12}$$

Where X is the total horizontal displacement in the x-direction, the constant value c'=0.685 (Gelderen, 1999) the location where the stone arrives at the seabed is depicted by x, σ_N is the standard deviation of the total horizontal displacement and μ_x is the mean of X, which, in theory, equals the x-coordinate of the starting position of the stone.

This model can be extended from a two-dimensional model to a three-dimensional one. The three-dimensional probability density function can be determined by taking the product of both the probability density function in the x direction and the y direction under the assumption that the displacements in both directions are independent of each other. The three-dimensional probability density function is then given by:

$$f_{\underline{X,Y}}(x,y) = f_{\underline{X}}(x) \cdot f_{\underline{Y}}(y) = \frac{1}{\sigma_N^2 \cdot 2\pi} \cdot e^{-\frac{1}{2}\left(\frac{(x-\mu_x)^2+(y-\mu_y)^2}{\sigma_N^2}\right)} \tag{6.13}$$

The visual representation of the probability density function in two dimensional form is depicted in figure 6.2:

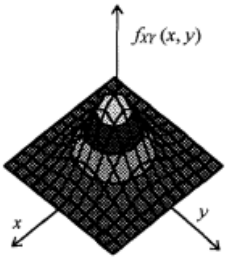

Figure 6.2: Two-dimensional probability density function of the horizontal displacement from a single stone by Cregten (1995)

The single stone model was verified by Gelderen (1999). His final conclusion was that only a portion (more than 50%) of the stones may be accurately represented by the physical derivation of the Single Stone Model. This is because other falling movements occur besides the random walk of stones, one of which is the Magnus effect. Nevertheless, a model that can be utilized in practice is the proportionality of the distribution of the stones with the root of the product of the water depth and the typical stone

diameter assumed in the Single Stone Model. The distribution of the stones can be accurately predicted using the Single Stone Model (Gelderen, 1999).

De Reus (2004) combined the Offset Model by Konter (1983) with the Single Stone Model to study the influence of the current on the Single Stone Model. The probability density function in the x direction that was described by De Reus (2004) is given by:

$$f_{\underline{X}}(x) = \frac{1}{\sigma_N \sqrt{2\pi}} \cdot e^{-\frac{1}{2}\left(\frac{x-h\frac{\sqrt{C_D/2}\cdot u_{current}}{\sqrt{g\cdot D_n\cdot\Delta}}}{\sigma_N}\right)^2}, \quad \text{with } \sigma_N = c'\sqrt{h\cdot D_n} \tag{6.14}$$

De Reus (2004) also noted that the effect of the ambient current on the displacement of stones is amplified as the current's flow velocity increases. This can be seen in the increased dispersion of stones as 'unmixing' increases, meaning that the smaller stones move relatively further due to their lower weight, resulting in a wider dispersion. The spread in the x direction increases with the flow velocity. This is also reflected by the difference between the spread in the x and y directions. At higher flow velocities, the 'unmixing' of the stones does not affect the distribution of the stones' displacements. These follow a normal distribution and a Rayleigh distribution as expected by statistics. The Single Stone Model is therefore also valid for stone installation within a current, despite the 'unmixing' that occurs.

6.3.2. Model

The Single Stone Model assumes a stone falling at a constant rate following a random walk, as such, the vertical forces that act upon the stone will balance each other to achieve an equilibrium at which the stone reaches its terminal velocity. In the model, the terminal velocity of the stone is given by:

$$w = \sqrt{2\frac{\nu}{\xi} D\Delta \frac{g}{C_D}} \tag{6.15}$$

with:

$$\Delta = \frac{\rho_s - \rho_f}{\rho_f}$$

where,

$\nu =$ Shape factor (for a cube $\nu = 1$, for a sphere $\nu = \frac{\pi}{6}$) [-]
$\xi =$ Shape factor (for a cube $\xi = 1$, for a sphere $\xi = \frac{\pi}{4}$) [-]

However, using these shape factors can lead to confusion. Therefore, to avoid confusion, this equation can also be written as (equation 3.9):

$$w = \sqrt{\frac{V}{A_s}\Delta \frac{g}{C_D}} \tag{6.16}$$

In this equation, the shape factors are replaced by the volume of the stone V and the frontal area A_s. This gives a more comprehensible equation that can be used more easily.

The horizontal acceleration can be obtained from the lift force, F_L, and Newton's second law ($F_L = Ma$). The lift force was previously discussed in section 3.2.2 and is described by equation 3.18. Rewriting the equation gives a relation for the acceleration in the direction of the lift force gives the following equation:

$$\frac{du}{dt} = \frac{\zeta \cdot \rho_f \cdot w^2 \cdot \mathrm{D}^2 \cdot \mathrm{C_L}}{\rho_\mathrm{s} \cdot \mathrm{D}^3} \tag{6.17}$$

Here, C_L is the lift coefficient and ζ is another shape factor that is dependent on the direction of the flow in connection with the orientation of the stone and on the sharpness of the edges of the stone (Manni & Vrijling, 1995). This shape factor, ζ, is not easily determined as stones are usually irregular in

shape. As a result, the value of this factor will be determined during the validation phase in section 6.3.3, where the model's performance will be compared against experimental data conducted by Gelderen (1999), which documented various experiments of a stone group released at different water depths.

The direction in which the stone accelerates is dominated by the effect of vortex shedding. This means that the period of a vortex shedding at a constant fall rate can be described using Strouhal's number (section 3.2.2). The Strouhal number (St) is described by:

$$\mathrm{St} = \frac{\omega \cdot \mathrm{D}}{w} = \frac{2 \cdot \pi}{\mathrm{T}} \cdot \frac{\mathrm{D}}{w} \tag{6.18}$$

where,

$\omega =$	radial frequency	$[1/s]$
$\mathrm{T} =$	Period of vortex shedding	$[s]$

The Strouhal number also depends on the Reynolds number (Re). As a result, within the region $10^2 \leq Re \leq 10^5$, the Strouhal number only varies between 0.18 and 0.22. As the Reynolds number stays within this region during the stone's fall, the Strouhal number can be assumed constant. After rewriting equation 6.18, the following equation is found for the period of vortex shedding (T):

$$\mathrm{T} = \frac{2 \cdot \pi \cdot \mathrm{D}}{\mathrm{St} \cdot w} \tag{6.19}$$

This period of vortex shedding (T) describes the time it takes for one vortex to shed. During each period a certain lift force acts on the stone causing an acceleration, as described by equation 6.17, in the direction of said lift force.

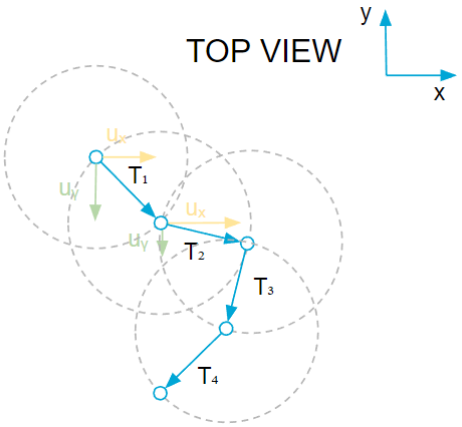

Figure 6.3: A top-view schematic illustration of the random walk process

The random walk a stone follows according to the single stone model is illustrated in figure 6.3. The stone is assumed to fall at its terminal velocity, resulting in a constant period of vortex shedding (T) for each step. The direction in which the stone has a horizontal acceleration during each step is uniformly distributed over the range of 0 to 2π.

The equation of motion describing the trajectory of a falling stone, as previously described in equations 6.4- 6.6, can be used to model its fall trajectory in MATLAB. However, the Single Stone Model assumes that the stone travels through stagnant water at its terminal velocity and hence does not require the velocities defined by the fluid field, u_f and v_f, in the equation. Due to the stone's acceleration in different horizontal directions during its descent, the added mass term remains in the equation. The differential equations in both the vertical and horizontal directions can be expressed, respectively, as:

$$(M+M_a)\frac{dv_s}{dt} = \frac{1}{8}A_s C_D \rho_f |U| v_s + V\left(\rho_s - \rho_f\right) g \tag{6.20}$$

$$(M+M_a)\frac{du_{s_x}}{dt} = \frac{1}{2}A_L C_L \rho_f |U| u_{s_x} \tag{6.21}$$

$$(M+M_a)\frac{du_{s_y}}{dt} = \frac{1}{2}A_L C_L \rho_f |U| u_{s_y} \tag{6.22}$$

where, the absolute velocity (U) is defined as:

$$U = \sqrt{u_{s_x}^2 + u_{s_y}^2 + v_s^2} \tag{6.23}$$

Where v_s is the vertical velocity of the stone and u_{s_x}, u_{s_y} are the horizontal velocities of the stone. Due to the fact that the Single Stone Model assumes the stone travels at its terminal velocity immediately after release (without acceleration), it is also possible to use the terminal velocity (w) described by equation 6.16 instead of the velocity described by the differential equation (eq. 6.20).

The random displacement in horizontal directions as described by the Single Stone Model can be added to this motion equation by means of an extra velocity component, u_{SSM}. This component is found after rewriting equation 6.17:

$$u_{SSM} = \frac{\zeta \cdot \rho_f \cdot w^2 \cdot \mathrm{D}^2 \cdot \mathrm{C_L}}{\rho_\mathrm{s} \cdot \mathrm{D}^3} \cdot \Delta t \tag{6.24}$$

Due to the fact that the horizontal direction in which the stone accelerates during each step is uniformly distributed over the range of 0 to 2π, the velocity of this extra component (u_{SSM}) can be written as two components, namely, u_{SSM_x} and u_{SSM_y}:

$$u_{SSM_x} = u_{SSM} \cdot \cos(r \cdot 2\pi) \tag{6.25}$$

$$u_{SSM_y} = u_{SSM} \cdot \sin(r \cdot 2\pi) \tag{6.26}$$

Where r is a uniformly distributed random number that lies between the interval [0,1].

The acceleration caused by vortex shedding, as explained by the Single Stone Model, can be defined as a fluctuating velocity around the mean velocity of the stone. As a result, not only the mean part of the stone velocity u_s has to be taken into account but also the value of the fluctuating part:

$$u_{s_x} = u_{SSM_x} + \overline{u_{s_x}} \tag{6.27}$$

$$u_{s_y} = u_{SSM_y} + \overline{u_{s_y}} \tag{6.28}$$

The new differential equations describing the fall trajectory of a stone are now given by:

$$(M+M_a)\frac{dv_s}{dt} = \frac{1}{8}A_s C_D \rho_f |U| \overline{v_s} + V\left(\rho_s - \rho_f\right) g \tag{6.29}$$

$$(M+M_a)\frac{du_{s_x}}{dt} = \frac{1}{2}A_L C_L \rho_f |U| (\overline{u_{s_x}} + u_{SSM_x}) \tag{6.30}$$

$$(M+M_a)\frac{du_{s_y}}{dt} = \frac{1}{2}A_L C_L \rho_f |U| (\overline{u_{s_y}} + u_{SSM_x}) \tag{6.31}$$

where, the absolute velocity (U) is defined as:

$$U = \sqrt{\overline{u_{s_x}}^2 + \overline{u_{s_y}}^2 + \overline{v_s}^2} \tag{6.32}$$

Important to note here is that $\overline{u_{s_x}}$, $\overline{u_{s_y}}$ and $\overline{v_s}$ are the mean velocity components. By means of discretization, the model can be implemented in MATLAB to compute the stone's fall trajectory. Each of the differential equations can be discretized to get the velocity at the next time step:

$$v_s^{n+1} = \left(\frac{1}{8} A_s C_D \rho_f \left|U^n\right| \left(v_s^n\right) + V\left(\rho_s - \rho_f\right) g\right) \cdot \frac{\Delta t}{(M + M_a)} + v_s^n \tag{6.33}$$

$$u_{s_x}^{n+1} = \left(\frac{1}{2} A_L C_L \rho_f \left|U^n\right| \left(u_{s_x}^n + u_{SSM_x}^n\right)\right) \cdot \frac{\Delta t}{(M + M_a)} + u_{s_x}^n \tag{6.34}$$

$$u_{s_y}^{n+1} = \left(\frac{1}{2} A_L C_L \rho_f \left|U^n\right| \left(u_{s_y}^n + u_{SSM_y}^n\right)\right) \cdot \frac{\Delta t}{(M + M_a)} + u_{s_y}^n \tag{6.35}$$

where,

n	=	current time step	$[-]$
$n+1$	=	next time step	$[-]$
Δt	=	time step	$[s]$

The position of a stone and its new position after each time step can be described using a Cartesian coordinate system with coordinates in the x, y, and z directions. The positions can be calculated using the following equations:

$$x_s^{n+1} = x_s^n + u_{s_x}^{n+1} \cdot \Delta t \tag{6.36}$$

$$y_s^{n+1} = y_s^n + u_{s_y}^{n+1} \cdot \Delta t \tag{6.37}$$

$$z_s^{n+1} = z_s^n + v_s^{n+1} \cdot \Delta t \tag{6.38}$$

6.3.3. Validation

Validation of the model will be performed by comparing the model results to experiments previously performed by Gelderen (1999) and verified by comparing it to the analytical solution suggested by the Single Stone Model. This way, it can be determined whether the model is consistent with the observed results. This is important to ensure that the model can be used to make future predictions about the stones' fall trajectory and final seabed distribution under different circumstances. Validation can also help to identify certain limitations of the model or areas where it may be inaccurate or incomplete.

To be able to correctly validate the model, it is important that the exact same parameters are used as in the experiments performed by Gelderen (1999). The parameters used during this validation are based on stone group A from Gelderen (1999). The characteristics of each individual stone can be found in Appendix B. Furthermore, parameters used to model the stones are also required. It is important to note that the shape factor ζ is determined by tuning the model as a result of the irregular shapes of the stones. This value can be different depending on the characteristics of the stone group. The complete list of parameters used for the modeling of stone group A is presented in the table below:

Table 6.1: List of parameters for stone group A

	Value	Unit
Number of stones	220	[-]
L/d	1.85	[-]
Diameter D_{n50}	11.2	[mm]
Density water ρ_f	1020	[kg/m^3]
Density stones ρ_s	3000	[kg/m^3]
Strouhal number St	0.2	[-]
Drag coefficient C_D	1.42	[-]
Shape factor ξ	1	[-]
Shape factor ν	1	[-]
Shape factor ζ	3.5	[-]

In his experiments, Gelderen (1999) used 220 different stones to research the dispersion of falling stones at various different heights. Therefore, the model created in MATLAB will also use 220 stones. Figure 6.4 shows the side view from a MATLAB simulation. It shows a correct representation of a random walk model with various directional changes that was previously depicted in figure 6.1.

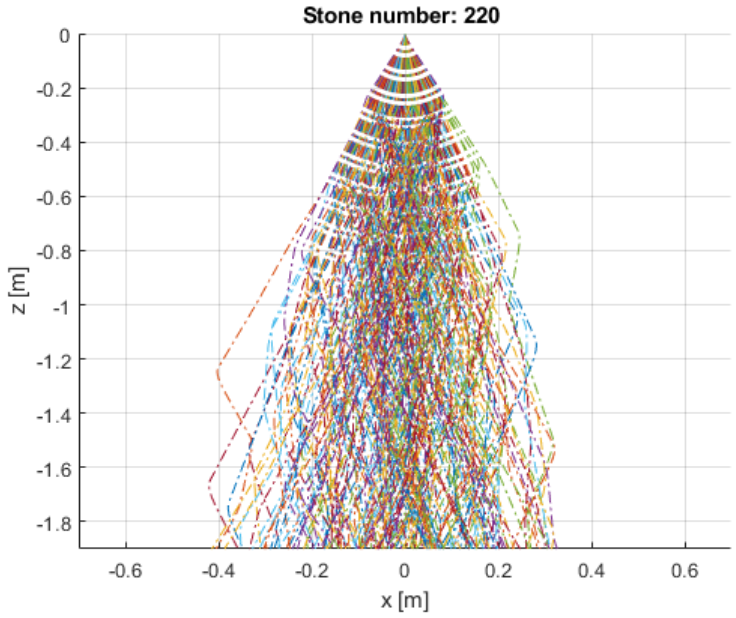

Figure 6.4: Side view from the computed stones' trajectories

The model can be further validated by comparing the stone distributions at the seabed resulting from both the model and the experiments. Figures 6.5a and 6.5b show the distribution at the seabed for both the model and the experiments, respectively, in which the stones were dropped from a height of 1.90 meters.

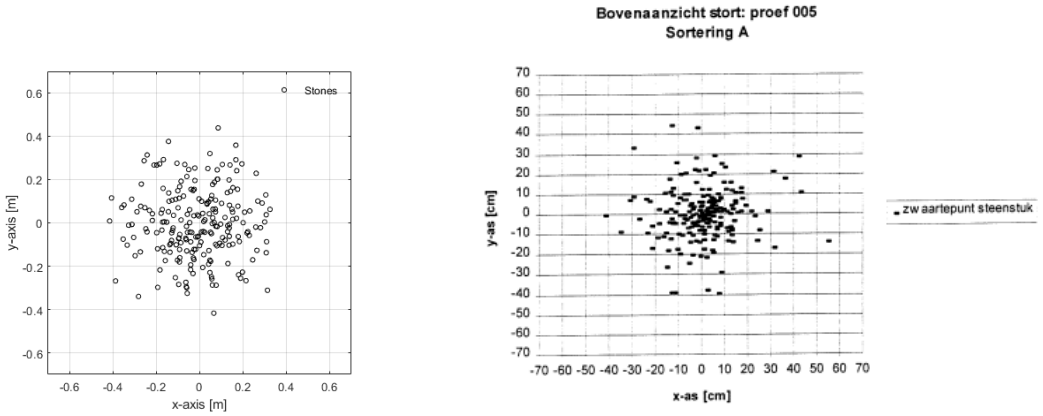

(a) Top view of the stones computed with the model

(b) Top view of the stones achieved by experiments by Gelderen (1999)

Figure 6.5: Final distribution of the stones at the seabed at a height of $h = 1.90m$

In addition to comparing the top view of both samples, a cumulative Rayleigh distribution function is used to analyze the deviation of each stone at the seabed with respect to the mean. This function can be used to compare the probability that a certain deviation will be within a certain range of values.

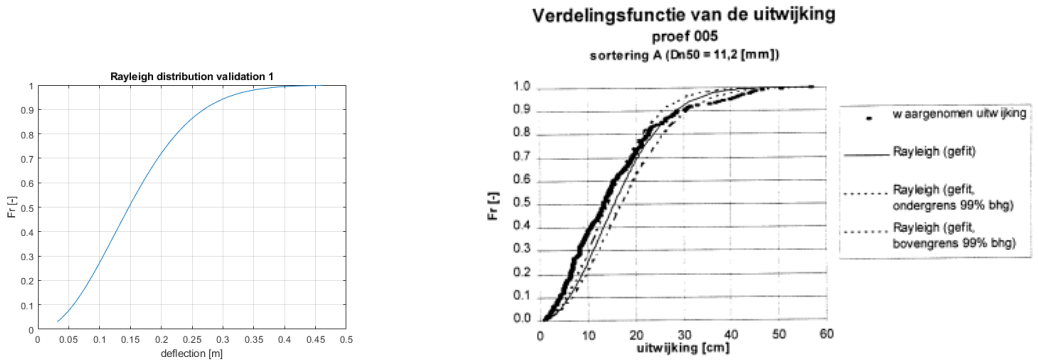

(a) Rayleigh distribution computed with the model

(b) Rayleigh distribution of the experiments by Gelderen (1999)

Figure 6.6: Rayleigh distribution of the total deflection at a height of $h = 1.90m$

The assumption made in the Single Stone Model regarding the proportionality of the distribution of stones with both the square root of the water depth and the square root of the characteristic stone diameter is a useful modeling approach. Manni and Vrijling (1995) then used a student t-test to determine that the value for the constant of proportionality (c') is 0.685. This way the standard deviation of stones can be described by the following equation:

$$\sigma = c' \cdot \sqrt{h \cdot D_{n50}} \tag{6.39}$$

where,

σ	=	Stone dispersion according to the SSM constant (c'=0.685)	$[-]$
h	=	water depth	$[m]$
$D_{n\,50}$	=	Nominal diameter	$[m]$

The experiments performed by Gelderen (1999) used the horizontal deviation $r_{39.35\%}$ of the stones, described by 39.35% of the stones with the smallest deviations out of the total number of measured stones. The values for $r_{39.35\%}$ can be obtained from the cumulative Rayleigh distribution for each experiment. After analyzing the $r_{39.35\%}$ of both the model and the experiments at the different water depths at which the experiments were performed, the model can be verified by comparing it to the analytical solution of the Single Stone Model (eq. 6.39) and validated by comparing it to the experimental data. The results of the experiments can be plotted as $\sigma - h$, along with the predicted distribution of the stones using the SSM and the new model. Figure 6.7 provides insight into the extent to which the new model corresponds to the SSM and the experiments.

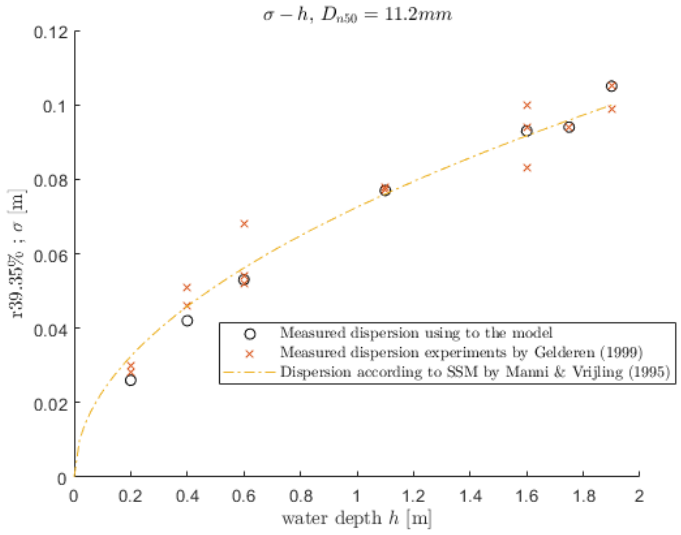

Figure 6.7: $\sigma - h$ Stone group A

From figure 6.7, it can be concluded that the model corresponds sufficiently to both the analytical solution suggested by the Single Stone Model as well as the results obtained by the experiments.

An additional observation is found in the model at lower water depths. When the stone is released at a lower depth it appears that a ring is formed around the point of release, see figure 6.8. This ring formation can be explained using equation 6.11. As a result of the Strouhal number to be assumed constant, the number of directional changes of the horizontal acceleration during the descent is proportionate to the water depth divided by the diameter of the stone, $N \sim \frac{h}{D}$. When N has a value around 1, a ring is formed due to the stones having an acceleration in the same direction for the entire fall duration. This is because, according to the Single Stone Model, there is not enough time for another vortex to shed. Therefore when the h/D ratio is small a ring will be formed on the seabed.

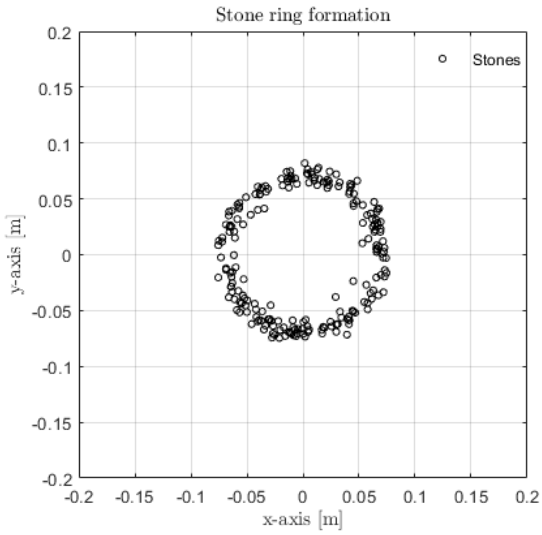

Figure 6.8: Dispersion forming a ring at the seabed

In reality, the formation of a ring as predicted by the model may not always occur due to the varying physical properties of stones. The model accounts for variations in the drag coefficient of each stone,

whereas in reality, the stones will vary across a much wider range of their characteristics. Nonetheless, it is important to note that ring formations have been observed in real-world experiments, such as those conducted by van Oord (1996). According to the findings reported by van Oord (1996), the formation of a ring can also be attributed to the Magnus effect, whereby the stones rotate during their fall, causing them to deviate at a constant rate from the vertical axis through the release point.

6.4. Turbulence model

In order to account for the jetting effect that occurs below the fallpipe and the initial velocity of the stones, a turbulence model is required to describe the fall trajectory of the stones. Stones and water that exits the fallpipe can be viewed as a mixture. The concentration of this mixture is obtained using the sliding bed model by Vehmeijer (2022). As the stones are relatively large in size, the effects at the boundary layers have little impact on their trajectories. Therefore, as it is not necessary to consider the near-wall flow behavior, the $k-\varepsilon$ model is the preferred model to calculate turbulent flow. Furthermore, the $k-\varepsilon$ model has a low mesh requirement and works well with limited computational power.

This section uses the methodology proposed by Kevelam (2016), where turbulence is defined as a fluctuating velocity term around the mean velocity. The underlying concept of this model is to introduce a characteristic timescale, such that the modeled turbulence has the same intensity and direction as that observed in a real-world eddy. Both the production and the depth of the water are kept constant in the simulations in this section to reduce the number of simulations that have to be run. These, and the other parameters kept constant in this section, are provided in the table below.

Table 6.2: Constant parameters turbulence model

	Value	Unit
Stone density ρ_s	2650	[kg/m^3]
Fluid density (water) ρ_f	1025	[kg/m^3]
Kinematic viscosity (water) μ	$1.42 \cdot 10^{-6}$	[m^2/s]
Gravitational constant g	9.81	[m/s^2]
Production P	400	[kg/s]
Water depth h	6	[m]

The water depth is set at 6 meters because the baseline operations will be performed around this water depth. Production is set at a relatively low but comparable production rate to the experiments performed by Vehmeijer (2022) to obtain a better indication of the validity of the model.

6.4.1. Mesh generation

During numerical modeling, first, a mesh is required to be able to discretize the physical domain, which has an infinite number of infinitely small elements, into a finite number of smaller elements. Using these smaller elements it becomes possible to solve the system numerically, which, usually, consists of partial differential equations which cannot be solved analytically. It is important to note that the mesh has to be well-designed to be able to accurately solve these equations. When the mesh is poorly designed it leads to an unstable solution which then becomes inaccurate. As a result, a mesh shouldn't be too coarse as it would not represent reality well and thus be inaccurate. But a mesh also shouldn't be too fine as it would require too much computation time. Therefore, it is important to carefully design the mesh to obtain accurate and efficient numerical solutions. To ensure the convergence of residual errors a mesh independence study can be performed. This can be done by comparing solutions of different simulations with mesh grids varying from very coarse up to very fine until the solution is converged. The result of a successful mesh generation is shown in figures 6.9a and 6.9b.

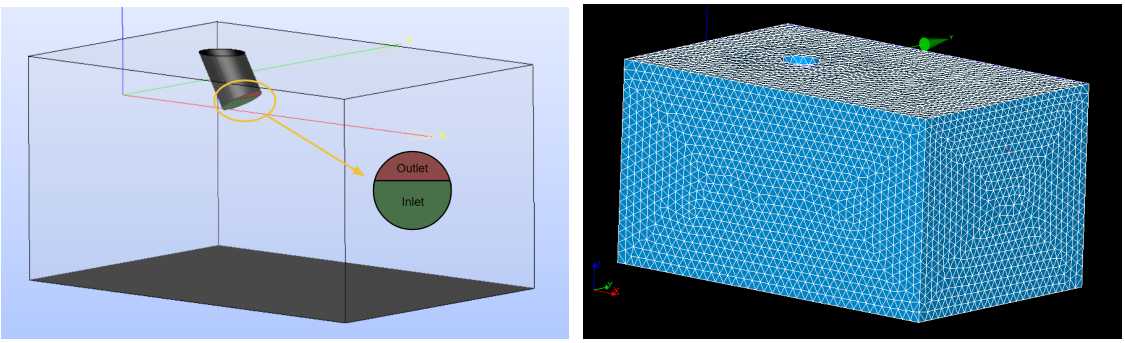

(a) Geometry of the model

(b) Mesh of the model

Figure 6.9: Geometry and Mesh from SALOME consisting of 110,000 elements

The process of creating a mesh starts with building a 3D geometric model. In this study, SALOME was used to generate this 3D geometric model. The geometry, illustrated in Figure 6.10, can be built using either the built-in geometry tools that SALOME provides or by importing a model created in a different 3D modeling software such as FreeCAD. The next step involves labeling and grouping the walls, inputs, and outputs of the created model for OpenFOAM to be able to recognize them.

In this case, it is important to model the stone exit of the fallpipe correctly, see Figure 6.9a. Due to the sliding bed formed inside the fallpipe, the mixture exits the pipe at or below the bed height. This area is therefore defined as the inlet. As a consequence of the mixture exiting the fallpipe through the inlet, water should be able to enter the fallpipe again above the bed height. This area is therefore labeled as the Outlet. The seabed and the pipe itself can be considered walls and can therefore be grouped. Lastly, the area that represents the open ocean should also be considered (The see through walls in Figure 6.9a) and is therefore named the atmosphere.

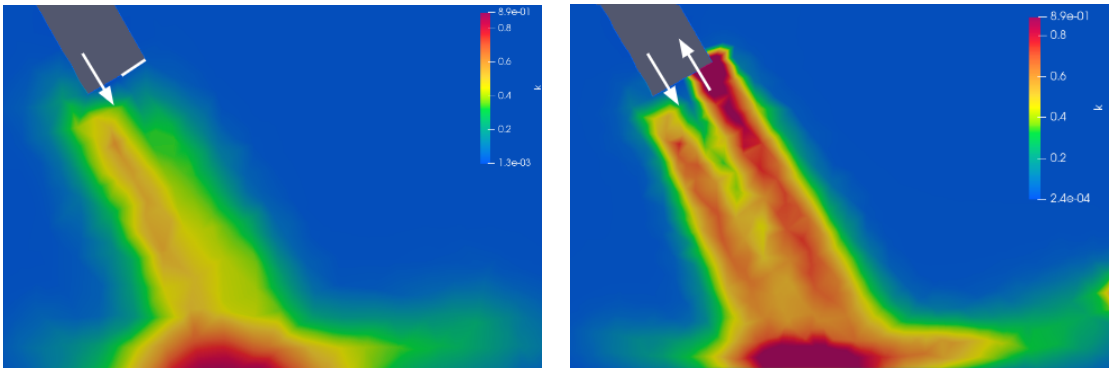

(a) Fallpipe exit modeled as an inlet and a wall

(b) Fallpipe exit modeled as an inlet and an outlet

Figure 6.10: Simulation of the turbulent kinetic energy (k), with different ways of modeling the exit of the fallpipe

The area now labeled as an outlet can also be modeled as a wall, see Figure 6.10a. This way the mixture can still exit the pipe, but water can not enter the pipe. As a result, however, there is no turbulent region formed at the top of the jet, which should exist as can also be seen in figure 6.10b. Therefore, the exit of the fallpipe should be modeled as a combination of an inlet and an outlet.

Using the 3d geometry, a mesh can be created by defining the meshing parameters. After finding a converged solution, the maximum element size for the mesh shown in 6.9b is set at 0.4m, and the minimum element size is 0.2 m. In addition, the mesh refinement is set to moderate and NETGEN 1D-2D and NETGEN 3D are used as the meshing algorithm. Using these settings for generating the mesh, the resulting mesh, shown in figure 6.9b, consists of 110,000 elements. This amount is sufficient

for an accurate result and does not require too much computation power in OpenFOAM. It should be noted that each mesh for either different pipe angles, different water depths, or various bed heights should have its own mesh convergence study to avoid inaccurate results.

After creating a mesh, it is beneficial to check the quality of the mesh. In OpenFOAM, a utility command can be used to check the mesh for overlapping, distorted or invalid cells. By checking the mesh before simulation, it is possible to find any potential problems before starting the simulation.

6.4.2. OpenFOAM

This study uses OpenFOAM to model a simulation using the driftFluxFoam solver. The driftFluxFoam solver is used to simulate the motion of a mixture of particles (stones) and a fluid (water). It takes into account the effect of gravity and particle settling, and is therefore useful for simulating the dispersion of stones. Having the right initial and boundary conditions is important to reduce the computation time and improve the accuracy of the model. The initial conditions refer to the values of the parameters set at the start of the time simulation (at 0 time), while the boundary conditions describe the behavior at the boundaries. It is important to note that the initial conditions for the turbulent kinetic energy, dissipation rate, and viscosity are used only as an initial guess. OpenFOAM will correct for the right values relatively quickly, but a better guess still leads to a faster computation time. To calculate these initial guesses, the following equations can be used.

For isotropic turbulence, the initial turbulent kinetic energy, k, can be estimated by (OpenCFD, 2021):

$$k = \frac{3}{2}\left(I\left|u_{ref}\right|\right)^2 \tag{6.40}$$

where,

I	=	Turbulence intensity	[%]
u_{ref}	=	A reference flow speed	$[m/s]$

For isotropic turbulence, the initial turbulence dissipation rate, ε, can be estimated by (OpenCFD, 2021):

$$\varepsilon = \frac{C_\mu^{0.75} k^{1.5}}{l_e} \tag{6.41}$$

where,

C_μ	=	A model constant equal to 0.09 by default	[−]
l_e	=	Eddy length scale	$[m]$

Lastly, the turbulent eddy viscosity, μ_t, is estimated by (Launder & Spalding, 1974):

$$\mu_t = C_\mu \rho k^2/\varepsilon \tag{6.42}$$

The initial guesses are then calculated using formulas 6.40-6.42. For the turbulence intensity (I), a value of 5% is used at the edges and 10 % at the inlet. The reference length scale (l_e) can be approximated using $l = 0.07 D_{pipe}$ (OpenCFD, 2021). This gives an initial value of around 0.1 m, and the reference flow speed (u_{ref}) is set at 4.5 m/s. As a result of the fallpipe being positioned at an angle, the initial velocity of the mixture at the inlet is expressed in its 3-dimensional vector form. Furthermore, due to the stones being modeled as a mixture, another parameter, denoted as *alpha.sludge* is used in which the initial concentration of the stones at the inlet is described. All the initial and boundary conditions used during the simulation of a fallpipe at an angle of 60 degrees are summarized in the table 6.3.

	U	alpha.sludge	epsilon	k	nut	p_rgh
Inlet	fixedValue uniform (2.3 0 −3.9)	fixedValue uniform 0.06	fixedValue uniform 0.026	fixedValue uniform 0.025	Calculated uniform 0.002	zeroGradient
Outlet	zeroGradient	inletOutlet uniform 0	zeroGradient	zeroGradient	zeroGradient	zeroGradient
Walls	fixedValue uniform (0 0 0)	zeroGradient	epsilonWallFunction uniform 0.1	kqRWallFunction uniform 0.1	nutkWallFunction uniform 0.008	fixedFluxPressure uniform 0
Atmosphere	pressureInletOutletVelocity uniform (0 0 0)	inletOutlet uniform 0	zeroGradient	zeroGradient	zeroGradient	totalPressure uniform 0

Table 6.3: Table consisting of the initial boundary conditions

Small changes in the initial or boundary conditions do not affect the results because OpenFOAM corrects them very fast. Therefore, when looking at different fallpipe angles or different stone sizes/velocities, the only initial conditions in OpenFOAM that must be changed are the inlet velocity (U) and the concentration of the mixture (*alpha.sludge*). Furthermore, it is important to be able to change the height of the bed and the angle of the fall pipe. Both of these parameters can only be changed by creating a new 3d geometry and a new mesh.

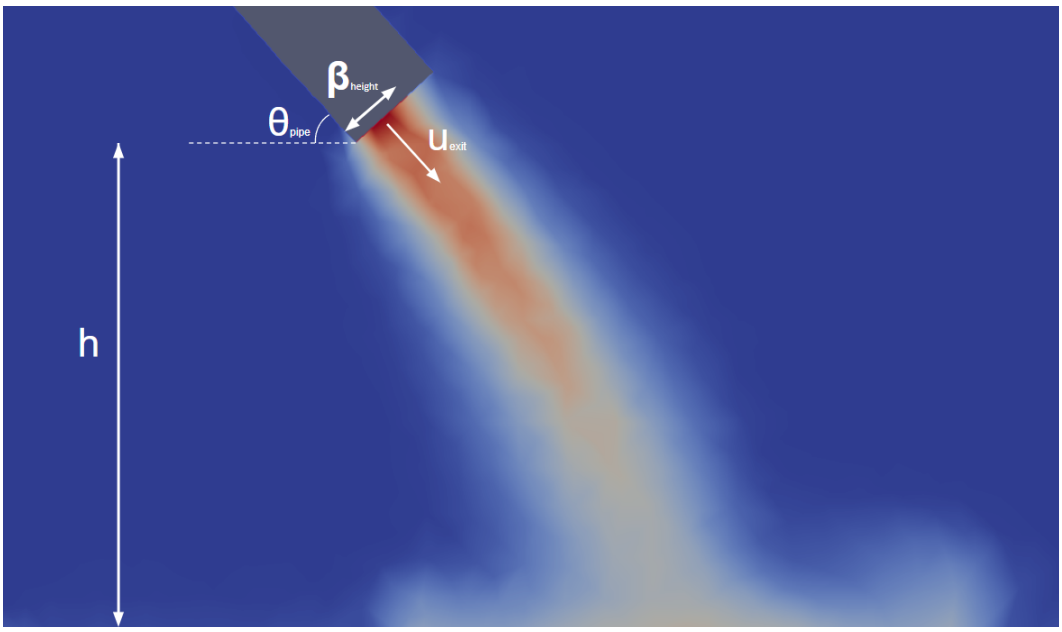

Figure 6.11: Fallpipe and the input parameters provided

Figure 6.11 displays the relevant parameters used during the OpenFOAM simulations resulting from the sliding bed model (SBM), developed by Vehmeijer (2022). The sliding bed model is used to calculate the exit velocity of the stones (u_{exit}), the stone concentration (c) within the mixture and the height of the bed (β_{height}) of the sliding bed inside the fallpipe. For a stone group with a size of $D_{n50} = 175mm$, a water depth $h = 6m$ and a constant production rate of $P = 300kg/s$, the following input parameters are obtained from the sliding bed model:

Table 6.4: Input parameters obtain by the SBM from Vehmeijer (2022)

	Value	Unit
Volumetric concentration c_v	6	[%]
Fallpipe exit velocity u_{exit}	4.5	[m/s]
Bed height β_{height}	1.1	[m]
Fallpipe angle θ_{pipe}	60	[degrees]

After solving the simulation using driftFluxFoam, the results can be reviewed using Paraview. It is determined that the steady-state condition is achieved after around 6 seconds. As a result, the results obtained by the simulation at this time step will be used for further calculations. The results of the simulation at time $T = 6s$ are shown in Figure 6.12.

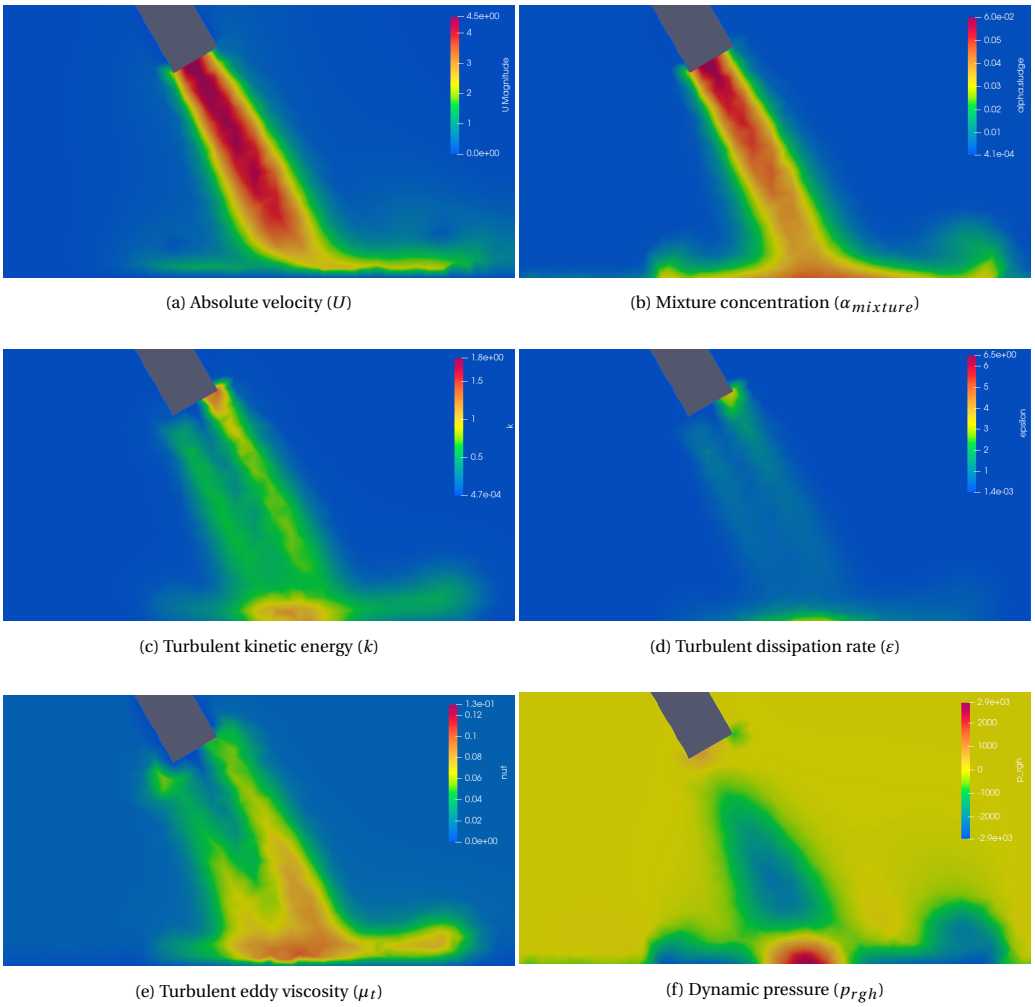

(a) Absolute velocity (U)

(b) Mixture concentration ($\alpha_{mixture}$)

(c) Turbulent kinetic energy (k)

(d) Turbulent dissipation rate (ε)

(e) Turbulent eddy viscosity (μ_t)

(f) Dynamic pressure (p_{rgh})

Figure 6.12: Results from OpenFOAM simulation illustrated as a 2D slice using Paraview

Based on the results shown in Figure 6.12, the following observations can be made:

- The jet maintains its initial velocity for a long duration, which causes the mixture to settle further away from the fallpipe.
- A large amount of turbulent kinetic energy is visible around the outlet. This may occur due to the conservation of mass, where the difference in cross-sectional area from the inlet and the outlet causes the velocity of the fluid to increase, increasing kinetic energy. Additionally, the sudden expansion of the flow area can create eddies and vortices that contribute to the turbulence in the surrounding area.
- An increase in turbulent kinetic energy can also be observed at the seabed. This can be explained by the jet interacting with the boundary layer. As it approaches the seabed, it encounters slow-moving water near the bottom. This may lead to the formation of turbulent eddies. These eddies cause mixing of the jet and the water to occur, leading to an increase in turbulent kinetic energy.

The seabed itself can also cause the formation of eddies, this can further increase the turbulence in the area. Lastly, it can also be explained due to the particles settling at the seabed.

The results of the simulations can be exported to MATLAB, where they can be used to describe the fall trajectories of stones based on the fluid field.

6.4.3. MATLAB

Matlab will be used to model the trajectories of stones by implementing the influence of turbulence on their velocities in all directions as a result of them traveling through a fluid (in this case water). The first step is to interpolate the data obtained from OpenFOAM, then the fluctuating velocity terms, that occur due to turbulence, are calculated using a discrete random walk model. These fluctuating velocity terms are subsequently integrated into the motion equations to model the fall trajectories of the stones.

Fluid field interpolation

As a result of the mesh being designed in SALOME, it consists of tetrahedral shapes, which is considered an unstructured mesh. To be able to model the fall trajectory of the stones in MATLAB it has to be converted to a structured, square mesh. Interpolation can be used to achieve this. By using interpolation, it is possible to approximate the value of the data points in a regular grid from the values of the data points in an irregular grid. The accuracy of the interpolation will depend on the quality of the mesh and the chosen interpolation method as can be seen in Figures 6.13a-6.13c.

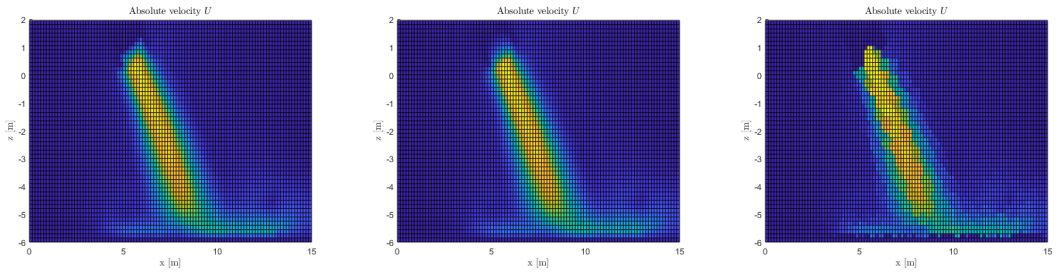

(a) Linear (b) Natural (c) Nearest neighbor

Figure 6.13: Different interpolation methods in Matlab with a grid size of 0.15m

From Figure 6.13 it follows that the nearest neighbor method does not give an accurate result. Therefore, either linear interpolation or natural interpolation has to be used. Linear interpolation fits a straight line between data points and therefore assumes the function changes linearly between them, while natural interpolation fits a curve with a polynomial of a higher degree that passes through all data points. As a result, the natural interpolation is more accurate. However, due to the linear method having a substantially faster computation time, and the observed difference in accuracy being minimal, the linear method will be used in this research to interpolate the data to a regular grid.

Motion equations

As discussed previously, to model the trajectory of stones below the fallpipe, it is necessary to determine their initial values. Figure 6.11 displays the relevant parameters resulting from the sliding bed model. The sliding bed model (SBM), developed by Vehmeijer (2022), is used to calculate the exit velocity of the stones (u_{exit}), the concentration of stones (c) within the mixture, and the height of the bed (β_{height}) of the sliding bed inside the fallpipe. The initial velocity of a stone used in the motion equations is defined as the sum of the velocity of the jet and the exit velocity of the stone. As a result of the orientation of the fallpipe, which is rotated around the y-axis under an angle (θ_{pipe}), the initial velocity in the y-direction is assumed to be zero. As a result, the initial velocities are defined as follows:

$$v_s = v_f + u_{exit} \cdot \sin(\theta_{pipe})$$
$$u_{s_x} = u_{f_x} + u_{exit} \cdot \cos(\theta_{pipe})$$
$$u_{s_y} = 0$$

where u_{exit} is the exit velocity of the stones calculated by the sliding bed model, θ_{pipe} is the angle at which the fall pipe is placed, and v_f, u_{f_x} are the fluid velocities in the corresponding directions.

The motion equations used in the turbulence model will be based on the motion equations previously described in section 6.2. Unlike the Single Stone Model, in which fluid velocities were not included due to the water being stagnant, it is essential to account for these velocities in this case. Additionally, the added mass term is required, due to the volume of the surrounding water being displaced as the stones move through it.

The motion equations (6.4-6.6) can be discretized to obtain the velocities in each direction at the next time step.

$$v_s^{n+1} = \left(\frac{1}{8} A_s C_D \rho_f \left|\vec{u}^n\right| \left(v_f^n - v_s^n\right) + V\left(\rho_s - \rho_f\right) g\right) \cdot \frac{\Delta t}{(M + M_a)} + v_s^n \tag{6.43}$$

$$u_{s_x}^{n+1} = \left(\frac{1}{2} A_s C_D \rho_f \left|\vec{u}^n\right| \left(u_{f_x}^n - u_{s_x}^n\right)\right) \cdot \frac{\Delta t}{(M + M_a)} + u_{s_x}^n \tag{6.44}$$

$$u_{s_y}^{n+1} = \left(\frac{1}{2} A_s C_D \rho_f \left|\vec{u}^n\right| \left(u_{f_y}^n - u_{s_y}^n\right)\right) \cdot \frac{\Delta t}{(M + M_a)} + u_{s_y}^n \tag{6.45}$$

where,

n	=	current time step	$[-]$
$n+1$	=	next time step	$[-]$
Δt	=	time step	$[s]$

Furthermore, the absolute velocity $\vec{u}$ is obtained from equation 6.10 and the fluid velocities u_{f_x}, u_{f_y} and v_f are obtained from the simulation in OpenFOAM.

Fluctuating velocity terms caused by turbulence

Adding turbulence to the motion equations, to improve the accuracy of the dispersion modeling, is possible with the use of the Discrete Random Walk Model (DRW) as described by ANSYS, INC. (2021). In the DRW model, each eddy is characterized by a time scale, either the characteristic lifetime of an eddy (τ_e) or the particle eddy crossing time (t_{cross}), and a Gaussian distributed random fluctuating velocity in each direction, u'_x, u'_y and v'. The values of these fluctuating velocities are calculated by assuming that they obey a Gaussian probability distribution with the Root Mean Squares (RMS) given by $\sqrt{\overline{u'^2_x}}, \sqrt{\overline{u'^2_y}}, \sqrt{\overline{v'^2}}$ so that:

$$u'_x = \gamma_1 \cdot \sqrt{\overline{u'^2_x}}, \quad u'_y = \gamma_2 \cdot \sqrt{\overline{u'^2_y}}, \quad v' = \gamma_3 \cdot \sqrt{\overline{v'^2}} \tag{6.46}$$

Assuming isotropy, the local RMS values of the fluctuating velocities can be defined as:

$$\sqrt{\overline{u'^2_x}} = \sqrt{\overline{u'^2_y}} = \sqrt{\overline{v'^2}} = \sqrt{2\frac{k}{3}} \tag{6.47}$$

The variable γ_i is a Gaussian distributed random number with zero mean and unit variance. Meaning that the variance of the data set, as well as the standard deviation, will tend towards 1. Additionally, the fluctuating velocities are constant over the interval time scale. This interval time scale is defined by two different time scales, namely, the characteristic lifetime of an eddy, denoted as τ_e, and the particle eddy crossing time, t_{cross}. The duration of each interval time scale is determined by selecting the minimum value between the two different time scales.

The first interval time scale is the characteristic lifetime of an eddy, τ_e, which can either be defined as a constant:

$$\tau_e = 2T_L \tag{6.48}$$

Or it can be defined as a random variation about T_L:

$$\tau_e = -T_L \ln r \tag{6.49}$$

Where r is a uniformly distributed random number between 0 and 1 ($0 < r < 1$).

Calculating τ_e by defining it as a random variation about T_L gives a more realistic solution (ANSYS, INC., 2021), therefore, for the model, this option will be used.

The fluid Lagrangian integral time, T_L, in equations 6.48 and 6.49, describes the average time in turbulence that a fluid particle takes to travel the integral length scale. For the $k-\varepsilon$ model, it is described by the following equation:

$$T_L \approx 0.30 \frac{k}{\varepsilon} \tag{6.50}$$

The second interval time scale is the particle eddy crossing time, t_{cross}, which is described by the following equation:

$$t_{cross} = -\tau \ln \left[1 - \left(\frac{l_e}{\tau \left| u - u_p \right|} \right) \right] \tag{6.51}$$

where,

l_e	=	Eddy length scale	$[m]$
τ	=	Particle relaxation time	$[s]$
$\lvert u - u_p \rvert$	=	Magnitude of the relative velocity	$[m/s]$

The eddy length scale (l_e) is obtained from rewriting equation 6.41 and the particle relaxation time (τ) is obtained from (ANSYS, INC., 2021):

$$\tau = \frac{D^2 \rho_s}{18 \mu \rho_f} \tag{6.52}$$

Figure 6.14 shows the two different time scales calculated for each time step during the fall trajectory of a single stone. The characteristic lifetime has a much more random behavior than the eddy crossing time caused by that uniformly distributed random number used in its calculation. Furthermore, it can be observed that the eddy crossing time gradually increases with time.

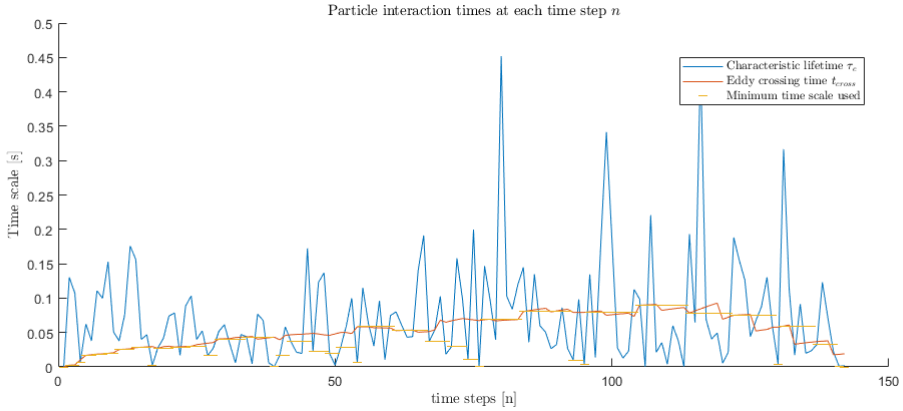

Figure 6.14: Particle interaction times at each time step

The turbulent velocity components can be added to the motion equations by means of a random fluctuation around the mean fluid velocities given by the fluid field. In all directions the fluid velocity

then becomes $u_f = \overline{u_f} + u'$. After discretizing, the final motion equations to determine the velocities of the stones in each direction are defined as follows.

$$v_s^{n+1} = \left(\frac{1}{8} A_s C_D \rho_f \left|\vec{u}^n\right| \left((v_f^n + v'^n) - v_s^n\right) + V\left(\rho_s - \rho_f\right) g\right) \cdot \frac{\Delta t}{(M + M_a)} + v_s^n \tag{6.53}$$

$$u_{s_x}^{n+1} = \left(\frac{1}{2} A_s C_D \rho_f \left|\vec{u}^n\right| \left((u_{f_x}^n + u'^n) - u_{s_x}^n\right)\right) \cdot \frac{\Delta t}{(M + M_a)} + u_{s_x}^n \tag{6.54}$$

$$u_{s_y}^{n+1} = \left(\frac{1}{2} A_s C_D \rho_f \left|\vec{u}^n\right| \left((u_{f_y}^n + u'^n) - u_{s_y}^n\right)\right) \cdot \frac{\Delta t}{(M + M_a)} + u_{s_y}^n \tag{6.55}$$

The position of a stone and its new position after each time step are described in the same way as the Single Stone Model by using a Cartesian coordinate system with coordinates in the x, y, and z directions. The positions are calculated using the following equations:

$$x_s^{n+1} = x_s^n + u_{s_x}^{n+1} \cdot \Delta t \tag{6.56}$$

$$y_s^{n+1} = y_s^n + u_{s_y}^{n+1} \cdot \Delta t \tag{6.57}$$

$$z_s^{n+1} = z_s^n + v_s^{n+1} \cdot \Delta t \tag{6.58}$$

Results

In order to demonstrate the effect of the turbulence model on the fall trajectory, the stones will be released from a single point in the middle of the jet with an exit velocity calculated by the sliding bed model from Vehmeijer (2022). Figure 6.15 shows the side view of an output from a simulation with 1000 stones overlayed on the vertical velocity components of the fluid field.

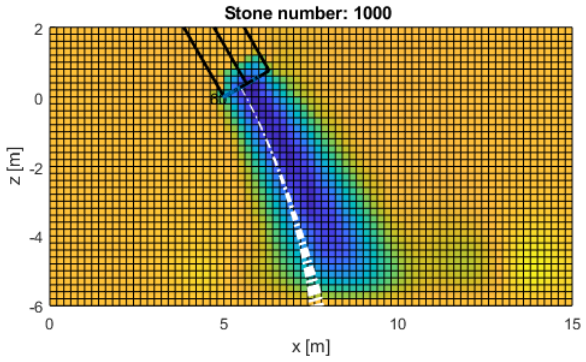

Figure 6.15: Side view dispersion $k-\varepsilon$ model

The stones have a large initial velocity and mass, causing them to reach the seabed in a relatively short amount of time. As a result, they have little time to disperse. Furthermore, the effect of gravity can be observed as the stones begin to deviate from the jet's trajectory. For a single stone group consisting of 1000 stones and a stone size of $D_{n50} = 175mm$ the initial parameters used in the simulation are given in the table below.

Table 6.5: Initial parameters

	Value	Unit
Volumetric concentration c_v	6	[%]
Fallpipe exit velocity u_{exit}	4.5	[m/s]
Bed height β_{height}	1.1	[m]
Fallpipe angle θ_{pipe}	60	[degrees]
Stone diameter D_{n50}	175	[mm]
Water depth h	6	[m]

The displacement at the seabed, denoted as Δr, is defined as the minimum horizontal distance at the seabed from the mean of the stone group to the stone in question. Therefore, the displacement at the seabed for a given stone (Δr) and the mean displacement of the stone group ($\mu_{\Delta r}$) is given by:

$$\Delta r = \sqrt{(x_s - \mu_{r_x})^2 + (y_s - \mu_{r_y})^2}, \quad \mu_{\Delta r} = \frac{1}{n}\sum_{i=1}^{n} \Delta r_i \tag{6.59}$$

where the coordinates of the stone at the seabed are given by x_s and y_s and the mean components in each direction are defined as:

$$\mu_{r_x} = \frac{1}{n}\sum_{i=1}^{n} x_{s_i}, \quad \mu_{r_y} = \frac{1}{n}\sum_{i=1}^{n} y_{s_i} \tag{6.60}$$

Figures 6.16a and 6.16b show the final result of the dispersion for this stone group as a result of the $k-\varepsilon$ model.

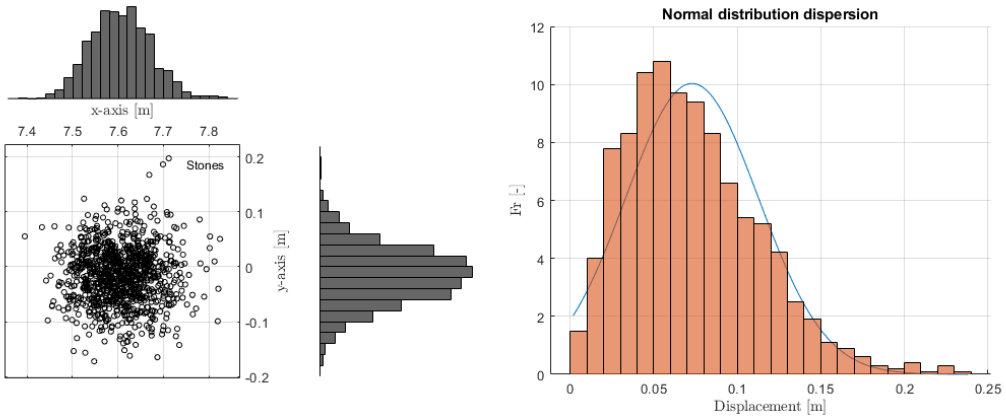

(a) Dispersion histogram

(b) Normal distribution fit on a histogram

Figure 6.16: Final distribution of the stones at the seabed at a height of $h = 6m$

It can be observed that the dispersion of the stones follows a Gaussian distribution in both directions. In the y direction, the distribution is a symmetrical normal distribution, therefore, the mean displacement in this direction is zero. However, in the x direction, the distribution is slightly left-skewed.

The left-skewed normal distribution of stones at the seabed in the x-direction can be explained as the result of the fallpipe being under an angle, causing the jet of stones to also align in that direction. The stones may then exit the jet in the downward direction, either due to gravity or turbulence, causing them to disperse further in that direction.

The effect of the skewed distribution may be more visible for smaller stones due to their lower inertia. Smaller stones are generally more influenced by external forces, such as gravity and fluid dynamics, compared to larger stones. As a result, they are more likely to deviate from the initial jet direction and disperse further away from it, leading to a broader distribution in the x-direction.

6.5. Combined model

Combining both the Single Stone Model and the $k-\varepsilon$ model will improve the quality of the stone dispersion model. Where the Single Stone Model can provide information about the dispersion caused by vortex shedding, the turbulence model can take into account the effects of the fluid motions on the stones. Merging both of the models is possible by combining the motion equations. This can be done by adding the horizontal velocity terms from the Single Stone Model to equations 6.53-6.55. After combining, the complete discretized motion equations for both models are now defined as

$$v_s^{n+1} = \left(\frac{1}{8} A_s C_D \rho_f \left|\vec{u}^n\right| \left((v_f^n + v'^n) - v_s^n\right) + V\left(\rho_s - \rho_f\right) g\right) \cdot \frac{\Delta t}{(M + M_a)} + v_s^n \tag{6.61}$$

$$u_{s_x}^{n+1} = \left(\frac{1}{2} A_s C_D \rho_f \left|\vec{u}^n\right| \left((u_{f_x}^n + u'^n) - (u_{SSM_x}^n + u_{s_x}^n)\right)\right) \cdot \frac{\Delta t}{(M + M_a)} + u_{s_x}^n \tag{6.62}$$

$$u_{s_y}^{n+1} = \left(\frac{1}{2} A_s C_D \rho_f \left|\vec{u}^n\right| \left((u_{f_y}^n + u'^n) - (u_{SSM_y}^n + u_{s_y}^n)\right)\right) \cdot \frac{\Delta t}{(M + M_a)} + u_{s_y}^n \tag{6.63}$$

The stone coordinates are then determined in the same way as previously described in equations 6.56 - 6.58.

6.5.1. Influence stone release point

The influence of both models on the dispersion can be studied using either the same initial release location or by varying the release location within the boundaries of the fallpipe exit.

Single point release

In the combined model in this subsection, each stone will have the same release point. By keeping the starting location consistent, any observed differences in dispersion can be attributed directly to the evaluated models. This way the effect that the Single Stone Model and the turbulence model have on the dispersion of a single stone can lead to a clearer understanding of the impact each model has. 1000 Stones will be used for each simulation to obtain a reliable result for the final seabed distribution. Using the same initial parameters set in table 6.2 and 6.5, the dispersion for each model is shown in Figure 6.17.

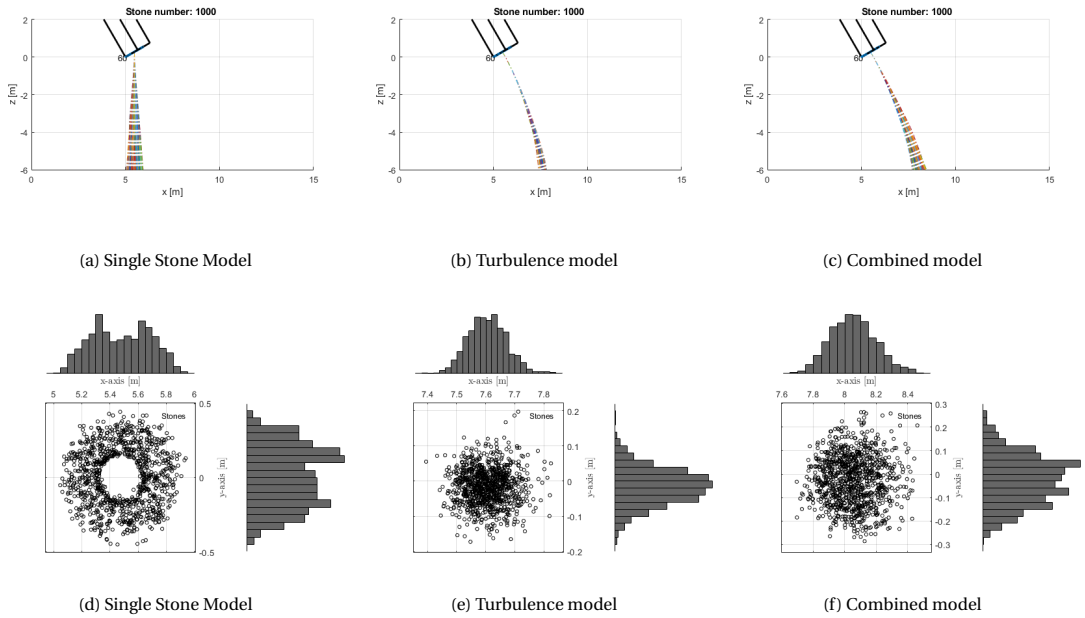

(a) Single Stone Model (b) Turbulence model (c) Combined model

(d) Single Stone Model (e) Turbulence model (f) Combined model

Figure 6.17: Combining both the model based on the Single Stone Model by Manni and Vrijling (1995) and the turbulence model

The model that uses physics based on the Single Stone Model shows a clear ring formation, characterized by a circular distribution of stones in Figure 6.17d. Upon calculating the N value that estimates the number of directional changes, given by equation 6.11, it is found to be approximately 1.1. As a result, the stones undergo a limited amount of directional changes during their fall, leading to the formation of the observed ring pattern.

When combining the Single Stone Model and the turbulence model, the ring formation is no longer visible (see Figure 6.17f). Due to the turbulence model adding additional random fluctuations in the stone velocities, it effectively counteracts the predominant directional movement from the Single Stones Model. As a result, the dispersion of stones becomes wider, indicating a broader distribution compared to each of the models alone. This can also be observed from the difference in the mean displacement (Δr), which, in the case of the turbulence model alone, amounts to approximately 7 cm. However, when using the combined model, the mean displacement increases to around 15 cm. This finding suggests that the combined model offers an improved representation of the stone dispersion by accounting for the interactions between the Single Stone Model and the turbulence effects.

Varying release point

If the stones are released from the center of the fallpipe exit, they are more likely to follow a similar path initially as they enter the central region of the jet. This can result in a different dispersion pattern compared to a uniform release. As the stones mostly interact with the core of the jet, they experience consistent turbulent forces and as a result, this leads to a narrower dispersion pattern. Therefore, in this subsection, the release point of each stone will be uniformly distributed within the boundaries of the inlet of the fallpipe. The distribution of these release points follows a uniform distribution, ensuring an equal probability for the stones to have an initial starting location across the inlet area. The distribution of release points for a random stone sample of 150 stones is shown in Figure 6.18, where each point of release is displayed as a blue dot.

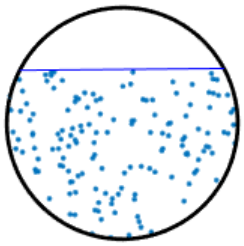

Figure 6.18: Fallpipe exit with stone release points from a random stone sample of 150 stones

A varying release location provides a more comprehensive view of the dispersion behavior as it also takes into account the potential variations in stone trajectories resulting from these different release positions. This approach captures the combined influence of both the Single Stone Model and the turbulence model on the overall dispersion patterns in the most realistic way. Again, 1000 stones will be used with the same initial parameters, set in tables 6.2 and 6.5, for each simulation, to obtain a reliable result for the final seabed distribution. The results illustrating the fall trajectory and dispersion of the stones are shown in Figures 6.19a to 6.19c.

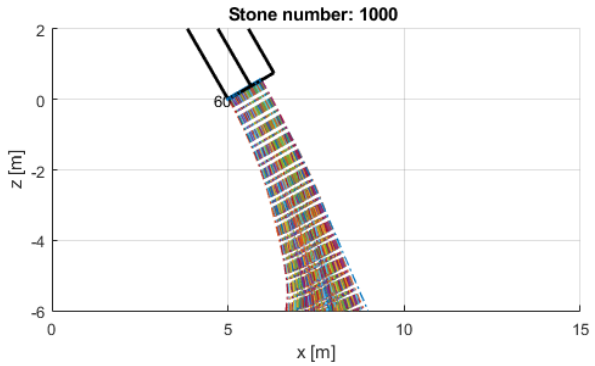

(a) Side view dispersion

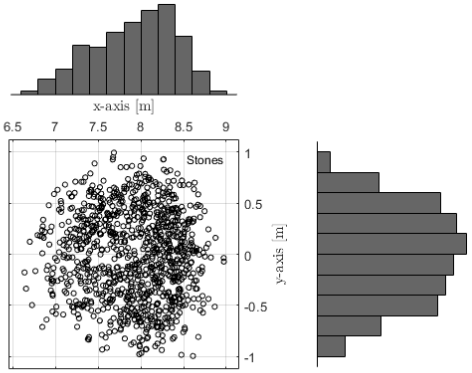

(b) Seabed distribution

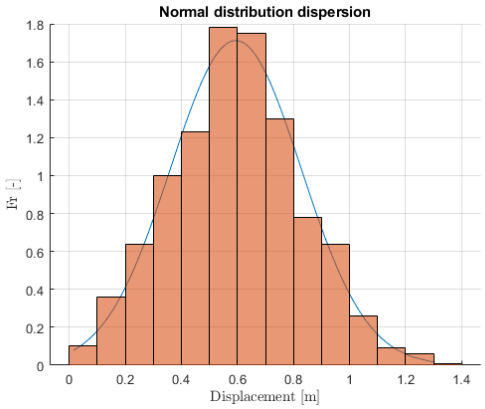

(c) Mean displacement

Figure 6.19: Results from the combined model with a varying release location of the stones.

Due to the stones being released uniformly throughout the fallpipe exit area, they have an equal chance of entering different turbulent regions of the jet. This can result in variations in the turbulent forces experienced by the stones as they interact with the turbulent flow. Due to the varying turbulence characteristics across the jet, different stones follow a much larger variety of fall trajectories. As a result, a wider distribution on the seabed is observed.

A left-skewed distribution can be observed in Figure 6.16a while studying the influence of the turbulence model on the dispersion with stones released from a single point. Same as for the single point release, the left-skewed distribution in the x direction is also observed in the combined model with a varying release location. Due to the possibility of stones having a release location closer to the bottom edges of the jet, more stones will tend to exit the jet and continue their downward motion as a result of gravity. Consequently, the left-skewed distribution observed in the combined model with varying release points, as depicted in Figure 6.19b, is even more pronounced compared to Figure 6.16a.

6.5.2. Influence varying stone diameters

During subsea stone installation, different stone sizes might be needed for different projects. Changing the diameter of the stones leads to different dispersion patterns. In general, larger stones tend to have larger inertia, which makes them less susceptible to turbulence and maintain their initial velocity longer.

As a result, larger stones will have a smaller dispersion compared to smaller stones. which have less inertia. At a constant production rate of $P = 400k/g$, water depth of $h = 6m$, fallpipe angle of $\theta_{pipe} = 60°$ and a mixture concentration of 6%, the dispersion will be compared for stone sizes with the diameters listed in table 6.6. To maintain a constant production rate, it is necessary to adjust the bed height and initial velocity corresponding to each stone size, as dictated by the Sliding Bed Model. Consequently, a different OpenFOAM simulation is required for each stone size as well. To simplify the simulations, the bed height and initial velocity have been rounded to one decimal, thereby reducing the number of different meshes required from seven to two and the number of OpenFOAM simulations from seven to five. By using this simplification, the computational time and resources necessary for the simulations can be significantly reduced while still maintaining a reasonable level of accuracy and reliability in the results. Lastly, 1000 stones will be used per sample group in Matlab to obtain a reliable result.

Table 6.6: Stone sizes and corresponding initial velocities and bed heights

Sample group	Diameter [mm]	Initial velocity [m/s]	Bed height [m]
1	50	4.2	1
2	75	4.3	1
3	100	4.4	1.1
4	140	4.5	1.1
5	175	4.5	1.1
6	210	4.5	1.1
7	245	4.6	1.1

The mean displacement, defined by equation 6.59, and the standard deviation can be seen as a measure of dispersion and spread. For each different stone sample group the mean displacement is plotted against the respective stone size in Figure 6.20a. Furthermore, the corresponding normal distributions are illustrated in Figure 6.20b.

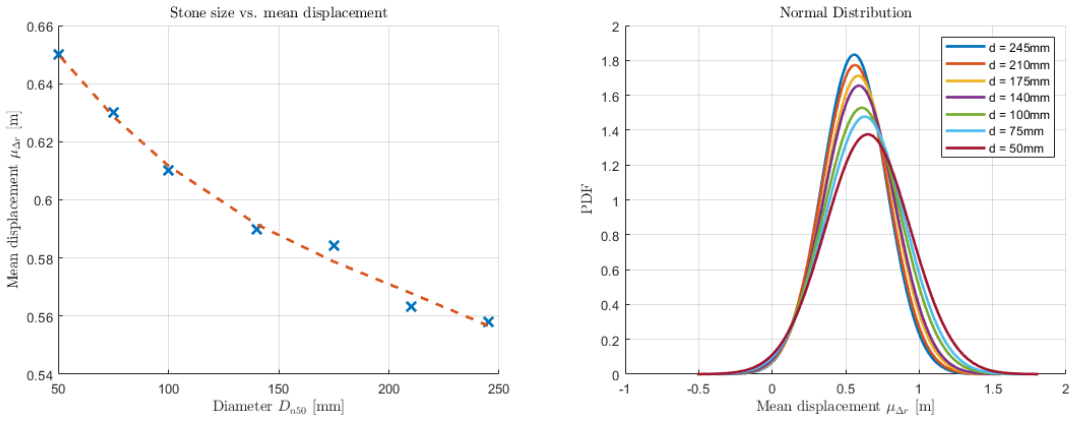

(a) Stone sizes vs mean displacement

(b) Normal distribution fit of the mean displacement

Figure 6.20: Influence of stone size on the dispersion

As expected, from figure 6.20a it can be observed that by increasing the diameter of the stone the mean displacement exponentially decreases, where the trendline is given by: $\mu_{\Delta r} = 0.487x^{-0.097}$.

Due to the greater inertia that the larger stones have, they are less affected by turbulent fluctuations in the fluid flow. As a result, they tend to maintain a more predictable trajectory and experience less dispersion. This results in a smaller mean displacement at the seabed. Secondly, the larger stones experience a much larger gravitational force, which causes them to descend much more rapidly. This causes them to have a shorter fall duration, which leads to less time available for the stones to disperse resulting in a smaller mean displacement.

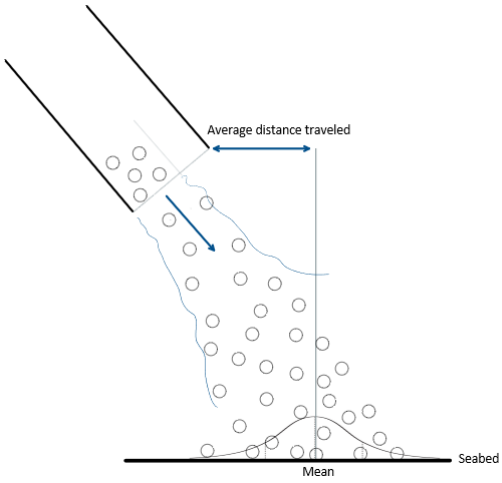

Figure 6.21: Sketch illustrating the average distance traveled

Figure 6.21 illustrates the average distance traveled, which is defined as the horizontal distance in the x direction from the tip of the fallpipe to the mean of the stone group. This distance is of importance as the safety margin during installation is also measured from the tip of the fallpipe. It is also important to note that this distance is different from the offset, which is measured from the release location of the stone. For each sample stone group, the average distance traveled is calculated and the results are shown in Figures 6.22a and 6.22b.

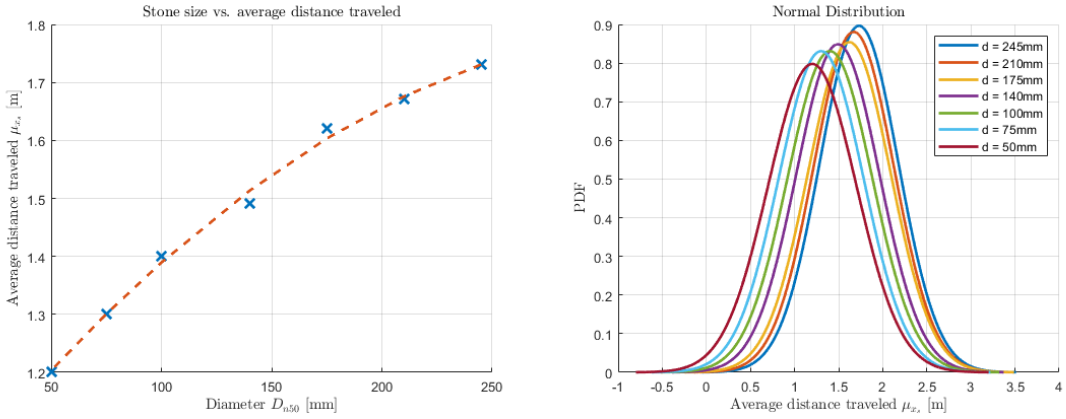

(a) Stone sizes vs average distance traveled

(b) Normal distribution fit of the average distance traveled

Figure 6.22: Influence of stone size on the distance traveled in x-direction

Based on the analysis of Figure 6.22a, it can be concluded that there is an exponential correlation between the stone diameter and the average distance traveled. The trendline shown in the figure is given by the equation $\mu_x = 2.41x^{0.235}$, where μ_x represents the average distance traveled and x represents the stone diameter. As the stone diameter increases, the average distance traveled also increases. It is worth noting that for a pipe angle of 60 degrees, there is a maximum average distance traveled. To achieve this maximum, the stones would need to experience minimal dispersion during their descent causing them to follow a nearly straight trajectory. This would require the stones to have a very high initial velocity and/or a very large inertia, allowing them to maintain a relatively linear path without any spreading.

6.5.3. Influence hindered settling

Due to the stones exiting the fallpipe in a sliding bed flow, instead of exiting one at a time. The effect of hindered settling occurs. Hindered settling, as described in chapter 4.3, causes a decrease in the terminal velocity of the stones. This can either occur due to an increase in drag coefficients caused by the presence of other stones nearby, an up-flow of water caused by the displacement of other falling stones, or by the collision of stones. Hindered settling can be added to the model using equation 4.2, effectively lowering the terminal velocity of the stones in the vertical direction. As a result, the new motion equation in the vertical direction becomes:

$$v_s^{n+1} = (1-c_v)^{n_{HS}} \cdot \left(\frac{1}{8} A_s C_D \rho_f \left| \vec{u}^n \right| \left((v_f^n + v'^n) - v_s^n \right) + V \left(\rho_s - \rho_f \right) g \right) \cdot \frac{\Delta t}{(M + M_a)} + v_s^n \tag{6.64}$$

Where c_v is the volumetric concentration of the stones in the mixture and n is the hindered settling exponent, which, for high particle Reynolds numbers, has a value of $n_{HS} = 2.4$ (Van Rhee, 2018). An important note is that, for the sake of simplicity, the assumption is made that the volume concentration of stones remains constant throughout the entire domain. The model without hindered settling is compared to the renewed model with hindered settling in Figures 6.23a and 6.23b. For the comparison, 5 simulations were run with the same initial conditions using a 50 mm diameter stone.

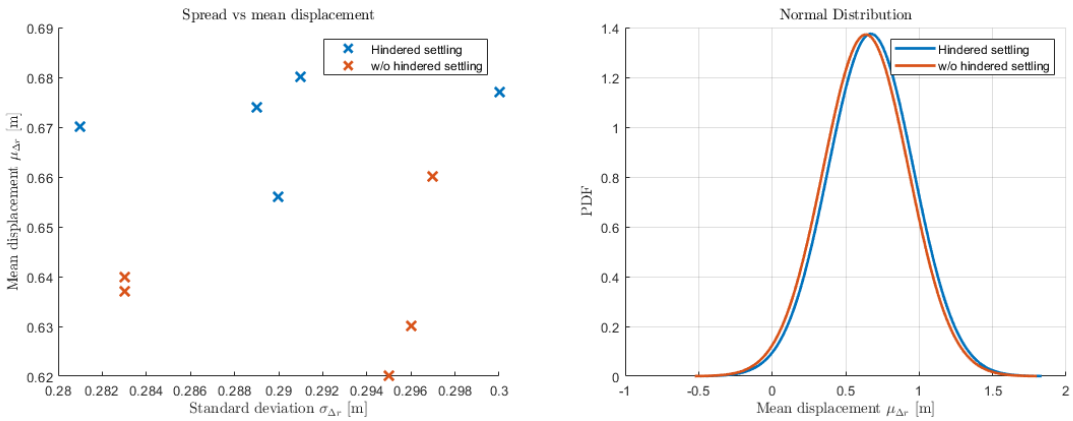

(a) Spread vs mean displacement

(b) Normal distribution fit of the mean displacement

Figure 6.23: Influence of hindered settling on the spread and mean displacement of the stones

When comparing the model with hindered settling and without hindered it is observed that mean displacement increases slightly. Due to the hindered settling lowering the fall velocity of the stones, they have more time to disperse. Consequently this results in a larger value for the mean displacement which means a wider distribution at the seabed.

6.5.4. Validation

The model can be validated by comparing the model results with the experiments performed by Vehmeijer (2022). During the experiments, the stones were loaded onto a conveyor belt which fed the stones into the fallpipe through a funnel. This fallpipe was held in place using ropes that were attached to two crossbars above the tank. The water tank used had a size of 5 by 2 by 2.5 meters and the diameter of the fallpipe used was 92 mm. A 3D model of the experimental set up used by Vehmeijer (2022) is shown in Figure 6.24.

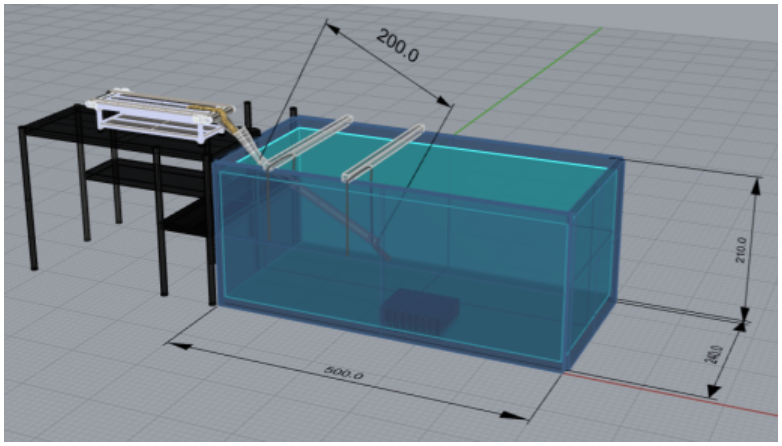

Figure 6.24: 3D model experimental set up (Vehmeijer, 2022)

During the experiments Vehmeijer (2022) used three different stone particle sizes, namely, small (5.8-10mm), medium (10-20mm) and large (20-25mm) where the nominal diameter (D_{n50}) for each different stone batch was estimated to be, respectively, 8mm, 15mm and 22 mm. However, due to the focus of the research by Vehmeijer (2022) being on the physics inside the fallpipe, a select few experimental runs can be used for validation. The parameters kept constant during the lab experiments are listed in table 6.7.

Table 6.7: Constant parameters turbulence model

	Value	Unit
Stone density ρ_s	2650	[kg/m^3]
Fluid density (water) ρ_f	1025	[kg/m^3]
Kinematic viscosity (water) μ	$1.42 \cdot 10^{-6}$	[m^2/s]
Gravitational constant g	9.81	[m/s^2]
Diameter pipe D_{pipe}	0.092	[m]

Validation using dispersion outline

This subsection describes the validation process during which the scatter of the stones during their fall is analyzed. By comparing the side view of both the experimental runs and the model of the trajectory of the stones it can be used for validation. The experimental runs that can be used for this, using the outline of the scatter stones during their fall, are run 2, 3, 4 and 17. To be able to recreate the experiments with the model the exact same settings are required. The required initial conditions for this, resulting from the lab experiments performed by Vehmeijer (2022), are listed in table 6.8.

Table 6.8: Results experiments Vehmeijer (2022)

Run	Fallpipe angle [deg]	Stone size	Production [kg/s]	Velocity [m/s]	β [rad]	β_{height} [mm]	C_{vb} [-]
2	48	Medium	0.47	0.73	1.23	30.6	0.12
3	48	Large	0.50	0.68	1.45	40.5	0.09
4	48	Small	0.46	0.65	1.14	26.8	0.16
17	60	Medium	0.43	0.84	1.5	42.7	0.07

In table 6.8, C_{vb} stands for the volumetric concentration of particles and β is the angle of the bed height (see Figure 2.4). To compare the video footage captured during the experiments with the model, the following steps were taken:

a) First, video footage was obtained from the experiments that contain a side view that clearly shows the dispersion for all stone sizes. From these videos, the relevant frames were extracted and then

superimposed, enhancing the image and resulting in a more visible dispersion pattern.

b) To identify the image that contains the most visible dispersion, the image containing the highest level of scattered stones was selected. Subsequently, an outline representing the estimated dispersion of the stones was drawn around the scattered stone positions depicted in Figure 6.25b by a black dashed line.

c) The model was then run with the exact same settings and initial conditions as the experiments. Subsequently, a side view plot was generated for each distinct experiment run that shows the dispersion well.

d) For the model, an outline representing the estimated dispersion of the stones was drawn around the shape of the trajectories of the stones as well.

e) Finally, both trajectory outlines can be compared by overlaying them onto a single image, allowing for a visual comparison of the paths followed by the stones in both the model and the experiments.

As an example, steps a to d are illustrated using the corresponding image for test run 2. Each step is shown in Figures 6.25a to 6.25d.

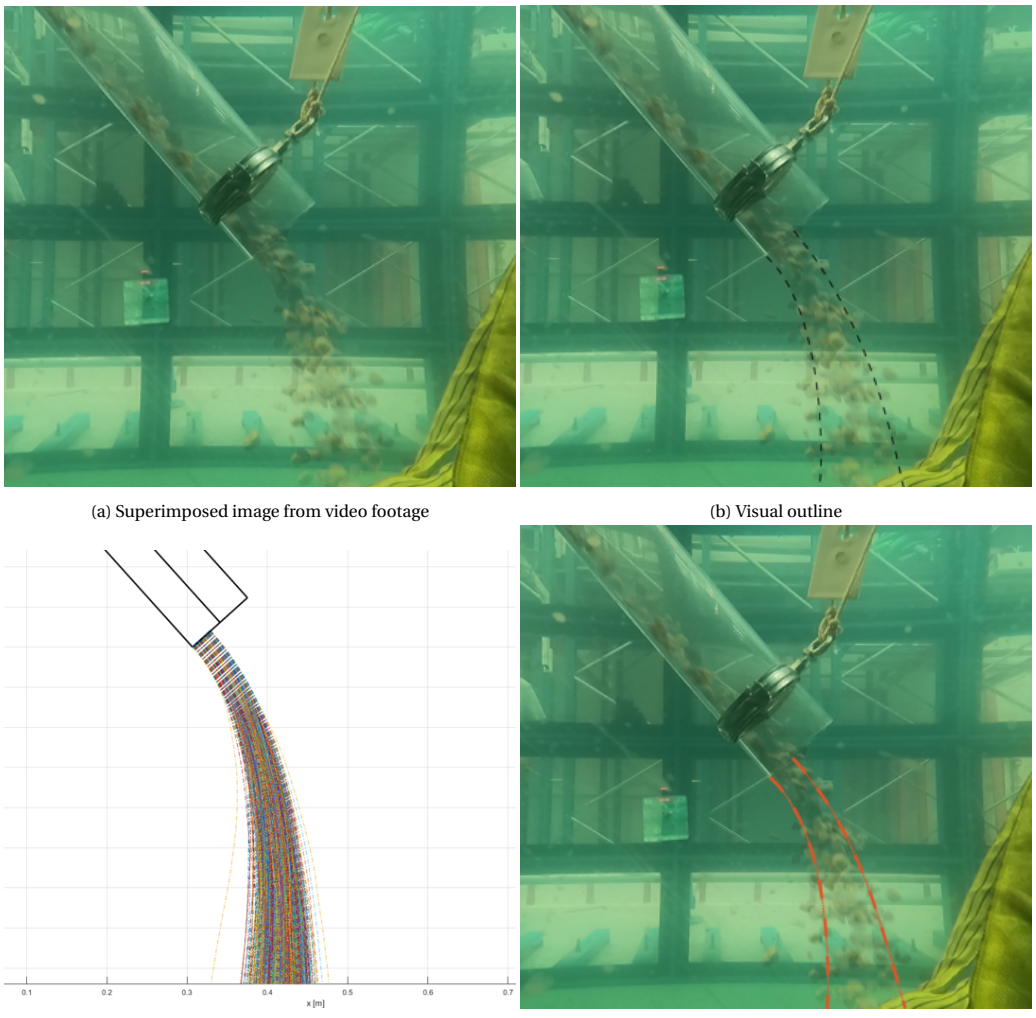

(a) Superimposed image from video footage

(b) Visual outline

(c) Model

(d) Model outline

Figure 6.25: Comparison video footage and model - run 2

The final step, which involves the comparison between the experimental runs listed in Table 6.8 and the corresponding models, is presented in Figures 6.26a to 6.26d. These figures contain the overlayed dispersion outlines, of the model and experiments, for each of the four experimental runs. The dashed black lines represent the observed stone dispersion in the experiments, while the orange dotted line represents the dispersion calculated by the model.

(a) Run 2 - Medium stones, $\theta_{pipe} = 48deg$

(b) Run 3 - Large stones, $\theta_{pipe} = 48deg$

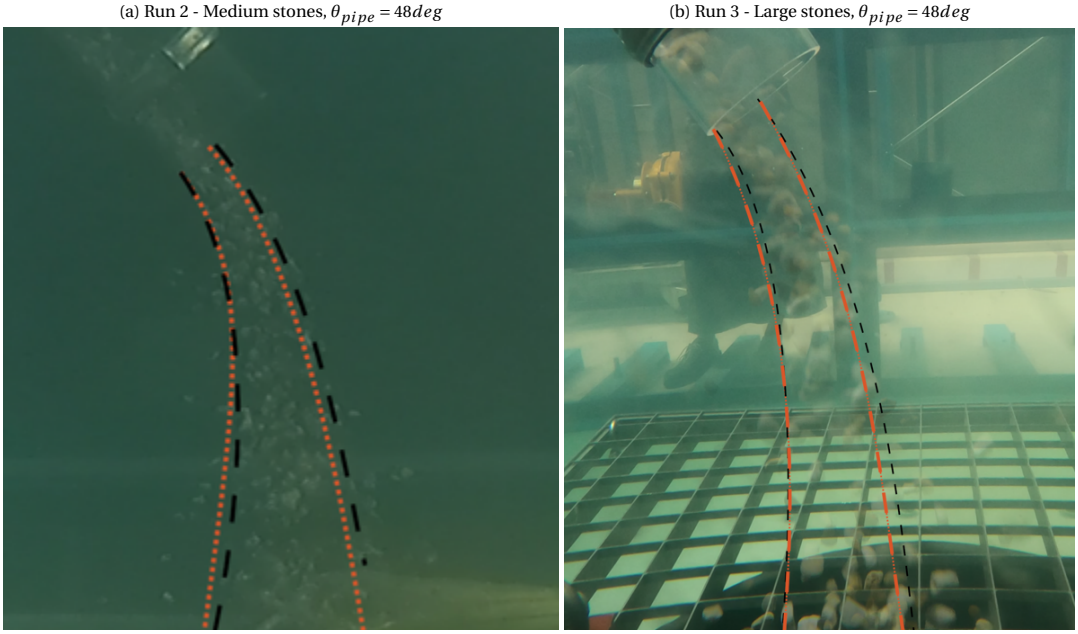

(c) Run 4 - Small stones, $\theta_{pipe} = 48deg$

(d) Run 17 - Medium stones, $\theta_{pipe} = 60deg$

Figure 6.26: Comparison video footage and model

Based on the observations from Figure 6.26, which show that the outline for the experiments and the model correspond quite well, with the main critique being the suboptimal camera angles, several conclusions can be drawn:

Model Validity: The fact that the model's outline aligns well with the experimental outline suggests that the model is very capable of capturing the essential characteristics of the dispersion of stone. Moreover, it indicates that the model's underlying assumptions and mathematical formulations are

effective in simulating the physical behavior of the system.

Reproducibility: The consistency between the outlines of both the model and the experiments implies that the dispersion patterns can be reproduced and predicted with a reasonable level of accuracy. This finding further strengthens the confidence in the model's ability to accurately simulate the real-world behavior of stone dispersion under similar conditions.

Camera Angle: The critique regarding suboptimal camera angles highlights a limitation of the experimental setup rather than a flaw in the model itself. Adjusting the camera angles in future experiments can help capture a more accurate representation of the dispersion.

Model Improvement: The correspondence between the outlines of both the model and the experiments suggests that the model is a valuable tool for analyzing stone dispersion. However, it also indicates the need for more experiments to be performed to be able to further validate the model and achieve even better alignment and accuracy between the two. Due to the experiments performed at a much smaller scale than the actual installation process, it is recommended to perform future experiments at a larger scale to avoid scaling issues.

Overall, the good agreement between the experimental and model outlines supports the validity and usefulness of the model in understanding and predicting stone dispersion. It also emphasizes the importance of carefully considering experimental setup parameters, such as camera angles, to ensure the most accurate representation of the dispersion.

Validation using measured seabed dispersion

The model can be further validated by comparing it with the dispersion patterns of the scattered stones on the seabed. These patterns were measured by Vehmeijer (2022) in runs 19 and 20. However, due to the measuring of dispersion not being the main scope of the research performed by Vehmeijer (2022), the only known initial conditions are production, fallpipe angle, stone sizes and an estimate of the water depth. Consequently, to be able to use his measurements for comparison, the other initial conditions have been calculated using his Sliding Bed Model. The initial conditions used for validation purposes in this subsection are provided in Table 6.9, with the parameters derived from the Sliding Bed Model indicated by shaded cells.

Table 6.9: Results dispersion tests Vehmeijer (2022)

Run	Fallpipe angle [deg]	Stone size	Product-ion[kg/s]	Velocity [m/s]	β [rad]	Water depth [m]	C_{vb} [-]
19	60	Medium	0.45	0.65	1.28	0.32	0.13
20	60	Medium	0.33	0.63	1.14	0.42	0.12

The dispersion during the experiments was measured using a grid system with plastic buckets positioned beneath it. The grid used consisted of 24 square cells, each with an approximate size of 6.7 cm. The observed dispersion for run 19 and 20 in the experiments performed by Vehmeijer (2022) is shown in Figures 6.27a and 6.27b.

(a) run 19 (b) run 20

Figure 6.27: Measured dispersion by Vehmeijer (2022)

From the observations, it can be concluded that the bulk of the stones are located in an area of around 20.1 cm by 13.4 cm due to each bucket having a size of 6.7cm by 6.7cm. Since the exact offset is not known, the average distance traveled cannot be compared. However, a comparison of the stone pile shapes can be made between the experimental data and the model. It is also worth noting that in run 19, the buckets were filled beyond their capacity, resulting in a greater displacement of the stones from their initial positions compared to the model prediction. The results are compared to the model by means of a histogram with the same amount of cells as the one used during the experiment. The calculated histograms are shown in Figures 6.28a and 6.28b.

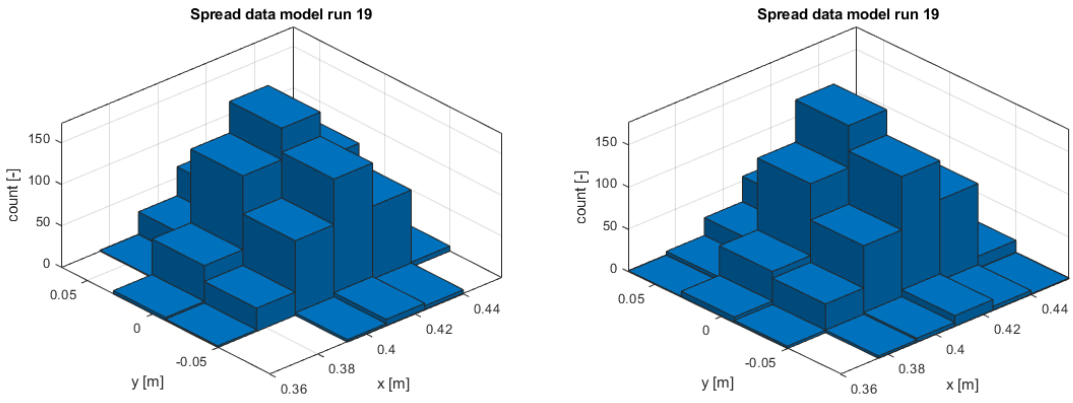

(a) run 19 (b) run 20

Figure 6.28: Histogram showing the dispersion calculated using the model

When comparing the observations from the lab experiments to the results obtained from the model, the following conclusions can be drawn:

- The dispersion in the y direction, perpendicular to the fallpipe, seems to align well with the model predictions. Both are normally distributed and have a similar spread of around 10-15cm.

- The dispersion in the x direction, parallel to the fallpipe, does not correspond as expected. This inconsistency can be the result of several different factors, namely:
  - The stones exiting the pipe form a heterogeneous mixture with areas of higher concentration and lower concentration. The variation in concentration leads to differences in the bed height and exit velocities, resulting in a larger dispersion. The dispersion in the x direction is affected more than in the y direction due to the stones having an initial velocity component in the x direction.
  - The irregular shape and varying sizes of the stones introduce significant variations in their falling trajectories, further contributing to the observed dispersion. The model assumes a constant shape and size leading to a more predictable fall trajectory, resulting in fewer stones exiting the jet and thus less dispersion.
  - The model does not consider the influence of rotating stones, which can deviate from the vertical trajectory due to the Magnus effect leading to a wider distribution.
- Some of the initial conditions for the model simulations are not known. Comparing the values calculated by the sliding bed model to previous runs with similar production rates, stone sizes, and angles reveals significantly larger values than predicted by the sliding bed model. This also has a large influence on the calculated dispersion pattern.

In conclusion, while the model successfully captures the dispersion in the y direction, more experiments are required to be able to validate or improve its accuracy in predicting the dispersion in the x direction. In addition, factors such as the heterogeneity of stone concentration or the Magnus effect could improve the model's ability to replicate observed dispersion more accurately. Lastly, obtaining more precise initial condition parameters would help in achieving better agreement between the model predictions and experimental results.

7

Application of the Model

This chapter aims to improve the understanding of stone dispersion during operation by expanding the existing model with additional factors such as a monopile as an obstacle and the presence of an ambient current. These variations in external conditions during stone installation can result in different dispersion patterns. Therefore, a comparative analysis will be conducted, examining both the fluid field and stone dispersion in scenarios with and without these additional circumstances. Two distinct cases with different stone sizes will be examined to gain deeper insights. The constant parameters used in this chapter are listed in table 7.1.

Table 7.1: Constant parameters

	Value	Unit
Stone density ρ_s	2650	[kg/m^3]
Fluid density (water) ρ_f	1025	[kg/m^3]
Kinematic viscosity (water) μ	$1.42 \cdot 10^{-6}$	[m^2/s]
Gravitational constant g	9.81	[m/s^2]
Production P	1500	[kg/s]
Water depth h	6.85	[m]
Safety Margain SM	2.5	[m]
Diameter fallpipe D_{pipe}	1.5	[m]
Diameter monopile D_{mp}	4	[m]

Furthermore, for the two distinct cases used in this section, the initial conditions are listed in table 7.2. The values in the gray cells are calculated using the Sliding Bed Model by Vehmeijer (2022).

Table 7.2: Initial parameters used in the application of the model for two cases

Case	Fallpipe angle [deg]	Stone Diameter [mm]	Velocity [m/s]	β[rad]	C_{vb}[−]
1	48	245	4.65	1.76	0.11
2	48	150	5.40	1.37	0.16

7.1. Adding a monopile

During installation, GLDD has a set safety margin for the minimum distance between the fallpipe and an obstacle, which, in this section, will be the base of a monopile. The minimum distance is measured from the tip of the fallpipe to the obstacle and is usually set to a value of 2.5 meters. Consequently, to be able to install the stones close to the monopile, the initial conditions and stone characteristics have to be chosen accordingly. Therefore, in this section, the influence of adding a monopile to the system on

the flow and the dispersion of the stones will be analyzed in two stages.

Firstly, the original geometry has to be modified by means of adding a monopile. The resulting mesh, containing the new geometry, will then be used in OpenFOAM to simulate the fluid field. The fluid field obtained from these simulations will then be compared to the simulations run without the monopile added to the geometry. During the OpenFOAM simulations, the same boundary conditions that are used for the fallpipe and the seabed are used for the monopile as well (see table 7.6).

Secondly, the fluid field data is exported to Matlab, where a boundary condition has to be set at the location of the monopile to prevent stones from traveling through the monopile wall when a collision occurs. Instead, the stones should 'bounce' off the wall. To account for the 'bounciness' of the collision a Coefficient of Restitution (CoR) is used, which is defined as the ratio of the relative velocity after the collision to the relative velocity before the collision and, therefore, has a value between 0 and 1. Consequently, a perfectly elastic collision has a CoR of 1, while a perfectly inelastic collision has a CoR of 0. Due to the dependency of the CoR on the material properties of both the stone and the monopile and the nature of the collision, a rough estimate of CoR = 0.7 is used for this model. It has to be noted that this value has been approximated based on visual observations of the resulting Matlab simulations. For a more accurate estimation, further research has to be performed.

The direction in which the stone travels after the collision is approximated by using the law of reflection, which assumes that the incident angle (Θ) is equal to the angle of reflection (Θ'). Figure 7.3 shows a schematic representation of a stone colliding with a monopile as viewed from above.

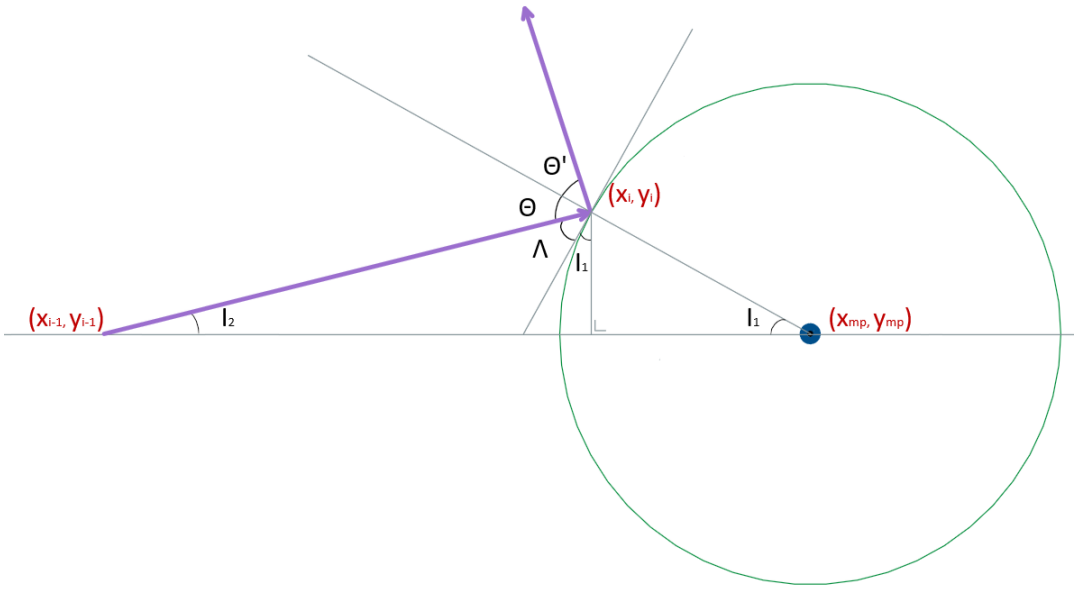

Table 7.3: Goniometric representation (Top view) of a stone (purple arrows) colliding with a monopile (green circle)

The model uses a Cartesian coordinate system, therefore the locations of the stone at the time of impact just before the collision, i and $i-1$, can be used to describe the location of the stone at time step $i+1$ just after the collision. First, the incident angle (Θ) and the angle of reflection (Θ') have to be determined. Based on Figure 7.3 it is possible to describe the angle in terms of I_1 and I_2. The derivation is shown in equations 7.1-7.3 below.

$$\Theta = 90 - \Lambda \tag{7.1}$$

$$\Lambda = 180 - I_1 - 90 - I_2 \tag{7.2}$$

$$\Theta = \Theta' = 90 - (180 - I_1 - 90 - I_2) = I_1 + I_2 \tag{7.3}$$

Both of the angles I_1 and I_2 can be described using known Cartesian coordinates, namely, the location before the impact x_{i-1} & y_{i-1}, the location at the time of impact x_i & y_i, and the location of the center of the monopile x_{mp} & y_{mp}. Consequently, both angles can be written as follows.

$$I_1 = \arctan\left(\frac{\Delta y}{\Delta x}\right) = \arctan\left(\frac{y_i - y_{mp}}{x_{mp} - x_i}\right) \tag{7.4}$$

$$I_2 = \arctan\left(\frac{\Delta y}{\Delta x}\right) = \arctan\left(\frac{y_i - y_{i-1}}{x_i - x_{i-1}}\right) \tag{7.5}$$

To describe the new location of the stone after the collision one more angle is required. This angle (I_3) is shown in Figure 7.4 and can be described using angles, I_2 and Θ.

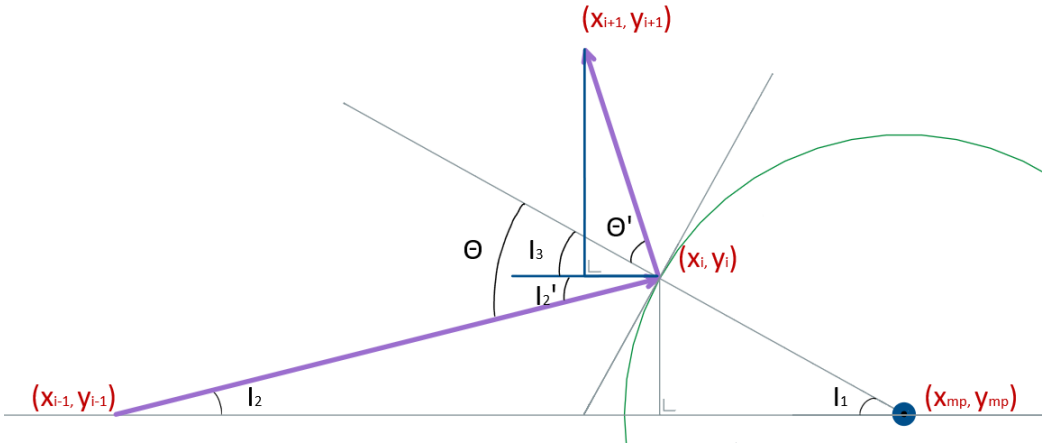

Table 7.4: Goniometric representation (Top view) of a stone (purple arrows) colliding with a monopile (green circle)

The angle I_2' shown in Figure 7.4 is equal to I_2 due to them being alternate angles that occur on opposite sides of the transversal line. Consequently, it becomes possible to describe angle I_3 in terms of I_2 and Θ.

$$I_2 = I_2' \tag{7.6}$$

$$I_3 = \Theta + \Theta' - I_2' = 2 \cdot \Theta - I_2 \tag{7.7}$$

The location after impact in the x and y direction can now be described by:

$$x_{i+1} = x_i - u_s^n \cdot \mathrm{CoR} \cdot \Delta t \cdot \cos(\Theta + I_3) \tag{7.8}$$

$$y_{i+1} = y_i + u_s^n \cdot \mathrm{CoR} \cdot \Delta t \cdot \sin(\Theta + I_3) \tag{7.9}$$

Where u_s is the absolute velocity of the stone before the collision, Δt is the time step, and CoR is the Coefficient of Restitution, which will have a value of 0.7 for this model.

The location of the stone after the collision in the z direction is easier to describe, due to the monopile's linear configuration along this axis (vertical). Illustrated in Figure 7.5, the side view depicts the collision between the stone (represented by purple arrows) and the monopile (indicated by the green line).

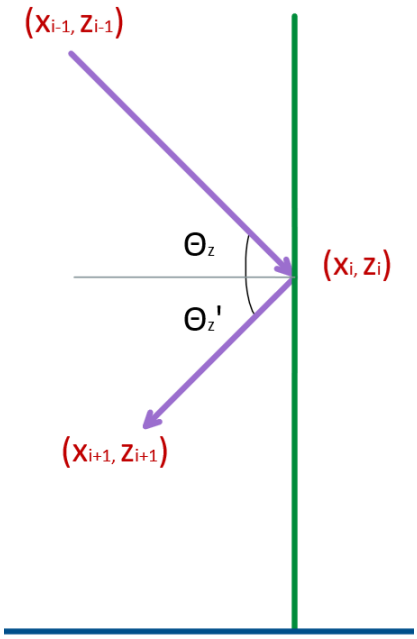

Table 7.5: Goniometric representation (side view) of a stone (purple arrows) colliding with a monopile (green line)

The z-coordinate following the collision can be described using the angle of reflection, denoted as Θ_z. The updated position z_{i+1} at time step $i+1$ can be expressed as:

$$z_{i+1} = z_i - u_s^n \cdot \text{CoR} \cdot \Delta t \cdot \cos(\Theta_z) \tag{7.10}$$

In the upcoming subsections, first, a comparative analysis between the OpenFOAM simulations with and without the monopile will be performed. Subsequently, the model will be used to analyze the dispersion results in Matlab by comparing the stone trajectories and the distribution of stones on the seabed with the model that does not include a monopile using identical initial parameters.

7.1.1. Comparative Analysis of Fluid Field in OpenFOAM Simulations

This subsection aims to analyze the influence of a monopile on the fluid field by performing multiple simulations for cases 1 and 2 using OpenFOAM. The fluid behavior in the presence and absence of the monopile will be compared by looking at the changes in flow patterns and characteristics. The results will provide valuable insights into the impact of the monopile on the fluid field.

The boundary conditions for the fluid field specified by the initial conditions in case 1 are listed in table 7.6. Due to the surfaces of the monopile being considered walls, they are assumed to have the same initial boundary conditions as the fallpipe and the seabed.

	U	alpha.sludge	epsilon	k	nut	p_rgh
Inlet	fixedValue uniform (3.11 0 −3.46)	fixedValue uniform 0.11	fixedValue uniform 0.026	fixedValue uniform 0.025	Calculated uniform 0.002	zeroGradient
Outlet	zeroGradient	inletOutlet uniform 0	zeroGradient	zeroGradient	zeroGradient	zeroGradient
Walls	fixedValue uniform (0 0 0)	zeroGradient	epsilonWallFunction uniform 0.1	kqRWallFunction uniform 0.1	nutkWallFunction uniform 0.008	fixedFluxPressure uniform 0
Atmosphere	pressureInletOutletVelocity uniform (0 0 0)	inletOutlet uniform 0	zeroGradient	zeroGradient	zeroGradient	totalPressure uniform 0

Table 7.6: Initial boundary conditions monopile modeling

It is important to note that in order to obtain the initial boundary conditions for the simulation specified by case 2, only two initial conditions that are listed in table 7.6 have to be changed. These are the initial velocity at the inlet and the initial mixture concentration at the inlet. By adjusting these values, the simulation can accurately represent the desired scenario for case 2. For the initial velocity, the updated initial value becomes, U(Inlet) = uniform(3.61 0 -4.01), and the initial mixture concentration at the inlet becomes alpha.sludge(Inlet) = uniform(0.16).

In case 1, the solution of the simulation converges to a steady state after approximately 5 seconds. Hence, the subsequent results for both the simulation using a geometry that includes a monopile and the simulation excluding a monopile are evaluated at this specific time point for comparative analysis. In case 2, the simulations reach a state steady after approximately 4 seconds, which is earlier than the steady state reached in case 1. This difference can be attributed to the higher initial exit velocity of the mixture in case 2. To determine the areas of interest for comparative analysis of the fluid field with and without a monopile, the result for a simulation with a monopile in case 1, which is illustrated using a contour filter around the mixture concentration in Figure 7.1, is analyzed.

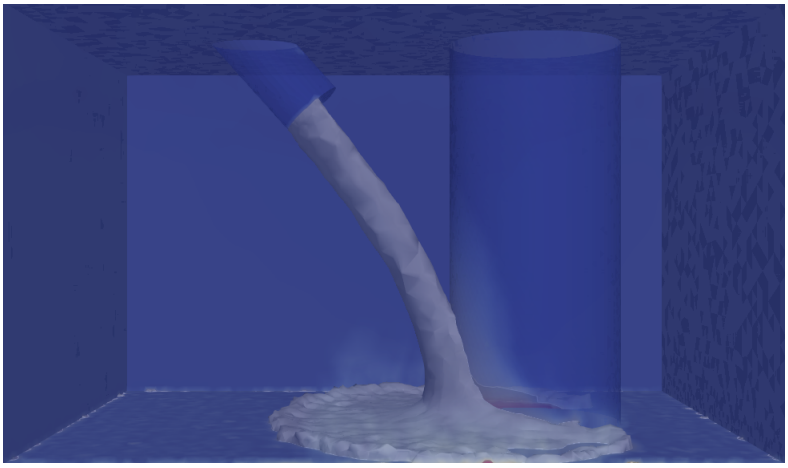

Figure 7.1: Contour of the mixture concentration for simulation 1

Figure 7.1 reveals that, for case 1, the jet formed by the mixture of stones and water impinges the monopile. From the figure, it can further be concluded that both a cross-section through the centerline of the jet in the yz-plane and a cross-section just above the seabed in the xy-plane can provide valuable insights. Figures 7.2a to 7.2d present the visualization of the absolute velocity in the yz-plane for both the simulation with and without a monopile using the initial conditions presented in case 1. Additionally, the mixture concentration is depicted in the xy-plane slightly above the seabed. The results of the simulations for case 2, including the calculated turbulent kinetic energy and the turbulent dissipation rate for both cases, can be found in Appendix C.3.1.

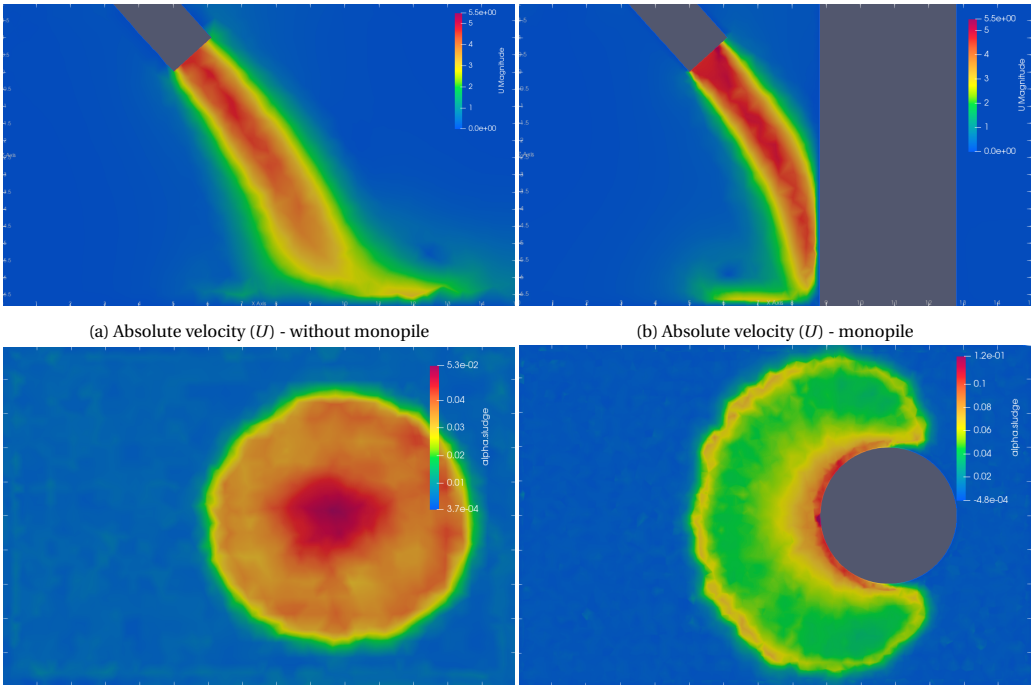

(a) Absolute velocity (U) - without monopile

(b) Absolute velocity (U) - monopile

(c) Mixture concentration ($\alpha_{mixture}$) - without monopile

(d) Mixture concentration ($\alpha_{mixture}$) - monopile

Figure 7.2: Results simulations in OpenFOAM for case 1

As a result of the jet impinging the monopile, the monopile acts as an obstacle in the fluid flow, causing the jet to deviate from its original path and redirect downwards as it interacts with the surface of the monopile. Once the jet reaches the seabed the modeled mixture disperses, spreading out laterally. Another interesting observation is that, due to the force of the impinging jet scour might occur around the base of the monopile resulting in the removal of sediment. The shape and depth of the scour hole will depend on factors such as jet velocity, angle of impingement, and sediment characteristics.

7.1.2. Comparative Analysis of the stone dispersion in Matlab

Using the results obtained from the simulation run in OpenFOAM, the fluid field data for both cases can now be used to analyze the dispersion of stones using the physics-based model in Matlab. However, due to the presence of the monopile, a boundary condition has to be set at the boundaries of the monopile to prevent stones from passing through it. When a stone hits a monopile, it loses a part of its absolute velocity due to the loss of kinetic energy. The amount of velocity that is lost on impact depends on different factors, including the properties of the stone and the monopile (such as size, shape, or density), the angle and velocity at which the stone travels on impact, and the characteristics of the fluid field. The determination of the exact energy loss on impact is beyond the scope of this study. Consequently, an assumption is made that upon impact with the monopile, approximately 80% of the stones' absolute velocity is lost, causing them to rebound from the monopile wall and continue their descent.

The combined physics-based model was applied to evaluate the stone dispersion after successfully integrating the fluid field data and the boundary condition at the monopile. For each simulation, 500 stones were used to obtain reliable results. Figure 7.3 shows the side view of the stone trajectories and Figure 7.4 illustrates the stone dispersion at the seabed resulting from the model for both case 1 and case 2. Additional simulation results can be found in Appendix D.1.1, providing a comprehensive overview of the outcomes.

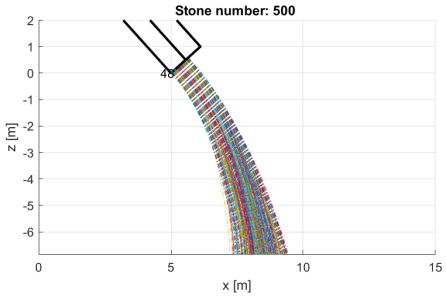

(a) Case 1

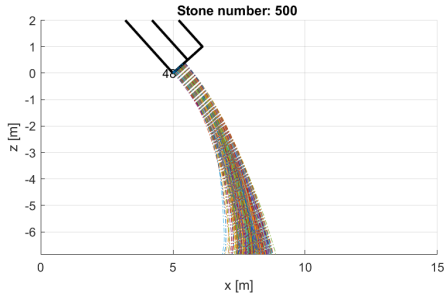

(b) Case 2

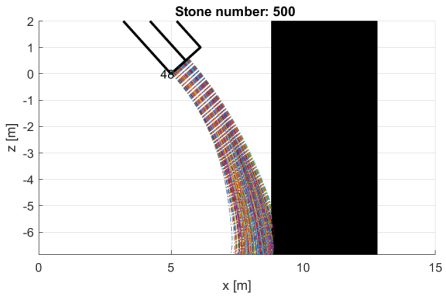

(c) Case 1 with a monopile

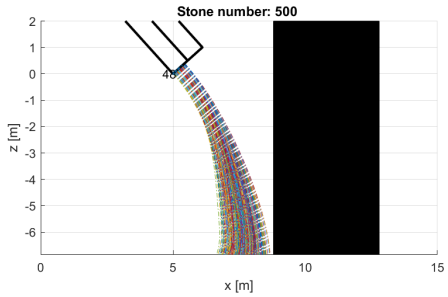

(d) Case 2 with a monopile

Figure 7.3: Side view of the dispersion calculated in Matlab

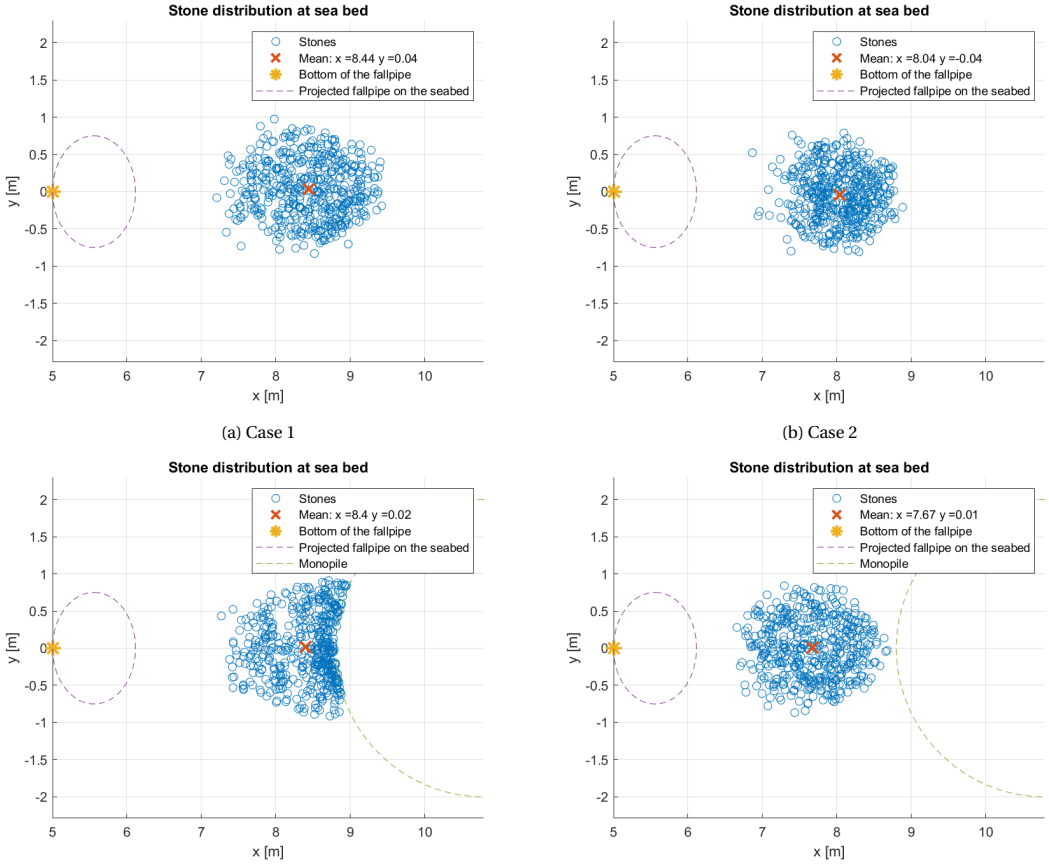

(a) Case 1

(b) Case 2

(c) Case 1 with a monopile

(d) Case 2 with a monopile

Figure 7.4: Stone distribution at seabed calculated in Matlab

Based on the analysis of Figures 7.4a to 7.4d, it can be concluded that the presence of a monopile has a significant influence on the dispersion. In case 1, where the stones collide with the monopile, they tend to settle in close proximity to the monopile, resulting in the dispersion pattern depicted in Figure 7.4c. In case 2 the stones do not directly collide with the monopile (see Figure 7.3d), however, a clear shift in the mean displacement can be observed from Figures 7.4b and 7.4d.

The presence of the monopile causes a change in the fluid flow. In case 2, this change leads to more stones exiting the jet earlier, resulting in a different dispersion pattern than the pattern observed in the simulation without a monopile.

Another explanation for the observed dispersion behavior could be the interaction between the monopile and the water flow. The presence of the monopile causes disturbances in the natural flow patterns, leading to increased turbulence and the formation of eddies nearby the monopile. These turbulent flow patterns can influence the trajectories of the stones, leading to a different dispersion pattern.

In conclusion, the addition of a monopile in the system has a significant influence on both the fluid field and the dispersion behavior of stones during installation. The presence of the monopile changes the fluid velocity and flow patterns, leading to changes in the behavior of the modeled jet and a different dispersion pattern. Consequently, the observed differences highlight the importance of considering obstacles, such as monopiles, when analyzing stone dispersion during installation. Understanding the influence of these factors will be important for accurate prediction of the dispersion during operation.

7.2. Adding an ambient current

This section aims to analyze the influence of an ambient current on the dispersion. As a result of the installation process usually taking place in open water, the presence of an ambient current becomes a significant factor that can possibly have a large impact on the dispersion of the stones. The current changes the resulting jet's shape and the falling stone's trajectory. Consequently, depending on the direction of the ambient current, the stones end up at a different location, than where they would end up if there would have been no ambient current.

For **case 1**, as listed in table 7.2, ambient currents with a different uniformly distributed velocity will be added to the simulation in OpenFOAM, considering three different directions: a cross current, a parallel current in one direction, and a parallel current in the opposite direction. The velocity of these currents will be varied from 0.1 m/s up to 0.5 m/s, which makes it possible to analyze the impact of the current on the shape of the jet. After analyzing the results, they are exported to Matlab to further analyze the influence of an ambient current on the stone dispersion.

7.2.1. Results OpenFOAM simulations

This subsection focuses on adding a uniform ambient current into the OpenFOAM simulation, considering three distinct directions: a cross current in the y direction, a parallel current in the x direction, and a parallel current in the opposite x direction. Furthermore, adding an ambient current to the simulations does not require a change in geometry, as a result, there is no need for designing a new mesh. By setting the initial field to the value of the corresponding ambient current it is possible to analyze its influence. The results of each simulation are presented at a time of $T = 5s$, representing the steady state condition.

Ambient cross current

The cross current is analyzed by applying a contour filter in paraview to visualize the mixture concentration. Due to the presence of a cross current, the jet formed by the mixture of stones and water undergoes a noticeable change in its shape, with a bending effect in the direction of the current. As a result, analyzing the results through a slice representation becomes impractical due to the changed geometry of the jet caused by the cross current. Consequently, the jet is displayed as a contour in a front view, where the ambient water has been made transparent. The obtained results for the cross current are shown in Figures 7.5a to 7.5d.

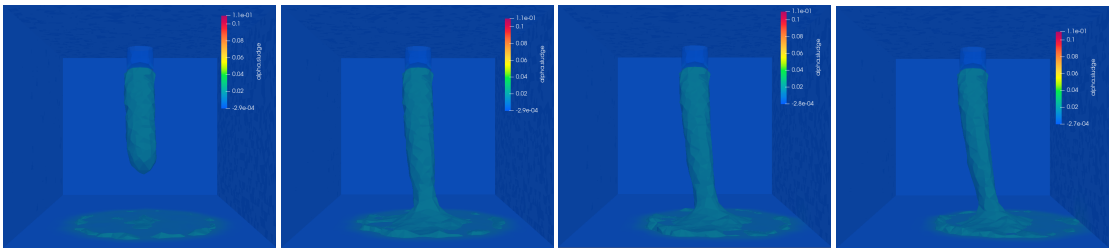

(a) $u_{current} = 0.1m/s$ (b) $u_{current} = 0.2m/s$ (c) $u_{current} = 0.35m/s$ (d) $u_{current} = 0.5m/s$

Figure 7.5: Influence of a uniform cross current on the jet

Figures 7.5a to 7.5d demonstrate that the jet is affected quite substantially by the presence of an ambient cross current causing it the bend in the direction of the current. This bending effect is more prominent in the lower part of the jet compared to the part at the fallpipe exit. This suggests that the lower portion of the jet is more susceptible to the influence of the cross current. The observed effect also suggests that the cross current might have a significant impact on the dispersion behavior of stone, potentially affecting the stone trajectories and seabed distribution.

Ambient parallel current

In contrast to the cross current, the ambient parallel current in the x direction added to the OpenFOAM simulation can be visualized using a slice representation of the fluid velocity. This is because the shape of the jet only changes in the direction of the current. The simulation results for a current varying between 0.1 m/s and 0.5 m/s in both the positive and negative x-direction are shown in Figures 7.6 and 7.7, respectively.

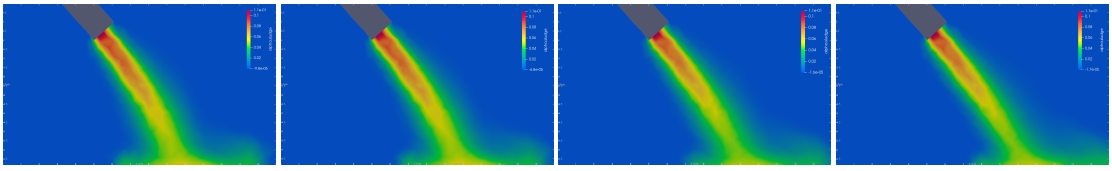

(a) $u_{current} = 0.1 m/s$ (b) $u_{current} = 0.2 m/s$ (c) $u_{current} = 0.35 m/s$ (d) $u_{current} = 0.5 m/s$

Figure 7.6: Influence of a uniform parallel current in the same x direction of the jet on the mixture ($\alpha_{mixture}$)

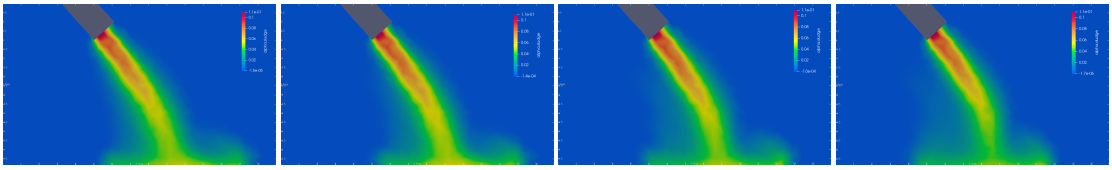

(a) $u_{current} = -0.1 m/s$ (b) $u_{current} = -0.2 m/s$ (c) $u_{current} = -0.35 m/s$ (d) $u_{current} = -0.5 m/s$

Figure 7.7: Influence of a uniform parallel current in the opposite x direction of the jet on the mixture ($\alpha_{mixture}$)

From Figure 7.6, illustrating the influence of an ambient current in the positive x direction, it can be observed that the current does not have a large effect on the shape of the jet. However, it can be noticed that the jet appears to maintain its straight form for a longer distance as the current velocity increases.

Figure 7.6 demonstrates the impact of an ambient current in the negative x direction. In this case, it can clearly be observed that the jet has a more pronounced curvature as the (absolute) velocity of the current increases.

Furthermore, it is noticed that due to the large initial velocity of the jet, the influence of the ambient current may not be significant at the start. As a result of the high initial velocity of the jet, it dominates the motion of the mixture, causing the effects of the ambient current to be relatively small or perhaps even negligible initially.

In summary, the presence of ambient currents, whether cross or parallel, can impact the dispersion and shape of the jet, with the direction and magnitude of the current playing a very important role in determining the extent of this influence.

7.2.2. Results Matlab model

In this subsection, the Matlab model will be used to analyze the influence of ambient currents on the stone dispersion, specifically focusing on the resulting final stone distribution at the seabed, encompassing both the mean and spread of the seabed distribution from different scenarios. For each of the ambient currents used in the OpenFOAM simulations from the previous subsection, the dispersion will be modeled. To obtain reliable results, each simulation is run using 500 stones. For both the cross current and the parallel current, the most relevant results are shown in this section, however, more results can be found in Appendix D.1.2 and D.1.3

Ambient cross current

As previously mentioned, the cross current will be analyzed by implementing the generated fluid fields by OpenFOAM in the Matlab model. The resulting seabed distribution will then be used to analyze the difference in mean stone displacements r, and the mean locations of the distributions in x and y-directions. For the ambient cross current, results of the final seabed distributions from the simulations run using a current velocity of 0.1 m/s up to 0.5 m/s are shown in Figures 7.8a to 7.8d.

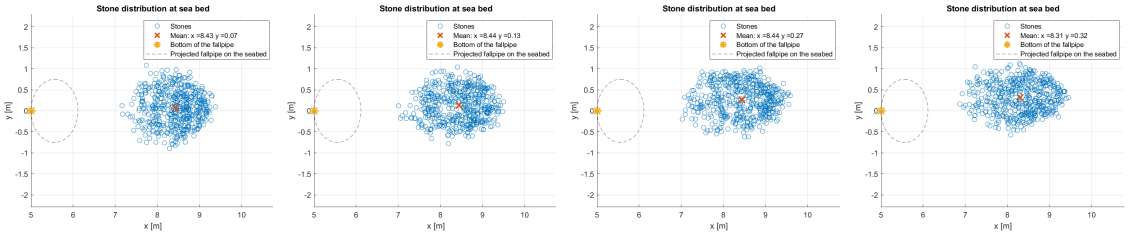

(a) $u_{current} = 0.1 m/s$ (b) $u_{current} = 0.2 m/s$ (c) $u_{current} = 0.35 m/s$ (d) $u_{current} = 0.5 m/s$

Figure 7.8: Influence of a uniform cross current perpendicular on the stone dispersion

From Figure 7.8, two observations stand out. Firstly, the mean location of the stone group increases in the y direction for an increasing ambient cross current. This can be explained as a result of the current adding an additional horizontal velocity component to the stone's motion, causing it to travel a greater distance in the y direction before reaching the seabed. Therefore, with an increasing cross current, the stones are displaced further in the y direction, resulting in an upward shift of the mean location.

Secondly, the shape of the overall spread seems to become more oval instead of round. This change in the shape of the overall spread from round to oval can be attributed to the interaction between the falling stones and the cross current. As a result of the cross current, stones facing the current tend to get pushed sideways in the direction same direction as the current, causing them to deviate from their original trajectories. Furthermore, the stones facing the current appear to be blocking the current for the stones at the other end of the jet. Consequently, the stones tend to settle closer to each other in the x direction. As the velocity of the cross current increases, more stones get pushed sideways by the current, leading to a more oval-shaped spread of the stones at the seabed.

To provide a more comprehensive analysis, the resulting mean locations in x and y-direction and the mean displacement Δr, described by equation 6.59, are plotted against the corresponding velocity of the uniform ambient cross current in Figures 7.9a to 7.9c. These figures offer a visual representation of the relationship between the cross current velocity and the resulting stone dispersion characteristics.

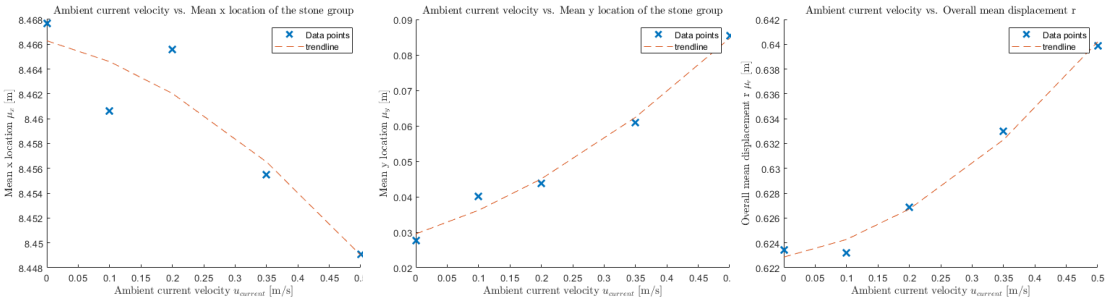

(a) Ambient current velocity vs. Mean location of the stone group in x direction

(b) Ambient current velocity vs. Mean location of the stone group in y direction

(c) Ambient current velocity vs. Overall mean displacement Δr

Figure 7.9: Influence ambient cross current on the stone dispersion

From Figures 7.9b, the increasing mean of the stone group in the y direction as the cross current velocity increases can clearly be observed. Therefore it can be concluded that, for higher cross current velocities, the stones have a large average displacement in the y direction. Secondly, it appears that the mean in the x direction also decreases slightly for larger currents. This could be explained by the effect of the cross current pushing some stones out of the jet earlier, causing them to settle closer to the fallpipe in x direction. Lastly, the overall mean displacement r, shown in Figure 7.9c, shows a clear increasing trend with higher cross current velocities. This indicates that the stones have a larger relative displacement with respect to the mean of the stone group as the velocity of the cross current increases, further supporting the observation that the cross current contributes to the stones being pushed sideways causing a wider dispersion.

In summary, the analysis of Figures 7.9a to 7.9c demonstrates the influence of cross current velocity on the mean locations in the x and y directions, as well as the overall mean displacement of the stone group. The increasing mean in the y direction and mean displacement (Δr), along with the decreasing mean in the x direction for increasing cross currents support the effect of the cross current pushing the stones sideways and thus changing their dispersion pattern.

Ambient parallel current

In this subsection, the fluid fields generated by adding an ambient current parallel to the x direction (the same direction as the x component of the fallpipe) will be used to analyze the effect on the stone dispersion. The velocities of the current used in the simulations will vary from -0.5 m/s to 0.5 m/s. The results for the final seabed distribution are shown in Figures 7.7a to 7.6d

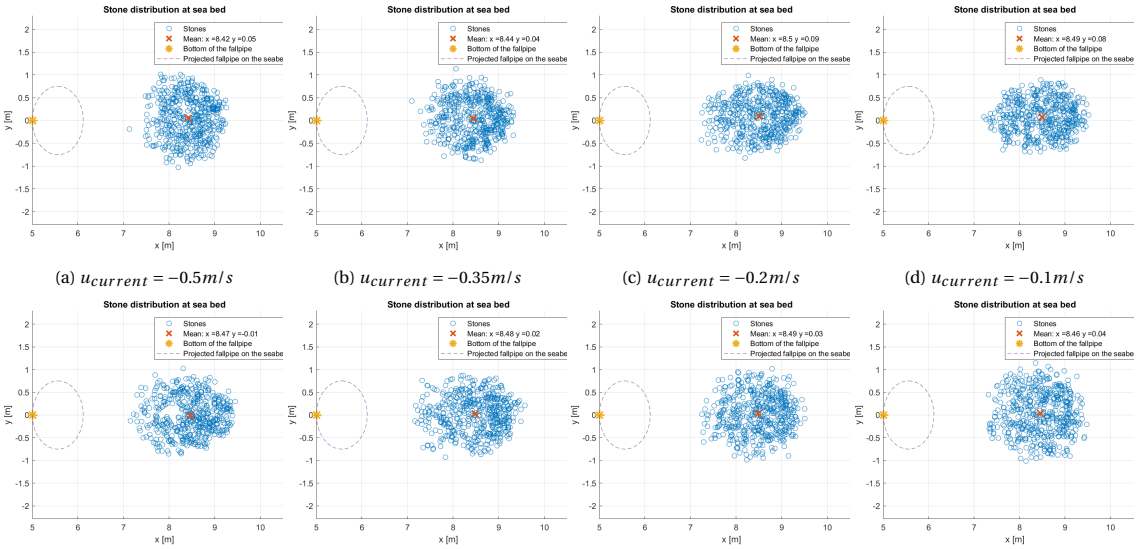

(a) $u_{current} = -0.5m/s$ (b) $u_{current} = -0.35m/s$ (c) $u_{current} = -0.2m/s$ (d) $u_{current} = -0.1m/s$

(e) $u_{current} = 0.1m/s$ (f) $u_{current} = 0.2m/s$ (g) $u_{current} = 0.35m/s$ (h) $u_{current} = 0.5m/s$

Figure 7.10: Influence of a uniform parallel current in the x direction of the jet on the stone dispersion

Figure 7.10 illustrates that an increasing current in either direction leads to a more round-shaped dispersion pattern. In the case of a positive x-direction current, the stones that would normally exit the jet at the bottom are influenced by the current, which pushes them back in the direction of the jet. Meanwhile, the stones on the opposite side are less affected by the current due to the current being blocked by the other stones. Consequently, the final seabed distribution becomes less oval-shaped as the stones that would have settled closer to the fallpipe are displaced further away, while those that would have settled far from the fallpipe experience minimal current influence and thus settle closer to their original locations in the absence of a current.

If the current acts in the negative x direction, the opposite effect is be observed. The stones that would normally exit the jet at the top are be influenced by the current, pushing them back toward the jet. On the other hand, the stones on the bottom side are less affected by the current due to blockage. As a result, the final seabed distribution still becomes less oval-shaped, but with a different orientation. The stones that would have settled closer to the fallpipe in the absence of a current now settle further away, while the stones originally far from the fallpipe experience less influence of the ambient current and thus settle closer to their original locations.

For further analysis of the dispersion, the result of the mean displacement of the stones (Δr) versus the corresponding ambient current velocities is shown in Figure 7.11.

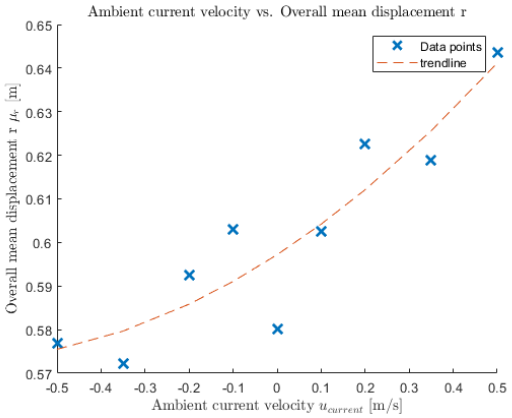

Figure 7.11: Ambient parallel current velocity vs. Overall mean displacement Δr

From Figure 7.11, it is clear that an increasing velocity of the ambient current in the positive x direction results in a larger dispersion of the stone group. This implies that when the current acts in the opposite direction (negative x direction), the stone group becomes more compact, as the average distance to the middle of the stone group is minimized. Conversely, when the current is directed in the same direction, the stones show a larger dispersion, indicating a larger spread across the seabed.

7.3. Concluding remarks

In conclusion, this chapter aimed to improve the understanding of stone dispersion during operation by expanding the existing model with additional factors such as a monopile as an obstacle and the presence of an ambient current. The comparative analysis performed in this chapter considered scenarios with and without these additional circumstances, analyzing both the fluid field and stone dispersion.

The presence of a monopile in the system was found to have a large influence on the fluid field and therefore also on the stone dispersion. The monopile acted as an obstacle in the fluid flow, causing the jet formed by the mixture of stones and water to deviate from its original path and redirect downwards as it interacted with the surface of the monopile, resulting in different dispersion patterns. The observed changes highlight the importance of considering obstacles such as monopiles when analyzing stone dispersion, as they can significantly affect the behavior of the modeled jet and the resulting dispersion pattern.

The influence of ambient currents on stone dispersion was also analyzed in this chapter. The presence of ambient currents, whether cross or parallel, was found to impact the shape of the jet and the trajectories of the falling stones. Both the cross current and the parallel current caused the jet to bend in the direction of the current leading to different dispersion patterns, where the magnitude and direction of this ambient current are very important for determining the extent of this influence. These findings demonstrate the need to consider ambient currents when studying stone dispersion, as they can lead to changes in the dispersion patterns and the final distribution of stones at the seabed.

8

Conclusions and Recommendations

The main objective of this thesis was to model the dispersion of stones while using a diagonal fallpipe for varying initial conditions, boundary conditions and additional factors, and by doing so provide valuable insights into the dispersion of stones during subsea stone installation.

8.1. Conclusions

The influence of different parameters, such as the angle of the fallpipe and bed height has revealed their significant impact on dispersion patterns. The stone characteristics have also been found to play a crucial role, where the nominal size and shape of the stones have a large impact on the dispersion. Changing the nominal diameter of the stone group results in a different initial bed height, volumetric concentration of the mixture, and initial velocity produced by the Sliding Bed Model by Vehmeijer (2022). Consequently, the fluid field generated in OpenFOAM, which uses these three variables as an initial condition, changes as well, leading to a different dispersion pattern. Overall, due to the complexity and interplay of multiple parameters, describing dispersion precisely remains challenging. However, it can be concluded that smaller stones exhibit larger dispersion due to their lower inertia compared to larger stones, where the relation between the dispersion (measured as the mean displacement $\mu_{\Delta r}$ on the seabed) and the stone size and can be described using a power law.

The influence of the lift force on the fall trajectory of a single stone can be modeled accurately based on the Single Stone Model by Manni and Vrijling (1995). For a single stone descending through stagnant water, the stones will form a normal distribution, with the mean location directed below the release location. However, there is uncertainty in the model due to the varying stone shapes and sizes, as well as the lift coefficient. The shape factor ξ used in the Single Stone Model is dependent on the direction of the flow in connection with the orientation of the stone and on the sharpness of the edges of the stone. This shape factor should be determined experimentally for each stone group as it can vary depending on the properties of the stones being analyzed. By obtaining the appropriate shape factor through experimental measurements, a more accurate representation of the stone's fall trajectory can be achieved using the model.

The presence in the fluid field has been found to affect stone dispersion, with larger stones experiencing less influence due to their greater inertia, resulting in a narrower dispersion pattern. On the other hand, smaller stones, with their lower inertia, are more prone to deviation from their original path. As these smaller stones exit the jet at the bottom, either due to gravity or turbulent forces, they start to descend according to the Single Stone Model, leading to wider dispersion patterns. This phenomenon highlights the influence of stone size and inertia on the interaction between stones and turbulence, which determines the characteristics of the dispersion observed during subsea stone installation.

Validation of the combined model using small-scale experiments has demonstrated its accuracy in representing real-world subsea scenarios in terms of stone descent. However, discrepancies were observed when comparing the dispersion at the seabed, highlighting the need for further experimental research and potential improvements to the model. Furthermore, it is worth noting that the smaller-scale simulations exhibited lower turbulence due to the lower Reynolds regime, indicating the importance of conducting experiments at larger scales to capture realistic turbulence levels.

The addition of external factors, such as nearby obstacles and ambient ocean currents, has revealed their substantial influence on stone dispersion. The presence of a monopile placed at the safety margin alters the fluid velocity and flow patterns, leading to changes in the behavior of the modeled jet and a different dispersion pattern. Ambient currents have caused shifts in the mean location and the spread of stone groups on the seabed. Cross currents have resulted in significant displacement of the mean location in the y direction, whereas parallel currents mainly influenced the shape and exit behavior of the stone jet, leading to different dispersion patterns on the seabed. For both, the cross current and the ambient current it is concluded that an increase in the velocity of the ambient current leads to a larger dispersion.

In conclusion, this research has provided valuable insights into modeling stone dispersion during subsea stone installation. The influence of initial parameters, stone characteristics, external factors, and turbulence in the fluid field has been explored. Although several research questions have been answered, further (experimental) research is required to address the observed discrepancies and improve the accuracy of the model. This work provides useful insights and lays the foundation for future studies to enhance the understanding of stone dispersion while using a diagonal fallpipe that can be used for subsea stone operations by GLDD.

8.2. Recommendations

In terms of future research, there are several recommendations to further increase the understanding and improve the model of stone dispersion during subsea stone installation:

1. Perform additional (large-scale) experiments: During the validation of the combined model, a limited amount of small-scale experiments performed by Vehmeijer (2022) were used. To further validate the combined model, more (large-scale) experiments have to be performed, where dispersion patterns observed on the seabed can be compared with the model predictions. By addressing the differences between simulations and experimental results, the accuracy of the model can be improved, leading to more reliable predictions.

2. Further explore the influence of different stone shapes on the the stone trajectories, lift force and dispersion. By analyzing multiple stone shapes and their influence on the dispersion patterns, the accuracy of the model based on the Single Stone Model by Manni and Vrijling (1995) can be improved.

3. Add more realistic field conditions such as an irregular seabed, or dynamic ambient ocean currents. By adding varying conditions, the model can by refined to account for their complexities and lead to a more realistic representation of stone dispersion during subsea installation.

4. Account for time dependency during the numerical simulations instead of using a Steady State condition. It is possible to evaluate different flow models, such as the Reynolds-Averaged Navier-Stokes (RANS) and Large Eddy Simulation (LES), to study the influence of the time dependency on the dispersion.

References

ANSYS, INC. (2021). ANSYS Fluent Theory Guide, Canonsburg.

Bouwdienst RWS. (1991). Handboek uitvoering bodemverdedigingsconstructies van losgestorte granulaire materialen. *rapport C2498*.

Chopra, G., & Mittal, S. (2019). Drag coefficient and formation length at the onset of vortex shedding. *Physics of Fluids*, *31*(1), 013601. https://doi.org/10.1063/1.5075610

Cregten, H. (1995). *Het gebruik van probabilistische methoden bij het beoordelen van het stortresultaat van een zijstorter* (Doctoral dissertation). Delft University of Technology.

CUR 169. (1995). Manual on the use of rock in hydraulic engineering. ministry of transport. *public works and water management*.

De Groot, F. (1989a). Onderzoek naar het stortresultaat van een steenstorter. *rapport WL Q673-2*.

De Groot, F. (1989b). Onderzoek naar het stortresultaat van een steenstorter. *rapport WL Q673-1*.

De Reus, J. (2004). *Het valgedrag van stortsteen onder invloed van stroming* (Master's thesis). TU Delft, Faculty of Civil Engineering and Geosciences, Hydraulic Engineering.

De Vos, T. (2004). *Het stortgedrag van een schuifstorter* (Master's thesis). TU Delft, Faculty of Civil Engineering and Geosciences, Hydraulic Engineering.

Gelderen, P. (1999). Het enkele-steen-model, een verificatie op basis van modelproeven, afstudeerverslag sectie waterbouwkunde. *Technische Universiteit Delft*.

Jones, W., & Launder, B. (1973). The prediction of laminarization with a two-equation model of turbulence, " *Intj. Heat Mass Transfer*, *5*, 301–314.

Kevelam, M. (2016). *Hydrodynamics below a closed fallpipe system: The profile of a rock berm acquired with rock placement operations* (Master's thesis). TU Delft, Faculty of Civil Engineering and Geosciences, Hydraulic Engineering.

Konter, J. (1983). Stormvloedkering oosterschelde: Stortmethoden voor drempel en overgangsconstructie. *m1768*.

Launder, B., & Sharma, B. (1974). Application of the energy-dissipation model of flow near a spinning disc. *Lett. Heat Mass Transfer*, 131–138.

Launder, B., & Spalding, D. (1974). The numerical computation of turbulent flows. *Comput. Methods Appl. Mech. Eng.*, *103*, 456–460.

Manni & Vrijling. (1995). Voorspelling van de stort bij storten met een schuifstorter [TU Delft].

Mazijk, A. (1982). Bepaling valhoogte van een steen in water vanaf het moment van loslaten tot het moment, waarop de evenwichtsvalsnelheid wordt bereikt. *Deltadienst Rijkswaterstaat*.

Meermans, W. (1997). Steenstorten, voorspelling van het stort als gestort wordt vanuit een vast punt. *Technische Universiteit Delft*.

Menter, F. R. (1994). Two-equation eddy-viscosity turbulence models for engineering applications. *AIAA journal*, *32*(8), 1598–1605.

Miedema, S. (1981). *The flow of dredged slurry in and out hoppers and the settlement process in hoppers* (Master's thesis). Master's thesis, Delft University of Technology.

OpenCFD. (2021). Openfoam: User guide v2112. the open source cfd toolbox.

Ravelli, F. (2009). *Improving the efficiency of a flexible fallpipe vessel* (Master's thesis). TU Delft, Faculty of Offshore and Dredging Engineering.

Richardson, J., & Zaki, W. (1997). Sedimentation and fluidisation: Part i. *Chemical Engineering Research and Design, 75*, S82–S100. https://doi.org/https://doi.org/10.1016/S0263-8762(97)80006-8

Slack, G. (1963). Sedimentation of compact clusters of uniform spheres. *Nature, 200*(4905), 466–467.

Sumer, B. M., Fredsøe, J., & Christiansen, N. (1992). Scour around vertical pile in waves. *Journal of Waterway, Port, Coastal, and Ocean Engineering, 118*(1), 15–31. https://doi.org/10.1061/(ASCE)0733-950X(1992)118:1(15)

van der Wal, J. (2002). *Het valgedrag van steengroepen. model onderzoek ter vergroting van het inzicht in het valgedrag van breuksteen* (Master's thesis). TU Delft, Faculty of Civil Engineering and Geosciences, Hydraulic Engineering.

Van Driest, E. R. (1956). On turbulent flow near a wall. *Journal of the aeronautical sciences, 23*(11), 1007–1011.

Van Rhee, I. C. (2018). *Lecture notes OE*44045. Technical report, TU Delft.

van Oord, G. (1996). *Spreiding van steen in het stortproces van schuifstorters. modelproeven ter verificatie van het enkel steen model* (tech. rep.). Vakgroep Waterbouwkunde, Technische Universiteit Delft and Bouwdienst Rijkswaterstaat, Utrecht.

Vehmeijer, R. (2022). *Modelling an inclined fallpipe for subsea rock placement.* (Master's thesis). TU Delft, Faculty of Offshore and Dredging Engineering.

Wilcox, D. C., et al. (1998). *Turbulence modeling for CFD* (Vol. 2). DCW industries La Canada, CA.

WL M995. (1971). Berekening snelheidsverloop vallende betonblokken [Deltares (WL)]. *rapport M995*.

Zhai, Y., & Christensen, E. D. (2022). Computational Fluid Dynamics Investigation of Flow in Scour Protection Around a Mono-Pile With the Volume-Averaged k- Model [051901]. *Journal of Offshore Mechanics and Arctic Engineering, 144*(5). https://doi.org/10.1115/1.4054393

A

Appendix: Physical background of the Single Stone Model

Below is the derivation from the single stone model given as an excerpt from 'Prediction of the deposition-mound of dumped rubble' by Prof. dr. ir. Vrijling and ir. R.J. Manni (TU Delft) and ir. D. de Wilde (Rijkswaterstaat).

When a stone is dumped in stagnant water and without initial velocity, it will, at first, be subjected to gravity and to Archimedes' Law. The vertical resulting force will be:

$$F_{\Downarrow} = \upsilon \left(\rho_s - \rho_w\right) D^3 g \tag{1}$$

in which,

$F_{\Downarrow}$ = vertical force, due to gravity, combined with the buoyancy (Archimedes' Law)

υ = factor concerning the form of the stone. (For a cube: $\upsilon = 1$, for a sphere: $\upsilon = 1/6\pi$)

ρ_s = mass density of the stone

ρ_w = mass density of the water

D = significant length-measure of the stone (diameter of a sphere, edge of a cube, etc.)

g = acceleration due to gravity.

While the stone is falling the drag force will act in the direction opposite to that of the motion:

$$F_{\Uparrow} = \xi \frac{1}{2} \rho_{\varphi} \mathrm{v}^2 D^2 C_d \tag{2}$$

in which,

$F_{\Uparrow}$ = drag force

ξ = factor like υ, but now concerning the cross section of the stone ($\xi = 1/4\pi$ for an sphere or 1 for a cube)

υ = momentary velocity of the stone

C_d = drag coefficient

A short time after the stone has been dumped in the water the velocity is (practically) constant. The forces in the direction of the motion then balance. From (1) and (2) it follows that:

$$\upsilon \left(\rho_s - \rho_w\right) D^3 g = \xi \frac{1}{2} \rho_w \upsilon^2 D^2 C_d \tag{3}$$

From (3) the velocity can be calculated:

$$\mathrm{v} = \sqrt{2\frac{\upsilon}{\xi} D\Delta \frac{g}{C_d}} \tag{4}$$

with:

$$\Delta = \frac{\rho_s - \rho_w}{\rho_w}$$

υ and ξ both depend on the form of the stone as does the drag coefficient. It is common practice to mention the drag coefficient explicitly. The other form- dependent coefficients are combined in:

$$\gamma = \sqrt{2\frac{\upsilon}{\xi}}$$

$$\gamma = \text{ constant}$$

The velocity of the stone can now be written as

$$\upsilon = \gamma \sqrt{\frac{D\Delta g}{C_d}} \tag{4a}$$

During the fall of the stone the lift force acts perpendicularly to the direction of the motion. The motion is approximately vertical so the lift force is approximately horizontal:

$$F_{\Leftarrow} = \psi \frac{1}{2} \rho_w \upsilon^2 D^2 C_L \tag{5}$$

with:

$F_{\Leftarrow}$ = lift force (perpendicular to the direction of the motion)

ψ = factor concerning the form of the stone. This factor can be split into two components, ψ' and ζ say. ψ' can be compared with ξ in equation (2), now taken for the direction of the lift force. This implies, that $1/2\psi$ can be included in the earlier mentioned constant, γ. ζ depends on the direction of the flow in connection with the orientation of the stone and on the sharpness of the edges. (For pebbles from a river, which have more or less rounded edges, ζ will have an other value than for quarry stone consisting of blasted rock.)

C_L = lift coefficient

(5) can be written as:

$$F_{\Leftarrow} = \zeta \rho_w \upsilon^2 D^2 C_L \tag{5a}$$

The mass of the body (the stone) is:

$$M = \upsilon \rho_s D^3 \tag{6}$$

with: M = mass of the body (the stone).

From the lift force (5a), the mass (6) (with υ again included in γ) and Newton's Second Law, the acceleration in the direction of the lift force can be derived:

$$a_{\Leftarrow} = \frac{\zeta \rho_w \upsilon^2 D^2 C_L}{\rho_s D^3} \tag{7}$$

in which,

$a_{\Leftarrow}$ = acceleration in the direction of the lift force

ζ = coefficient depending on the direction of the flow in connection with the orientation of the stone and on the sharpness of the edges of the stone.

When (4a) is substituted in (7), it follows that:

$$a_{\leftarrow} = \zeta \gamma^2 \frac{\rho_w}{\rho_s} \frac{C_L}{C_d} g\Delta \tag{8}$$

Suppose that the change in direction of the acceleration in the direction of the lift force is governed by vortex shedding. For 2-dimensional flow the Strouhal Number is significant for this phenomenon:

$$S = \frac{\omega D}{\nu} = \frac{2\pi}{T} \frac{D}{\nu} \tag{9}$$

in which,

S = Strouhal Number

T = period of vortex shedding, equal to the period of change of the direction of the acceleration in the direction of the lift force

ω = radian frequency: $\frac{2\pi}{T}$.

Suppose that for a 3-dimensional flow a Strouhal Number can be defined. When the fall velocity is constant (and supposing the other parameters to be constant), the Strouhal Number is constant. (9) can be written as:

$$T = \frac{2\pi D}{S\nu} \tag{10}$$

Substitution of the fall velocity (4a) in (10) leads to:

$$T = \frac{2\pi}{\gamma S \sqrt{\Delta \frac{g}{C_d}}} \sqrt{D} \tag{11}$$

Neglecting the resistance in the direction of the lift force the horizontal distance covered in the time between two changes in the direction of the "horizontal" acceleration (i.e. in the direction of the lift force) equals:

$$s_{\Leftarrow} = \frac{1}{2} a_{\Leftarrow} T^2 \tag{12}$$

Substitution of (8) and (11) in (12) leads to:

$$s_{\Leftarrow} = \frac{\gamma'}{S^2} \frac{\rho_w}{\rho_s} C_L D \tag{13}$$

with: γ' = constant

According to (3) the velocity during the fall is (approximately) constant. The vertical distance covered in the time between two changes in the direction of the "horizontal" acceleration can be approximated by:

$$s_{\Downarrow} = uT \tag{14}$$

in which:
$s \Downarrow$= vertical distance covered between two changes of the direction of the acceleration in the direction of the lift force.

When (4a) and (11) are substituted in this equation the result is:

$$s_{\Downarrow} = \frac{2\pi D}{S} \tag{15}$$

The number of changes of the direction of the "horizontal" acceleration during the fall of the stone over the water depth is approximately:

$$N \approx \frac{h}{s_{\Downarrow}} \quad \text{or:} \quad N \approx \frac{hS}{2\pi D} \tag{16}$$

in which,

N = number of changes of the direction of the "horizontal" acceleration during the fall of the stone over the water depth

h = water depth.

The distance covered in the time between two changes in the direction of the "horizontal" acceleration was (see (13)):

$$s_{\Leftarrow} = \frac{\gamma'}{S^2}\frac{\rho_w}{\rho_s}C_L D \tag{13}$$

As the stone has an irregular form and as it rotates during its fall, the vortex shedding can be taken as random over its surface. So the direction of the displacement perpendicular to the motion ("horizontal" displacement) in the next step will be independent of the displacement in the time step under consideration. This is the explanation of the random walk model, which is a statistical formulation of a diffusion process. The sum of the N independent horizontally covered distances will be zero on average.

The standard deviation of the total horizontally covered distance will be:

$$\begin{aligned}\sigma_G &= s_{\Leftarrow}\sqrt{N} \\ &= \frac{\gamma'}{S^2}\frac{\rho_w}{\rho_s}C_L D\sqrt{\frac{hS}{2\pi D}} \\ &= \frac{\gamma''}{\sqrt{S^3}}\frac{\rho_w}{\rho_s}C_L\sqrt{hD}\end{aligned} \tag{17}$$

with:

σ_G = standard deviation of the total horizontally covered distance

γ'' = constant

B

Appendix: Stone characteristics of the stone group used for validation

This Appendix contains the stone characteristics of the stones used in the verification of the Single Stone Model by Gelderen (1999). This group of stones is also used for the validation of the model based on the Single Stone Model in chapter 6.3.3.

Sortering A

steen nr.	Msteen boven water [g]	Msteen onder water [g]	Mverpl.water [g]	Vverpl.water = Vsteen [cm3]	rhos [g/cm3]	Dn [cm]	D [cm]	L [mm]	d [mm]	L/d [-]
1	5.16	3.46	1.70	1.71	3.02	1.20	1.42	23	9	2.56
2	4.04	2.71	1.33	1.34	3.02	1.10	1.31	17	11	1.55
3	3.76	2.51	1.25	1.26	2.99	1.08	1.29	16	10	1.60
4	4.79	3.22	1.57	1.58	3.03	1.16	1.39	20	9	2.22
5	3.75	2.50	1.25	1.26	2.98	1.08	1.29	19	9	2.11
6	5.15	3.45	1.70	1.71	3.01	1.20	1.42	19	11	1.73
7	3.28	2.17	1.11	1.12	2.94	1.04	1.24	16	8	2.00
8	3.23	2.16	1.07	1.08	3.00	1.03	1.22	15.5	7.5	2.07
9	4.01	2.70	1.31	1.32	3.04	1.10	1.31	19	9.5	2.00
10	4.98	3.34	1.64	1.65	3.02	1.18	1.41	19	12	1.58
11	4.11	2.70	1.41	1.42	2.90	1.12	1.34	16.5	10	1.65
12	4.40	2.95	1.45	1.46	3.01	1.13	1.35	17	10	1.70
13	3.34	2.24	1.10	1.11	3.02	1.03	1.23	19	8	2.38
14	4.12	2.70	1.42	1.43	2.88	1.13	1.34	17	11	1.55
15	4.05	2.69	1.36	1.37	2.96	1.11	1.32	19	10	1.90
16	3.52	2.37	1.15	1.16	3.04	1.05	1.25	17.5	9.5	1.84
17	4.60	3.07	1.53	1.54	2.99	1.15	1.37	18	9.5	1.89
18	2.95	1.96	0.99	1.00	2.96	1.00	1.19	16	9	1.78
19	3.74	2.50	1.24	1.25	3.00	1.08	1.28	18	9	2.00
20	3.47	2.29	1.18	1.19	2.92	1.06	1.26	17	7	2.43
21	3.54	2.36	1.18	1.19	2.98	1.06	1.26	17.5	7.5	2.33
22	3.03	2.02	1.01	1.02	2.98	1.01	1.20	17.5	9	1.94
24	3.97	2.66	1.31	1.32	3.01	1.10	1.31	16	10	1.60
25	4.57	3.06	1.51	1.52	3.01	1.15	1.37	20	10	2.00
26	4.56	3.05	1.51	1.52	3.00	1.15	1.37	18	9	2.00
27	3.84	2.57	1.27	1.28	3.00	1.09	1.29	18.5	7	2.64
28	3.28	2.18	1.10	1.11	2.96	1.03	1.23	19	8	2.38
30	5.47	3.66	1.81	1.82	3.00	1.22	1.45	20	11	1.82
32	4.13	2.75	1.38	1.39	2.97	1.12	1.33	17	9	1.89
33	4.13	2.77	1.36	1.37	3.02	1.11	1.32	19.5	8	2.44
34	4.37	2.93	1.44	1.45	3.01	1.13	1.35	18	11	1.64
35	4.35	2.86	1.49	1.50	2.90	1.14	1.36	18.5	11	1.68
36	4.18	2.82	1.36	1.37	3.05	1.11	1.32	21	8	2.63
37	5.65	3.77	1.88	1.89	2.99	1.24	1.47	20	11	1.82
40	5.56	3.71	1.85	1.86	2.99	1.23	1.46	20	10	2.00
41	4.32	2.92	1.40	1.41	3.07	1.12	1.33	21	9	2.33
42	4.76	3.14	1.62	1.63	2.92	1.18	1.40	17.5	10.5	1.67
43	5.35	3.60	1.75	1.76	3.04	1.21	1.44	17	11	1.55
44	3.09	2.06	1.03	1.04	2.98	1.01	1.20	16	8	2.00
45	5.40	3.62	1.78	1.79	3.01	1.21	1.45	18.5	9	2.06
46	4.45	2.99	1.46	1.47	3.03	1.14	1.35	18.5	10	1.85
47	4.30	2.89	1.41	1.42	3.03	1.12	1.34	19	9	2.11
48	4.06	2.73	1.33	1.34	3.03	1.10	1.31	18	9	2.00
49	4.53	3.04	1.49	1.50	3.02	1.14	1.36	16.5	9	1.83
50	4.15	2.77	1.38	1.39	2.99	1.12	1.33	16	7.5	2.13
51	3.15	2.12	1.03	1.04	3.04	1.01	1.20	15.5	8	1.94
52	3.79	2.54	1.25	1.26	3.01	1.08	1.29	17.5	7.5	2.33
53	4.71	3.13	1.58	1.59	2.96	1.17	1.39	19	10	1.90
54	3.83	2.57	1.26	1.27	3.02	1.08	1.29	19	10	1.90

I-1

steen nr.	Msteen boven water [g]	Msteen onder water [g]	Mverpl.water [g]	Vverpl.water = Vsteen [cm3]	rhos [g/cm3]	Dn [cm]	D [cm]		L [mm]	d [mm]	L/d [-]
55	4.08	2.74	1.34	1.35	3.02	1.10	1.32		17	9	1.89
56	3.75	2.45	1.30	1.31	2.87	1.09	1.30		18.5	10	1.85
57	4.97	3.27	1.70	1.71	2.90	1.20	1.42		19.5	12	1.63
58	4.06	2.71	1.35	1.36	2.99	1.11	1.32		18.5	10	1.85
59	3.31	2.21	1.10	1.11	2.99	1.03	1.23		19	7	2.71
60	5.04	3.37	1.67	1.68	3.00	1.19	1.42		22	12	1.83
61	3.48	2.33	1.15	1.16	3.01	1.05	1.25		18	10	1.80
62	4.22	2.81	1.41	1.42	2.97	1.12	1.34		15	11	1.36
63	4.15	2.74	1.41	1.42	2.92	1.12	1.34		19.5	7	2.79
64	4.35	2.91	1.44	1.45	3.00	1.13	1.35		20	10	2.00
65	3.84	2.58	1.26	1.27	3.03	1.08	1.29		17	11	1.55
67	3.90	2.62	1.28	1.29	3.03	1.09	1.30		17	9	1.89
68	3.85	2.55	1.30	1.31	2.94	1.09	1.30		18	10	1.80
69	4.83	3.23	1.60	1.61	3.00	1.17	1.40		20	8	2.50
70	4.67	3.09	1.58	1.59	2.94	1.17	1.39		19.5	9.5	2.05
71	3.42	2.26	1.16	1.17	2.93	1.05	1.25		16.5	10.5	1.57
72	4.30	2.84	1.46	1.47	2.93	1.14	1.35		16	10	1.60
73	3.73	2.49	1.24	1.25	2.99	1.08	1.28		17.5	10	1.75
74	3.54	2.37	1.17	1.18	3.01	1.06	1.26		16.5	6.5	2.54
75	4.89	3.28	1.61	1.62	3.02	1.17	1.40		17	10	1.70
76	5.05	3.41	1.64	1.65	3.06	1.18	1.41		20	10	2.00
77	3.84	2.55	1.29	1.30	2.96	1.09	1.30		18	10	1.80
78	3.72	2.49	1.23	1.24	3.00	1.07	1.28		19	9	2.11
79	3.19	2.12	1.07	1.08	2.96	1.03	1.22		18.5	7	2.64
80	3.31	2.22	1.09	1.10	3.02	1.03	1.23		16.5	8	2.06
81	5.43	3.55	1.88	1.89	2.87	1.24	1.47		21	10	2.10
82	5.29	3.45	1.84	1.85	2.86	1.23	1.46		20.5	10	2.05
84	3.87	2.60	1.27	1.28	3.03	1.09	1.29		20.5	9	2.28
85	5.56	3.74	1.82	1.83	3.04	1.22	1.46		20.5	10	2.05
86	4.22	2.74	1.48	1.49	2.83	1.14	1.36		17	11.5	1.48
87	5.64	3.79	1.85	1.86	3.03	1.23	1.46		22	10.5	2.10
88	4.60	3.09	1.51	1.52	3.03	1.15	1.37		21	10	2.10
89	4.43	2.96	1.47	1.48	2.99	1.14	1.36		19	9	2.11
90	4.04	2.70	1.34	1.35	3.00	1.10	1.32		16	11	1.45
91	5.04	3.38	1.66	1.67	3.02	1.19	1.41		18	10	1.80
92	5.77	3.86	1.91	1.92	3.00	1.24	1.48		22	13	1.69
93	4.17	2.80	1.37	1.38	3.02	1.11	1.33		20	7.5	2.67
94	5.35	3.65	1.70	1.71	3.13	1.20	1.42		18	10	1.80
95	5.26	3.50	1.76	1.77	2.97	1.21	1.44		18.5	10	1.85
96	5.55	3.72	1.83	1.84	3.01	1.23	1.46		22	10	2.20
97	5.11	3.33	1.78	1.79	2.85	1.21	1.45		20.5	8.5	2.41
98	5.34	3.59	1.75	1.76	3.03	1.21	1.44		20	13	1.54
99	4.39	2.94	1.45	1.46	3.01	1.13	1.35		22	8	2.75
101	4.63	3.09	1.54	1.55	2.99	1.16	1.38		21	8.5	2.47
103	4.25	2.84	1.41	1.42	2.99	1.12	1.34		19	8.5	2.24
104	4.57	3.08	1.49	1.50	3.05	1.14	1.36		22.5	7.5	3.00
105	4.26	2.86	1.40	1.41	3.02	1.12	1.33		20	9	2.22
106	4.48	2.99	1.49	1.50	2.99	1.14	1.36		16	11	1.45
107	3.73	2.49	1.24	1.25	2.99	1.08	1.28		18	9.5	1.89
108	4.61	3.06	1.55	1.56	2.95	1.16	1.38		17	10.5	1.62
109	5.41	3.63	1.78	1.79	3.02	1.21	1.45		24	9.5	2.53
110	4.12	2.74	1.38	1.39	2.97	1.12	1.33		19	8.5	2.24
111	4.14	2.76	1.38	1.39	2.98	1.12	1.33		18	9	2.00

I-2

steen nr.	Msteen boven water [g]	Msteen onder water [g]	Mverpl.water [g]	Vverpl.water = Vsteen [cm3]	rhos [g/cm3]	Dn [cm]	D [cm]		L [mm]	d [mm]	L/d [-]
112	4.92	3.30	1.62	1.63	3.02	1.18	1.40		18	10	1.80
113	4.93	3.30	1.63	1.64	3.00	1.18	1.40		20	9	2.22
114	4.30	2.86	1.44	1.45	2.97	1.13	1.35		19	11	1.73
116	4.62	3.11	1.51	1.52	3.04	1.15	1.37		18	10.5	1.71
117	3.82	2.53	1.29	1.30	2.94	1.09	1.30		16	9	1.78
120	3.86	2.59	1.27	1.28	3.02	1.09	1.29		17	11	1.55
121	4.39	2.93	1.46	1.47	2.99	1.14	1.35		18	9	2.00
122	4.30	2.87	1.43	1.44	2.99	1.13	1.34		17.5	8.5	2.06
123	3.85	2.59	1.26	1.27	3.04	1.08	1.29		19	11	1.73
124	3.28	2.16	1.12	1.13	2.91	1.04	1.24		17	7.5	2.27
125	3.77	2.50	1.27	1.28	2.95	1.09	1.29		16	9	1.78
126	4.15	2.78	1.37	1.38	3.01	1.11	1.33		18	9	2.00
127	3.70	2.46	1.24	1.25	2.96	1.08	1.28		17	9.5	1.79
128	4.08	2.69	1.39	1.40	2.92	1.12	1.33		17	7	2.43
129	5.31	3.56	1.75	1.76	3.01	1.21	1.44		20	12	1.67
132	4.57	3.05	1.52	1.53	2.99	1.15	1.37		20	9.5	2.11
133	3.98	2.68	1.30	1.31	3.04	1.09	1.30		18	11	1.64
134	4.57	3.03	1.54	1.55	2.95	1.16	1.38		19	10	1.90
135	4.27	2.87	1.40	1.41	3.03	1.12	1.33		18	9	2.00
136	4.52	3.00	1.52	1.53	2.95	1.15	1.37		19	10	1.90
138	4.74	3.20	1.54	1.55	3.06	1.16	1.38		20	11	1.82
139	4.01	2.68	1.33	1.34	3.00	1.10	1.31		19	7	2.71
140	3.37	2.25	1.12	1.13	2.99	1.04	1.24		15.5	8	1.94
141	4.08	2.70	1.38	1.39	2.94	1.12	1.33		18	12	1.50
142	5.47	3.62	1.85	1.86	2.94	1.23	1.46		21	11	1.91
143	3.68	2.46	1.22	1.23	3.00	1.07	1.27		19	11	1.73
144	4.22	2.80	1.42	1.43	2.95	1.13	1.34		19	9.5	2.00
145	4.40	2.97	1.43	1.44	3.06	1.13	1.34		18	10	1.80
146	3.26	2.19	1.07	1.08	3.03	1.03	1.22		16	9	1.78
147	4.02	2.69	1.33	1.34	3.00	1.10	1.31		17	8	2.13
148	5.52	3.68	1.84	1.85	2.98	1.23	1.46		21.5	11	1.95
149	5.80	3.88	1.92	1.93	3.00	1.25	1.48		19	11	1.73
150	4.32	2.90	1.42	1.43	3.02	1.13	1.34		20	8	2.50
151	5.07	3.39	1.68	1.69	3.00	1.19	1.42		17.5	13	1.35
153	4.27	2.85	1.42	1.43	2.99	1.13	1.34		18	8	2.25
154	3.91	2.61	1.30	1.31	2.99	1.09	1.30		17.5	7.5	2.33
155	4.81	3.21	1.60	1.61	2.99	1.17	1.40		18.5	11	1.68
156	4.89	3.28	1.61	1.62	3.02	1.17	1.40		16.5	12	1.38
157	3.31	2.19	1.12	1.13	2.94	1.04	1.24		17.5	6.5	2.69
158	5.12	3.43	1.69	1.70	3.01	1.19	1.42		18.5	10.5	1.76
159	3.73	2.49	1.24	1.25	2.99	1.08	1.28		16	11	1.45
160	3.90	2.61	1.29	1.30	3.00	1.09	1.30		18	10.5	1.71
161	5.52	3.65	1.87	1.88	2.93	1.23	1.47		16.5	11	1.50
162	4.88	3.25	1.63	1.64	2.97	1.18	1.40		19	11	1.73
163	5.16	3.44	1.72	1.73	2.98	1.20	1.43		20	11	1.82
164	5.39	3.60	1.79	1.80	2.99	1.22	1.45		19	11	1.73
165	5.43	3.64	1.79	1.80	3.01	1.22	1.45		17	12	1.42
166	4.66	3.10	1.56	1.57	2.97	1.16	1.38		18	10	1.80
167	5.25	3.52	1.73	1.74	3.01	1.20	1.43		17.5	11.5	1.52
168	5.11	3.40	1.71	1.72	2.97	1.20	1.43		18.5	10	1.85
169	5.18	3.46	1.72	1.73	2.99	1.20	1.43		22	10	2.20
170	5.15	3.42	1.73	1.74	2.96	1.20	1.43		18	10	1.80
171	4.49	2.99	1.50	1.51	2.97	1.15	1.37		19	11	1.73

I-3

steen nr.	Msteen boven water [g]	Msteen onder water [g]	Mverpl.water [g]	Vverpl.water = Vsteen [cm3]	rhos [g/cm3]	Dn [cm]	D [cm]	L [mm]	d [mm]	L/d [-]
172	3.88	2.60	1.28	1.29	3.01	1.09	1.30	18	9	2.00
173	4.72	3.12	1.60	1.61	2.93	1.17	1.40	21.5	9.5	2.26
174	4.72	3.15	1.57	1.58	2.99	1.16	1.39	20.5	8	2.56
176	4.26	2.86	1.40	1.41	3.02	1.12	1.33	18	8	2.25
177	3.76	2.47	1.29	1.30	2.90	1.09	1.30	16	10.5	1.52
178	4.11	2.76	1.35	1.36	3.02	1.11	1.32	16	11	1.45
179	3.53	2.35	1.18	1.19	2.97	1.06	1.26	17.5	10	1.75
180	3.04	2.04	1.00	1.01	3.02	1.00	1.19	17	8	2.13
181	3.33	2.22	1.11	1.12	2.98	1.04	1.24	17.5	9	1.94
182	3.96	2.66	1.30	1.31	3.03	1.09	1.30	17	9	1.89
183	3.68	2.47	1.21	1.22	3.02	1.07	1.27	17	8.5	2.00
184	4.80	3.23	1.57	1.58	3.04	1.16	1.39	21	9	2.33
185	3.65	2.41	1.24	1.25	2.92	1.08	1.28	16	9	1.78
186	3.17	2.08	1.09	1.10	2.89	1.03	1.23	16.5	7.5	2.20
187	4.42	2.92	1.50	1.51	2.93	1.15	1.37	18	10	1.80
188	4.85	3.25	1.60	1.61	3.01	1.17	1.40	19.5	10.5	1.86
189	3.57	2.38	1.19	1.20	2.98	1.06	1.26	19	10	1.90
190	4.13	2.69	1.44	1.45	2.85	1.13	1.35	19	9.5	2.00
191	4.76	3.18	1.58	1.59	2.99	1.17	1.39	18.5	9	2.06
192	4.19	2.82	1.37	1.38	3.04	1.11	1.33	18	10	1.80
193	3.95	2.62	1.33	1.34	2.95	1.10	1.31	21.5	7	3.07
194	4.07	2.65	1.42	1.43	2.85	1.13	1.34	17	10	1.70
195	3.75	2.52	1.23	1.24	3.03	1.07	1.28	18	9.5	1.89
196	3.89	2.59	1.30	1.31	2.97	1.09	1.30	18.5	10	1.85
197	3.62	2.43	1.19	1.20	3.02	1.06	1.26	17	7	2.43
199	3.74	2.52	1.22	1.23	3.05	1.07	1.27	20	8	2.50
200	3.77	2.56	1.21	1.22	3.10	1.07	1.27	15.5	10	1.55
201	4.26	2.80	1.46	1.47	2.90	1.14	1.35	18	7.5	2.40
202	4.14	2.79	1.35	1.36	3.05	1.11	1.32	19	8	2.38
203	4.42	2.98	1.44	1.45	3.05	1.13	1.35	17	8	2.13
204	3.91	2.62	1.29	1.30	3.01	1.09	1.30	18	9	2.00
205	4.00	2.69	1.31	1.32	3.03	1.10	1.31	17	10	1.70
206	4.70	3.14	1.56	1.57	2.99	1.16	1.38	19	11	1.73
207	3.83	2.52	1.31	1.32	2.90	1.10	1.31	16	9	1.78
208	3.72	2.45	1.27	1.28	2.91	1.09	1.29	18	8	2.25
209	4.22	2.87	1.35	1.36	3.11	1.11	1.32	17	7	2.43
210	4.02	2.70	1.32	1.33	3.03	1.10	1.31	19.5	7	2.79
211	3.87	2.57	1.30	1.31	2.96	1.09	1.30	19	9.5	2.00
212	3.41	2.27	1.14	1.15	2.97	1.05	1.25	18	8	2.25
213	3.64	2.44	1.20	1.21	3.01	1.06	1.27	18	9	2.00
215	3.20	2.14	1.06	1.07	3.00	1.02	1.22	15	10	1.50
216	4.68	3.15	1.53	1.54	3.04	1.15	1.37	19	9	2.11
217	4.09	2.75	1.34	1.35	3.03	1.10	1.32	18	9.5	1.89
218	4.60	3.10	1.50	1.51	3.05	1.15	1.37	19	8.5	2.24
220	3.93	2.61	1.32	1.33	2.96	1.10	1.31	19	8.5	2.24

C

Appendix: OpenFOAM

This appendix contains the case structure used during the OpenFOAM simulations alongside the resulting simulation outcomes.

C.1. Case structure

Figure C.1 illustrates a tree diagram of the case structure used in OpenFOAM.

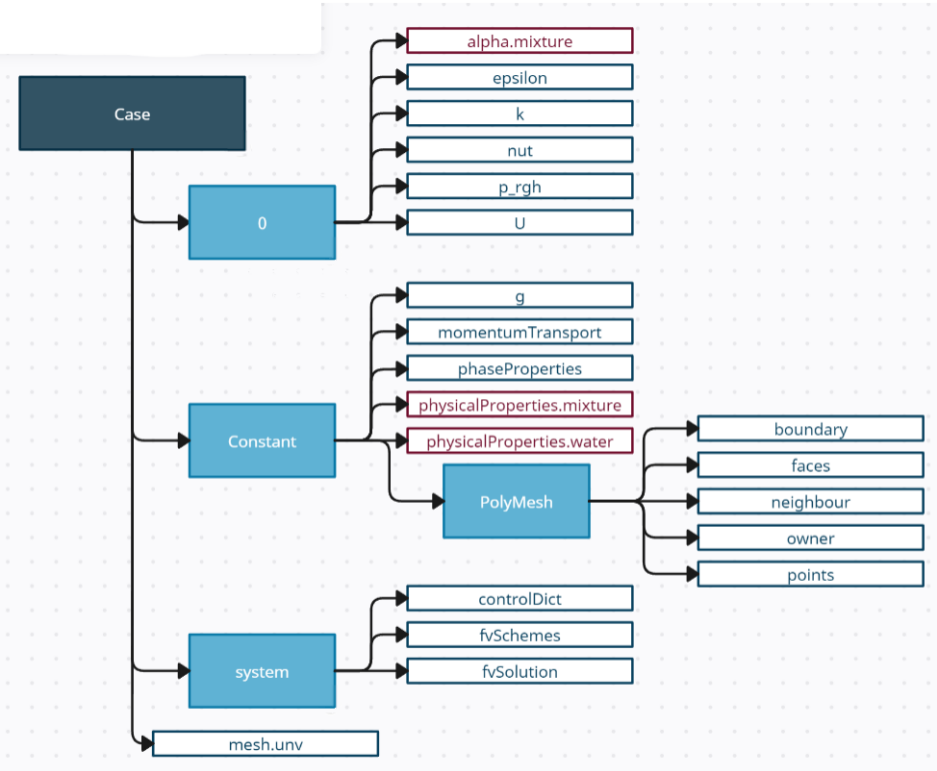

Figure C.1: Tree diagram displaying the OpenFOAM case structure

C.1.1. Directories

Within the case file, there are several directories: '0', 'Constant', 'PolyMesh', and 'system'. The usecase of each directory will briefly be described below.

- **0**: The '0' directory contains the initial and boundary conditions for each variable used in the model. In this case the variables used are the concentration (alpha.mixture), turbulent dissipation rate (epsilon), turbulent kinetic energy (k), turbulent viscosity (nut), dynamic pressure (prgh) and the velocity (U).
- **Constant**: This directory contains information about the physical properties and the mesh. In this case, the mesh was created using the file 'mesh.unv' to create the PolyMesh directory containing information about the mesh.
- **System** The 'system' directory is used to store various configuration files and settings that define the parameters and behavior of the simulation. Within the directory, there are three different files, 'controlDict', 'fvSchemes' and 'fvSolution'. 'controlDict' contains settings that control the overall behavior of the simulation, such as the time stepping scheme, start and end times of the simulation, and the time step size. 'fvSchemes' contains the discretization schemes for different terms in the governing equations and 'fvSolution' specifies the linear solvers and settings for solving the discretized equations.

C.1.2. Boundary and initial conditions

In the '0' directory, initial guesses can be assigned to the boundary and initial conditions, aiming to improve computational processes. These initial guesses come into play solely during the initial time step of the simulation. A well-informed initial guess significantly reduces the time necessary to reach convergence. As for the turbulent kinetic energy (k), turbulent dissipation rate (ε), and turbulent viscosity (ν_t), their initial value can be calculated using OpenCFD (2021):

$$k = \frac{3}{2}(uI)^2, \quad \text{with } I = 0.16Re^{-\frac{1}{8}} \tag{C.1}$$

$$\varepsilon = C_\mu^{\frac{3}{4}} \frac{k^{\frac{3}{2}}}{l} \tag{C.2}$$

$$\nu_t = C_\mu \frac{k^2}{\varepsilon} \tag{C.3}$$

where,

I	=	Turbulence intensity	$[-]$
I	=	Velocity	$[m/s]$
Re	=	Reynolds number	$[-]$
C_μ	=	Turbulence model constant	$[-]$
l	=	Turbulence length scale	$[m]$

C.2. Simulation results

Below the simulation results are shown of a simulation where a stone diameter of 245 mm, an initial velocity of 4.5 m/s, a pipe diameter of 1.5m and a height above the seabed of 1.1m is used.

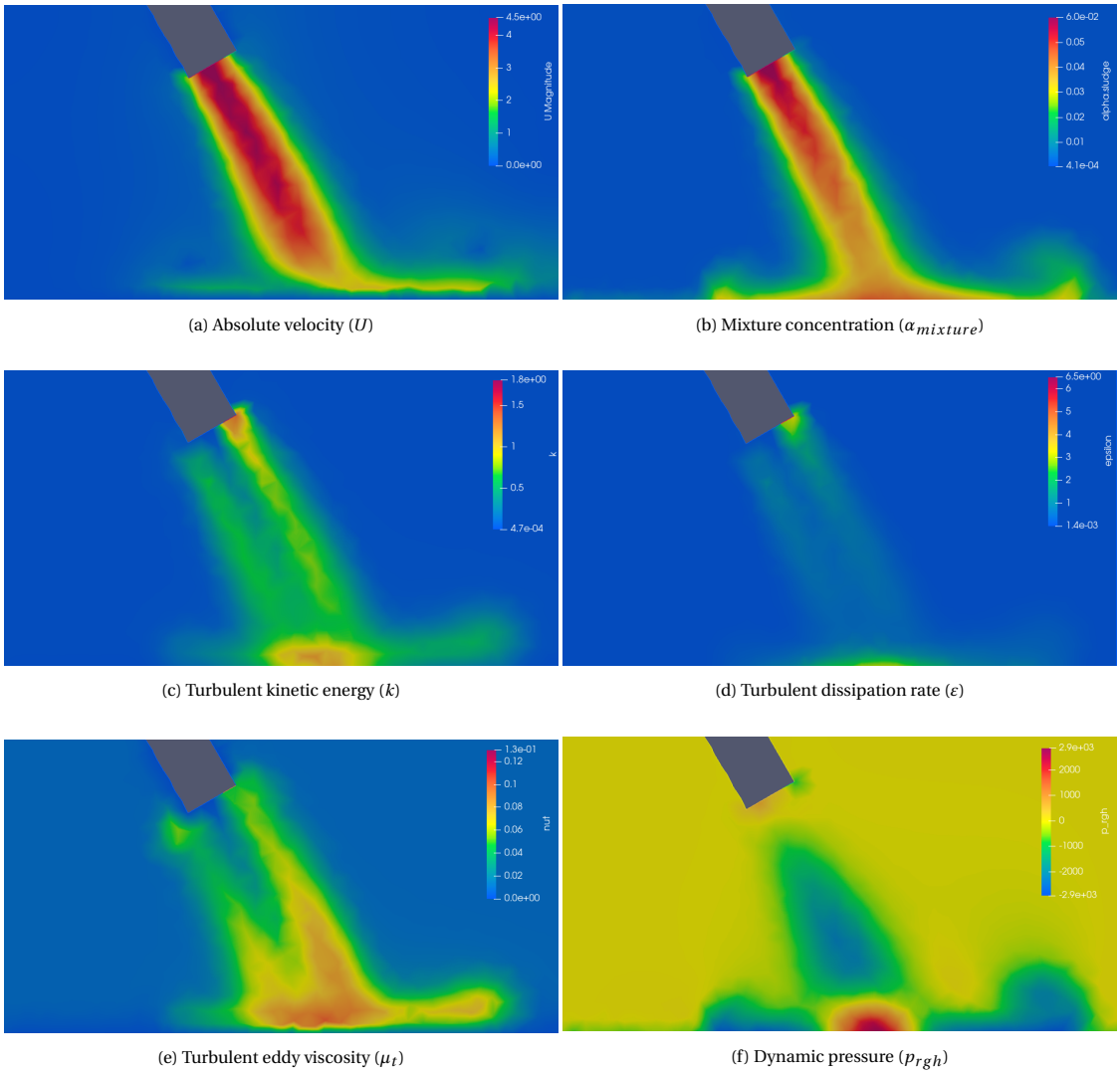

(a) Absolute velocity (U)

(b) Mixture concentration ($\alpha_{mixture}$)

(c) Turbulent kinetic energy (k)

(d) Turbulent dissipation rate (ε)

(e) Turbulent eddy viscosity (μ_t)

(f) Dynamic pressure (p_{rgh})

Figure C.2: Results from OpenFOAM simulation

C.3. Simulation results application of the model

The results of the simulations run to analyze the impact of external factors such as an obstacle or a current are shown in this Section. For the two cased used, the initial parameters are listed in Table 7.2. First, the simulation results of the added monopile are shown compared to a regular simulation. Afterward, the effect of the ambient current is shown for a varying velocity magnitude in three directions.

C.3.1. Simulation results including a monopile

This section presents the results of the simulations conducted in Section 7.1.1. The initial parameters for each case are as listed in Table 7.2. Each simulation is examined with and without the monopile to illustrate the impact of the monopile on the flow. The simulations in the xy plane are slices of the simulation just below the seabed and the simulation in the zy plane are sliced through the centerline of the fallpipe.

Results case 1

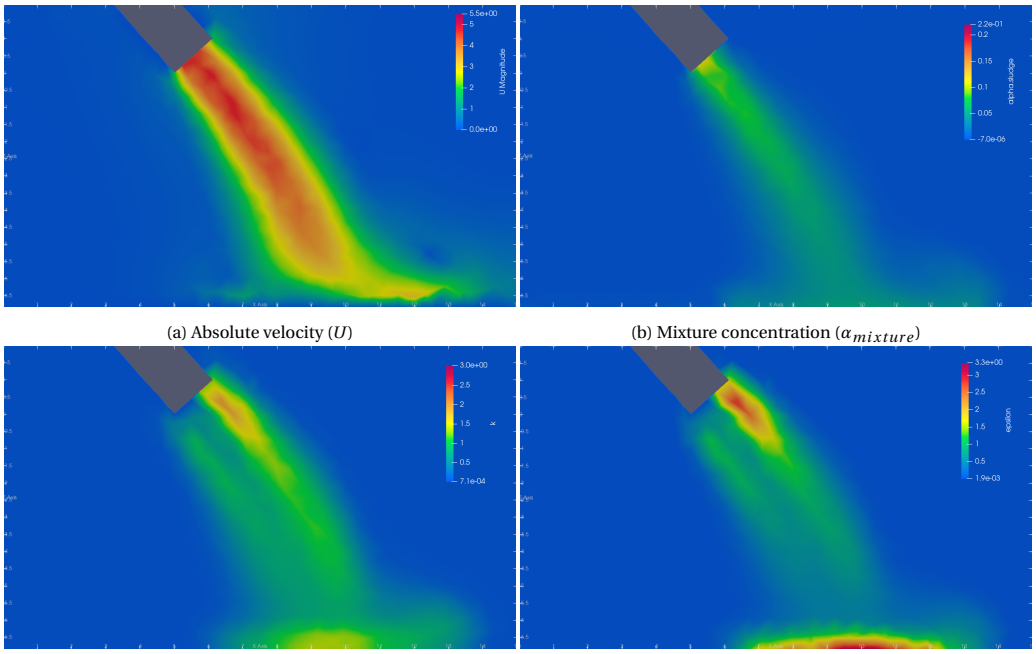

(a) Absolute velocity (U)

(b) Mixture concentration ($\alpha_{mixture}$)

(c) Turbulent kinetic energy (k)

(d) Turbulent dissipation rate (ε)

Figure C.3: Simulation case 1 (zy plane) - without monopile

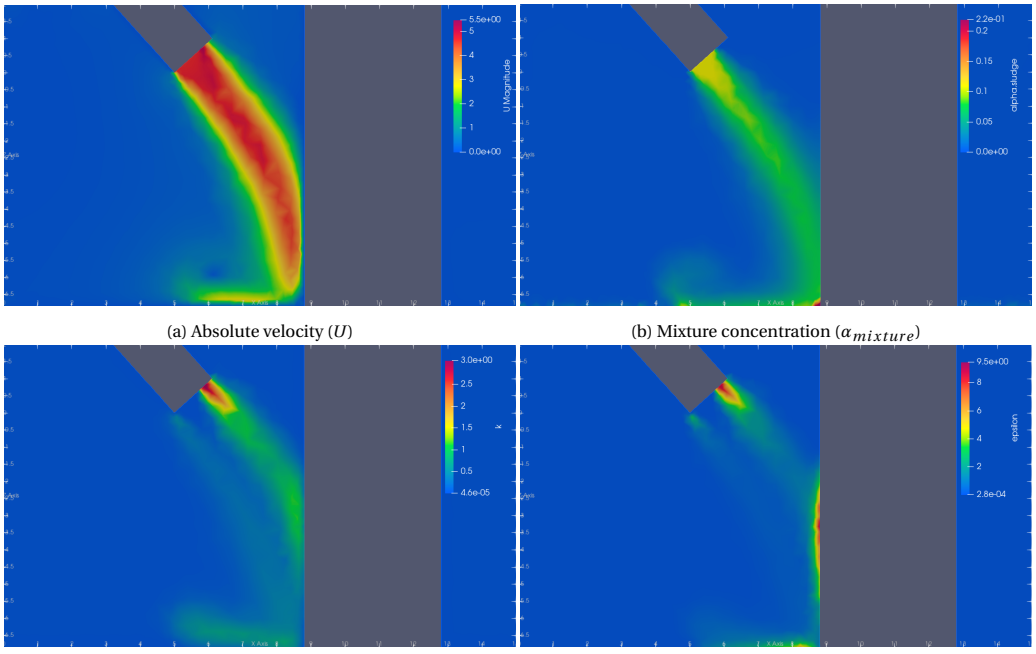

(a) Absolute velocity (U)

(b) Mixture concentration ($\alpha_{mixture}$)

(c) Turbulent kinetic energy (k)

(d) Turbulent dissipation rate (ε)

Figure C.4: Simulation case 1 (zy plane) - with monopile

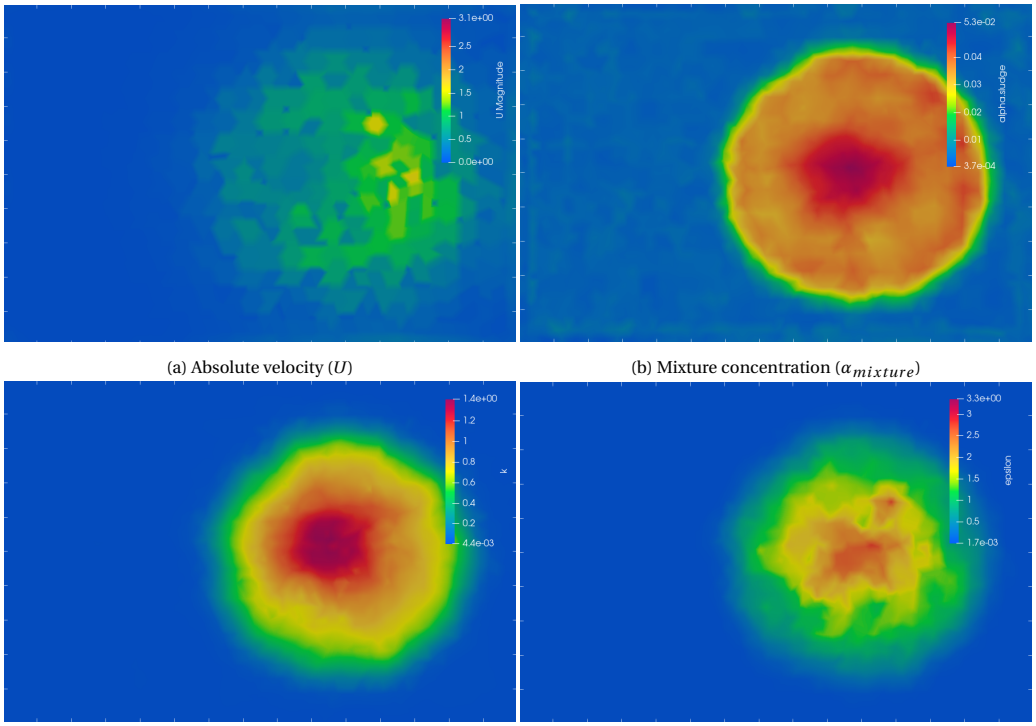

(a) Absolute velocity (U)

(b) Mixture concentration ($\alpha_{mixture}$)

(c) Turbulent kinetic energy (k)

(d) Turbulent dissipation rate (ε)

Figure C.5: Simulation case 1 (xy plane) - without monopile

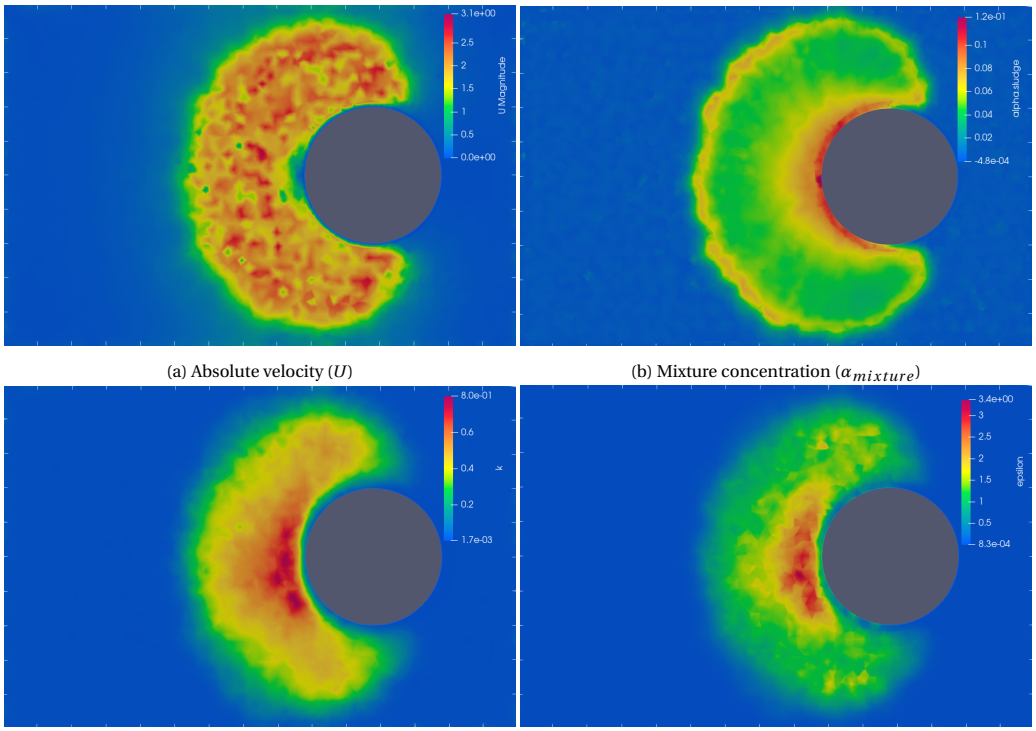

(a) Absolute velocity (U)

(b) Mixture concentration ($\alpha_{mixture}$)

(c) Turbulent kinetic energy (k)

(d) Turbulent dissipation rate (ε)

Figure C.6: Simulation case 1 (xy plane) - with monopile

Results case 2

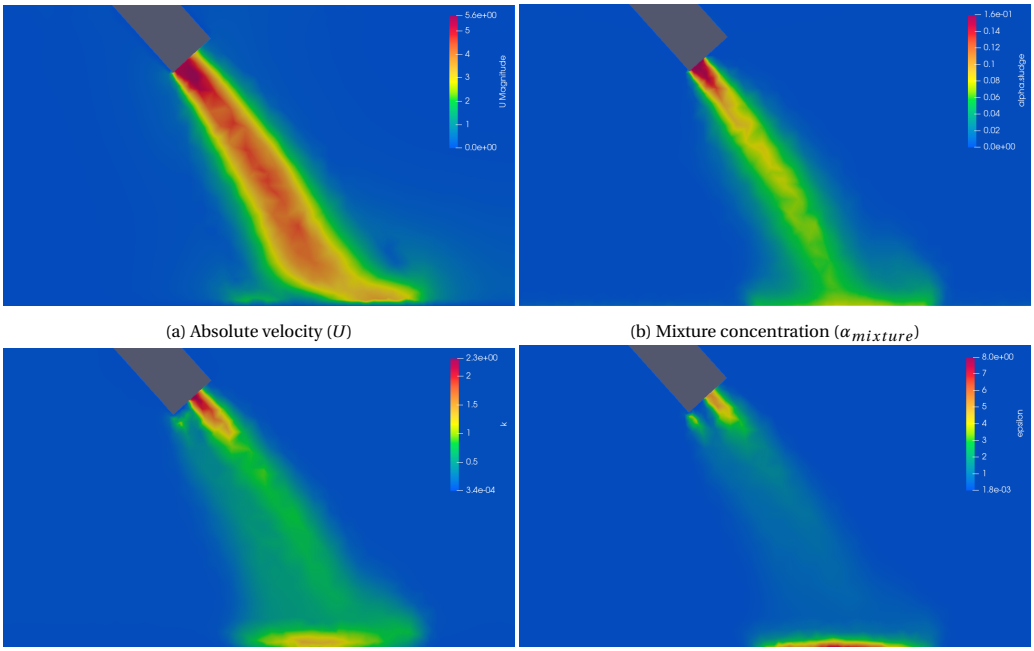

(a) Absolute velocity (U)

(b) Mixture concentration ($\alpha_{mixture}$)

(c) Turbulent kinetic energy (k)

(d) Turbulent dissipation rate (ε)

Figure C.7: Simulation case 2 (zy plane) - without monopile

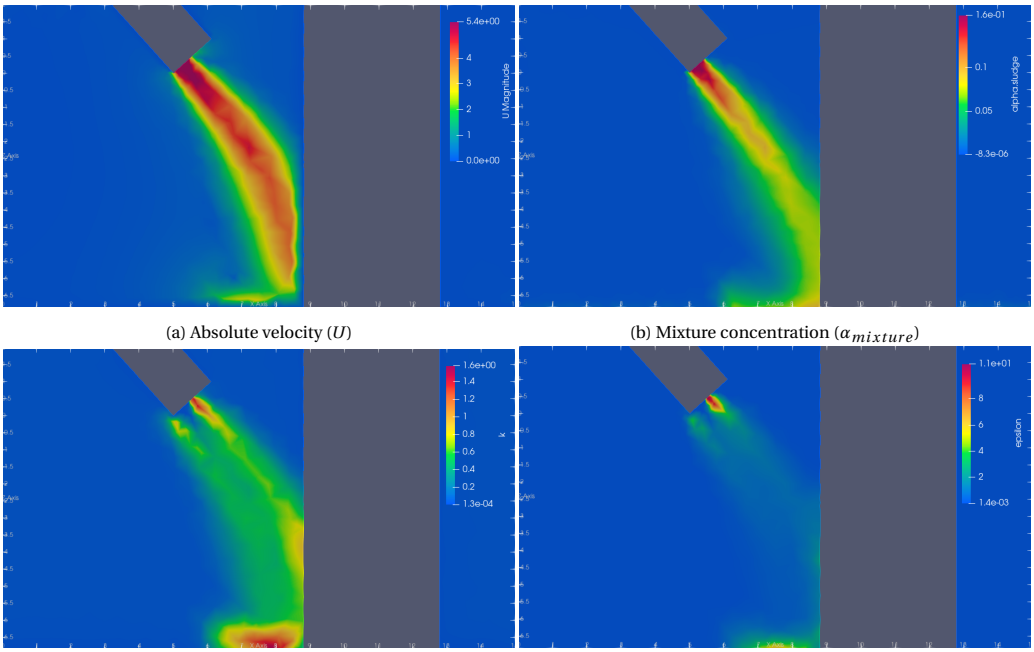

(a) Absolute velocity (U)

(b) Mixture concentration ($\alpha_{mixture}$)

(c) Turbulent kinetic energy (k)

(d) Turbulent dissipation rate (ε)

Figure C.8: Simulation case 2 (zy plane) - with monopile

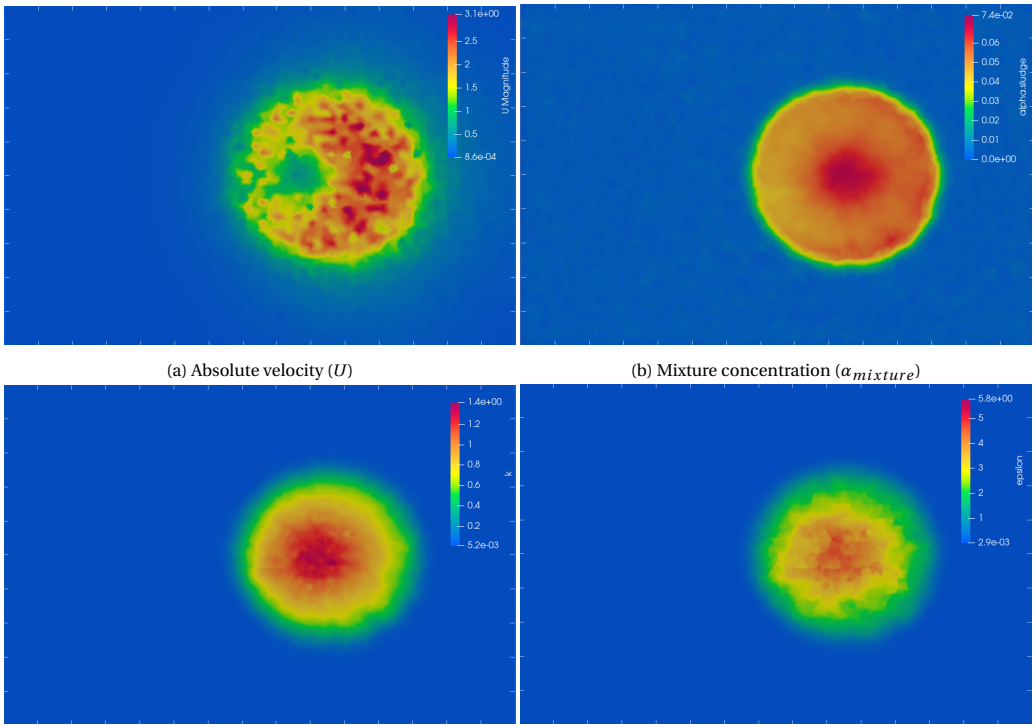

(a) Absolute velocity (U)

(b) Mixture concentration ($\alpha_{mixture}$)

(c) Turbulent kinetic energy (k)

(d) Turbulent dissipation rate (ε)

Figure C.9: Simulation case 2 (xy plane) - without monopile

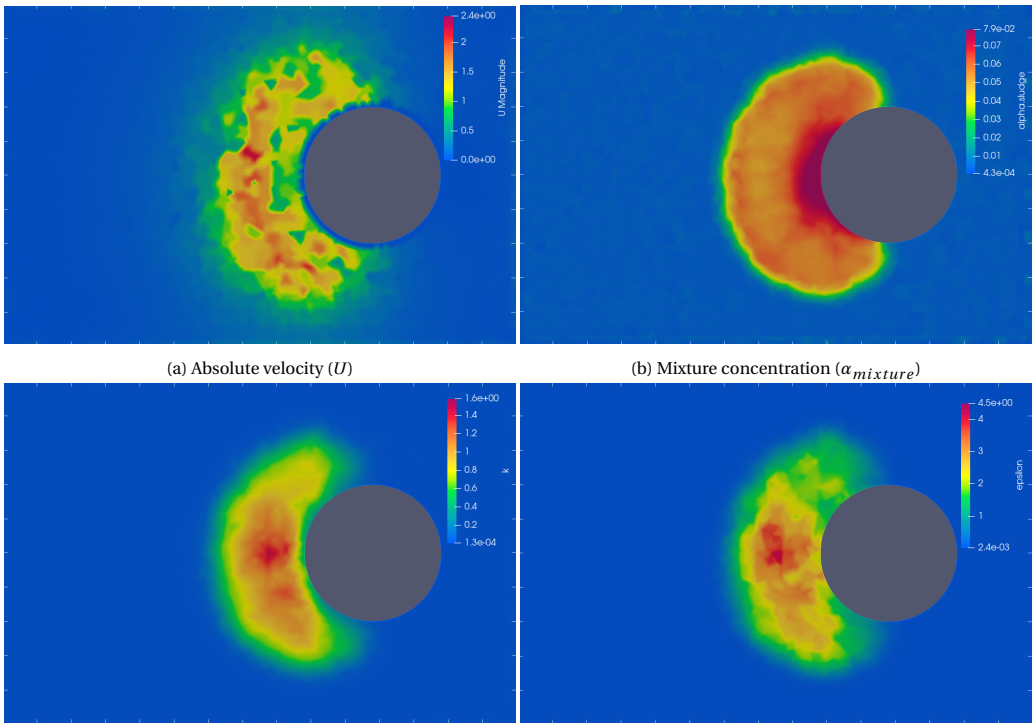

(a) Absolute velocity (U)

(b) Mixture concentration ($\alpha_{mixture}$)

(c) Turbulent kinetic energy (k)

(d) Turbulent dissipation rate (ε)

Figure C.10: Simulation case 2 (xy plane) - with monopile

C.3.2. Simulation results including an ambient cross current

This section contains the simulation results after applying a cross current to **case 1**.

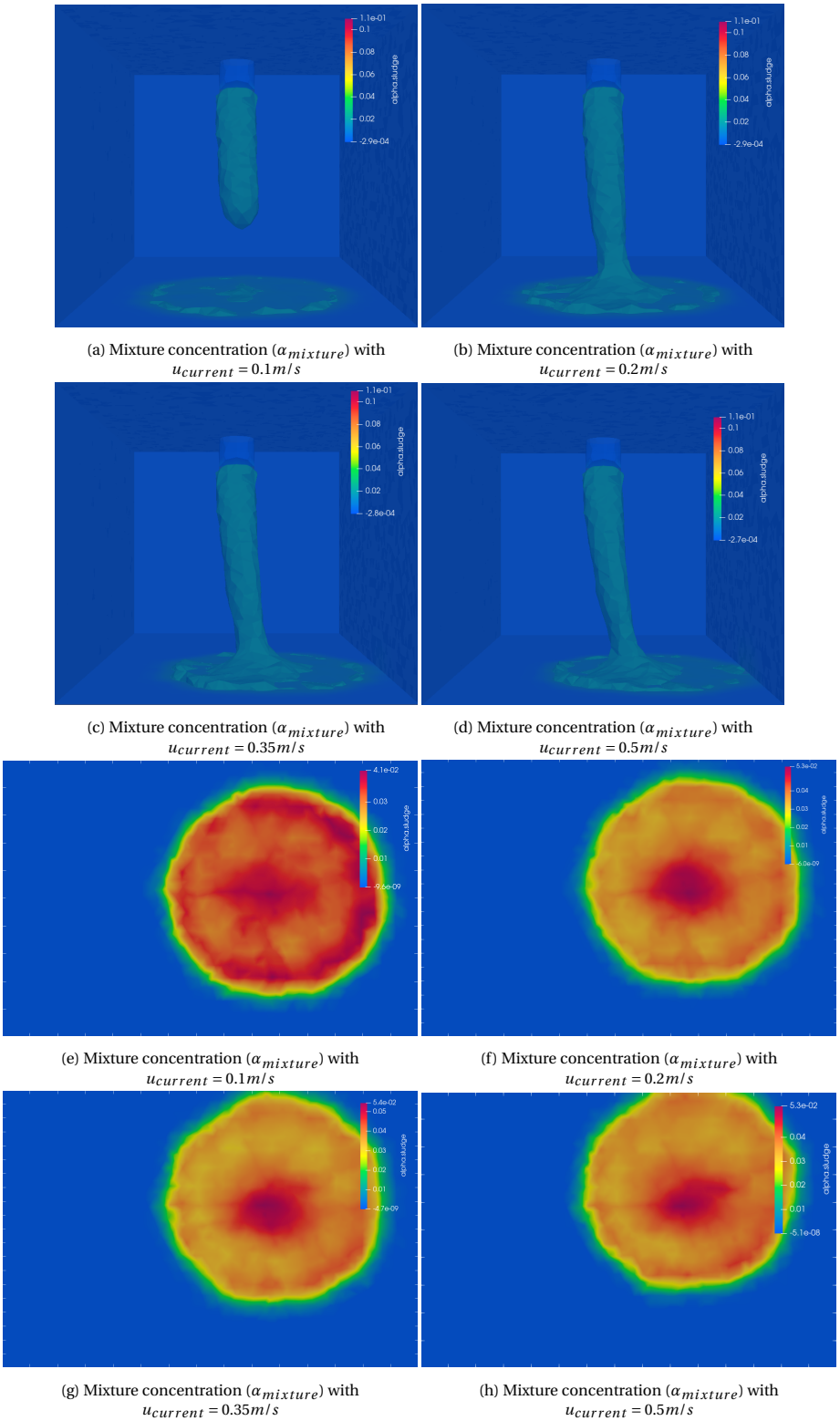

(a) Mixture concentration ($\alpha_{mixture}$) with $u_{current} = 0.1 m/s$

(b) Mixture concentration ($\alpha_{mixture}$) with $u_{current} = 0.2 m/s$

(c) Mixture concentration ($\alpha_{mixture}$) with $u_{current} = 0.35 m/s$

(d) Mixture concentration ($\alpha_{mixture}$) with $u_{current} = 0.5 m/s$

(e) Mixture concentration ($\alpha_{mixture}$) with $u_{current} = 0.1 m/s$

(f) Mixture concentration ($\alpha_{mixture}$) with $u_{current} = 0.2 m/s$

(g) Mixture concentration ($\alpha_{mixture}$) with $u_{current} = 0.35 m/s$

(h) Mixture concentration ($\alpha_{mixture}$) with $u_{current} = 0.5 m/s$

Figure C.11: Simulation results case 1 (zy plane) - with parallel ambient current

C.3.3. Simulation results including a parallel current

This section contains the simulation results after applying a parallel current to **case 1**.

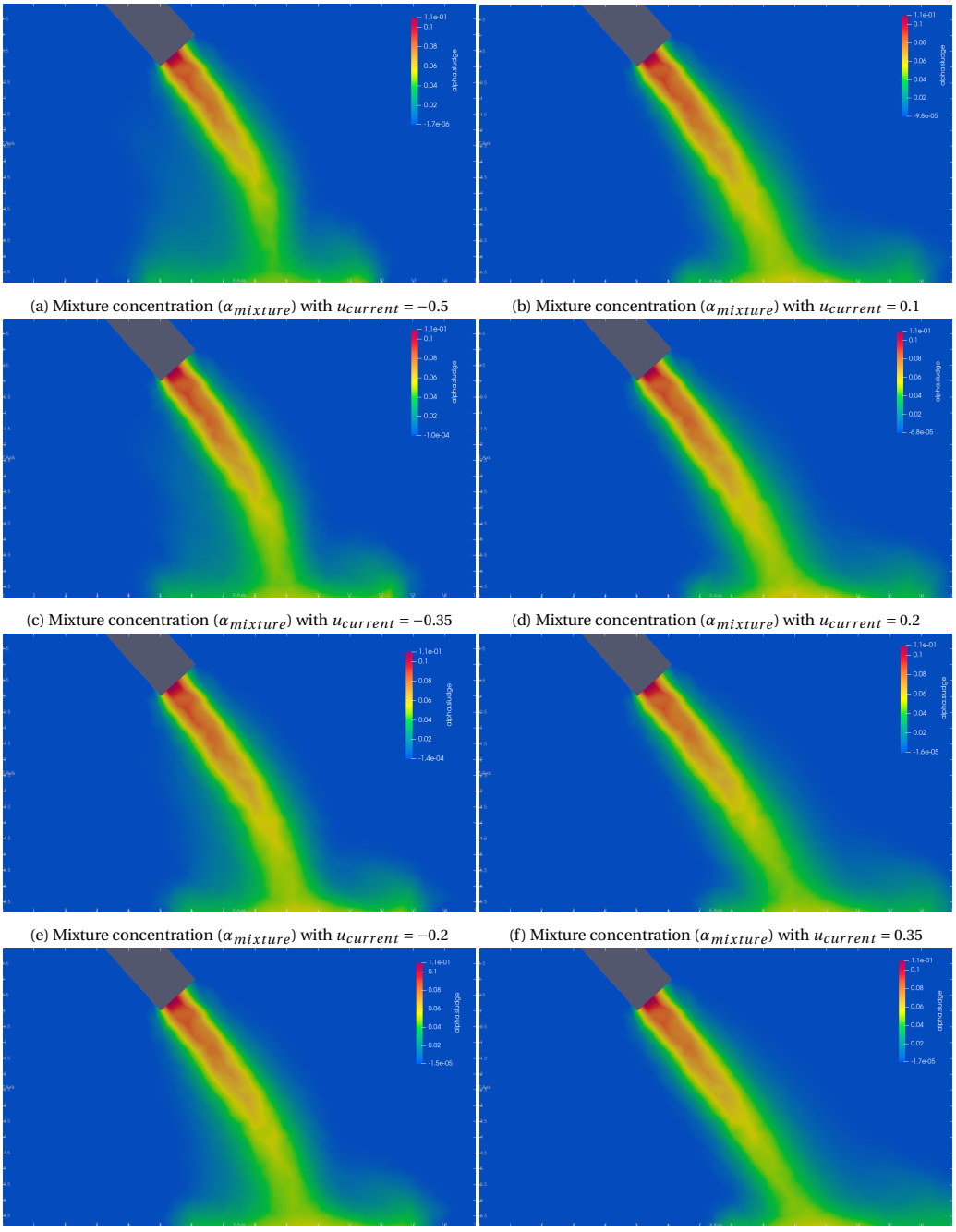

(a) Mixture concentration ($\alpha_{mixture}$) with $u_{current} = -0.5$

(b) Mixture concentration ($\alpha_{mixture}$) with $u_{current} = 0.1$

(c) Mixture concentration ($\alpha_{mixture}$) with $u_{current} = -0.35$

(d) Mixture concentration ($\alpha_{mixture}$) with $u_{current} = 0.2$

(e) Mixture concentration ($\alpha_{mixture}$) with $u_{current} = -0.2$

(f) Mixture concentration ($\alpha_{mixture}$) with $u_{current} = 0.35$

(g) Mixture concentration ($\alpha_{mixture}$) with $u_{current} = -0.1$

(h) Mixture concentration ($\alpha_{mixture}$) with $u_{current} = 0.5$

Figure C.12: Simulation results case 1 (xy plane) - with parallel ambient current

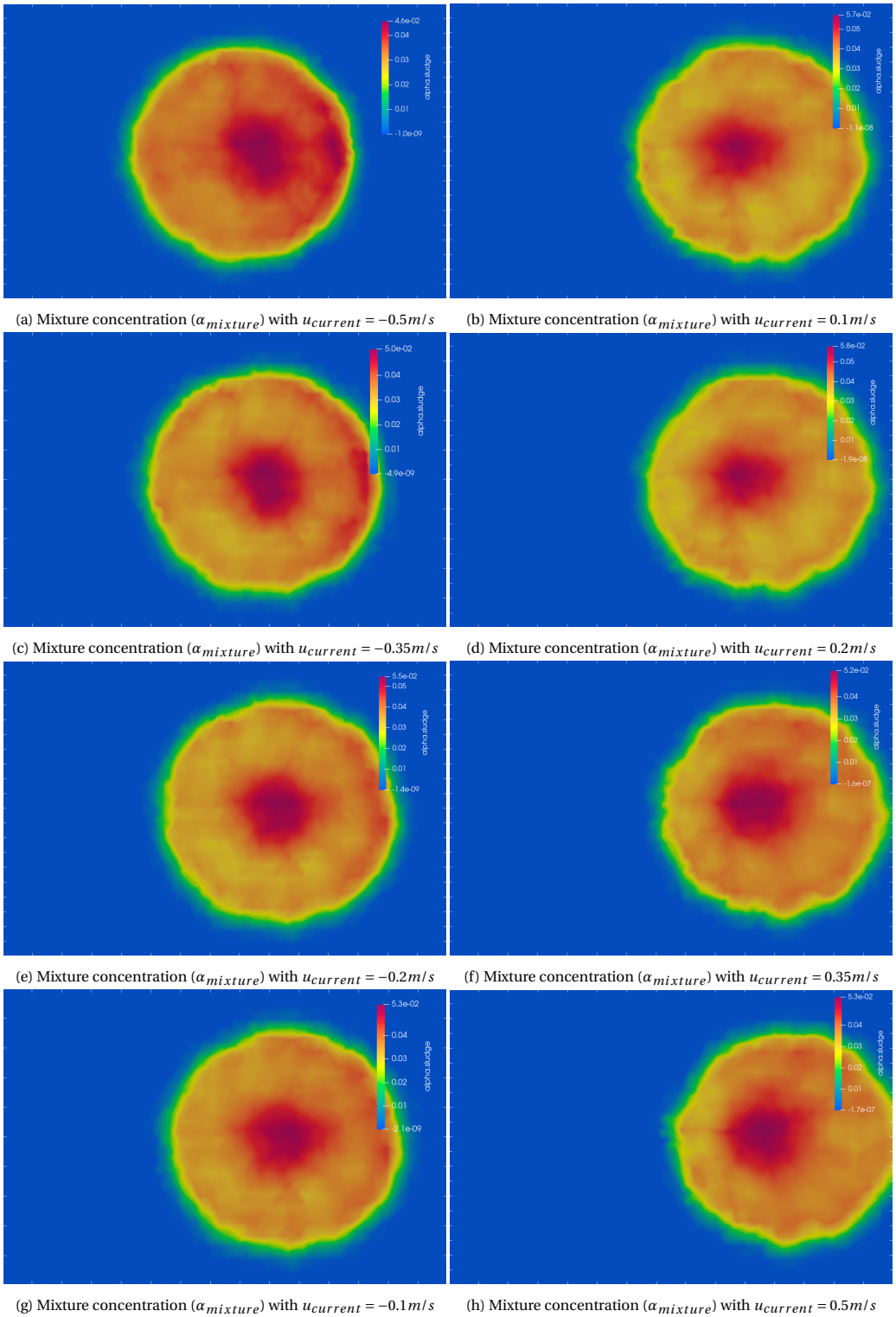

(a) Mixture concentration ($\alpha_{mixture}$) with $u_{current} = -0.5 m/s$

(b) Mixture concentration ($\alpha_{mixture}$) with $u_{current} = 0.1 m/s$

(c) Mixture concentration ($\alpha_{mixture}$) with $u_{current} = -0.35 m/s$

(d) Mixture concentration ($\alpha_{mixture}$) with $u_{current} = 0.2 m/s$

(e) Mixture concentration ($\alpha_{mixture}$) with $u_{current} = -0.2 m/s$

(f) Mixture concentration ($\alpha_{mixture}$) with $u_{current} = 0.35 m/s$

(g) Mixture concentration ($\alpha_{mixture}$) with $u_{current} = -0.1 m/s$

(h) Mixture concentration ($\alpha_{mixture}$) with $u_{current} = 0.5 m/s$

Figure C.13: Simulation results case 1 (zy plane) - with parallel ambient current

D

Appendix: MATLAB

D.1. Simulation results application of the model

This section contains the simulation result used in the application of the model for two different cases used in chapter 7. Case 1 used for both the simulations for the monopile and the added ambient currents, while case 2 is only used for the monopile simulations. Furthermore, all parameters used for these simulations are listed in tables D.1 and D.2. Where the values in the gray cells are calculated using the Sliding Bed Model by Vehmeijer (2022).

Table D.1: Constant parameters

	Value	Unit
Stone density ρ_s	2650	[kg/m^3]
Fluid density (water) ρ_f	1025	[kg/m^3]
Kinematic viscosity (water) μ	$1.42 \cdot 10^{-6}$	[m^2/s]
Gravitational constant g	9.81	[m/s^2]
Production P	1500	[kg/s]
Water depth h	6.85	[m]
Safety Margain SM	2.5	[m]
Diameter fallpipe D_{pipe}	1.5	[m]
Diameter monopile D_{mp}	4	[m]

Table D.2: Initial parameters used in the application of the model for two cases

Case	Fallpipe angle [deg]	Stone Diameter [mm]	Velocity [m/s]	β[rad]	C_{vb}[−]
1	48	245	4.65	1.76	0.11
2	48	150	5.40	1.37	0.16

Figures D.1 and D.2 present the simulation results for both cases without the inclusion of a monopile or ambient current. The simulation results considering the presence of a monopile, cross current, and parallel current are provided in Sections D.1.1, D.1.2, and D.1.3, respectively.

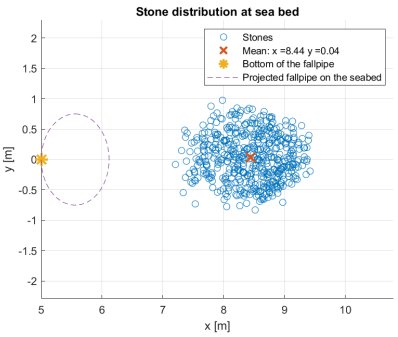

(a) Stone distribution at seabed

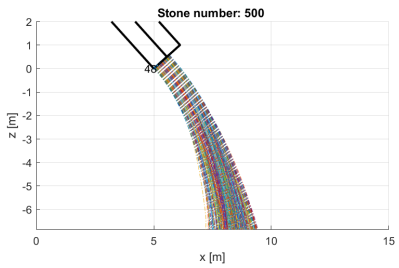

(b) Side view stone dispersion

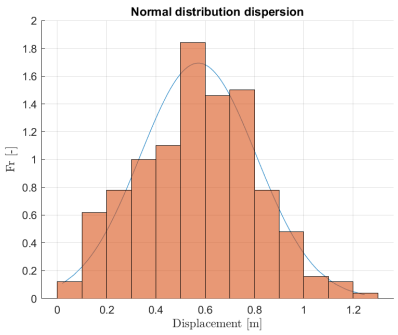

(c) Normal distribution mean displacement

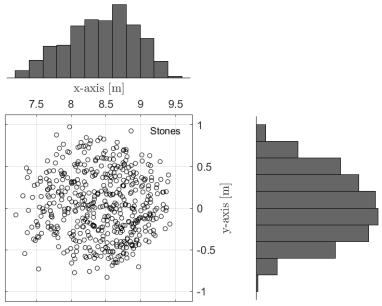

(d) Bivariate histogram from the seabed distribution

Figure D.1: Stone dispersion results in Matlab case 1

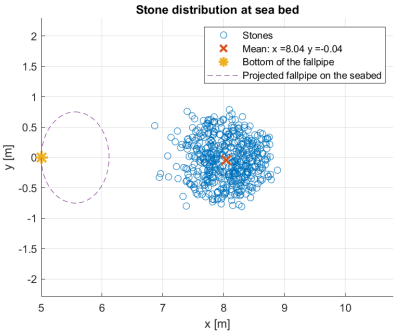

(a) Stone distribution at seabed

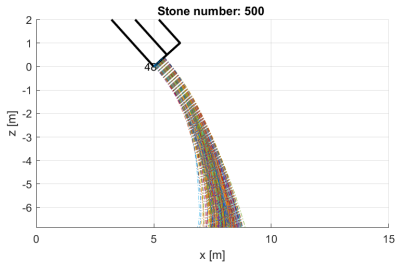

(b) Side view stone dispersion

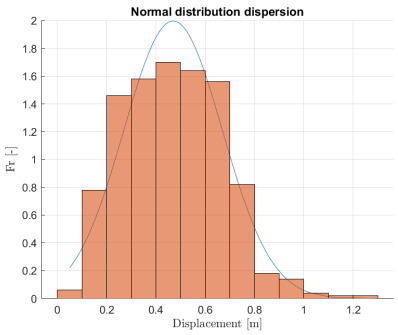

(c) Normal distribution mean displacement

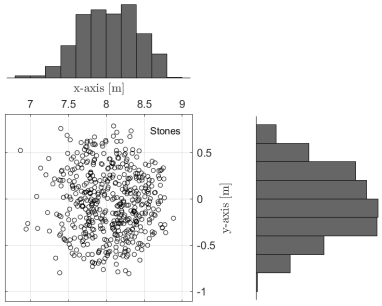

(d) Bivariate histogram from the seabed distribution

Figure D.2: Stone dispersion results in Matlab case 2

D.1.1. Simulation results including a monopile

This section contains the simulation results for both cases when adding a monopile to the geometry.

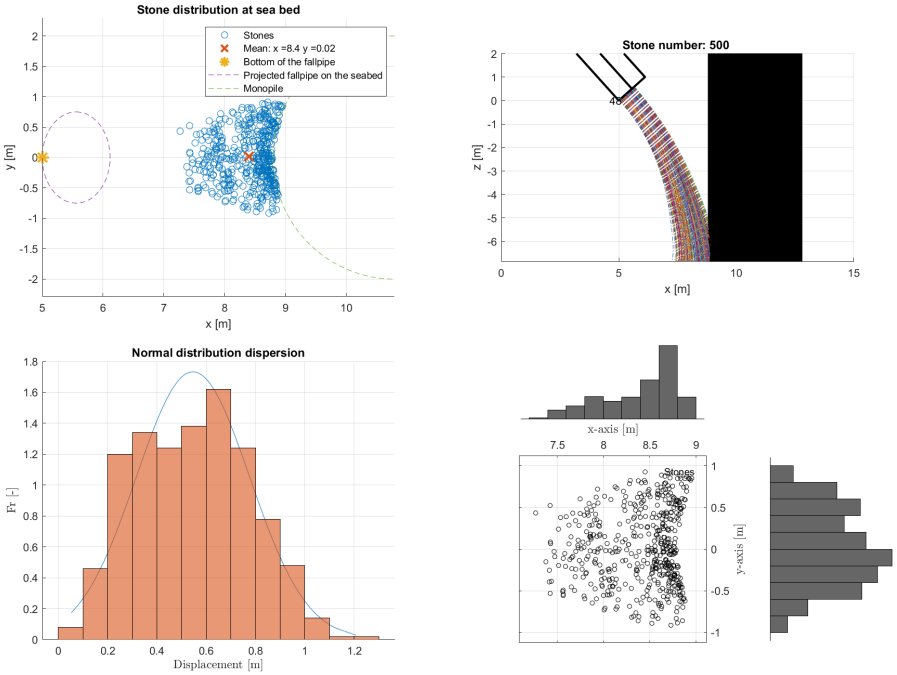

Figure D.3: Stone dispersion results in Matlab case 1 with a monopile

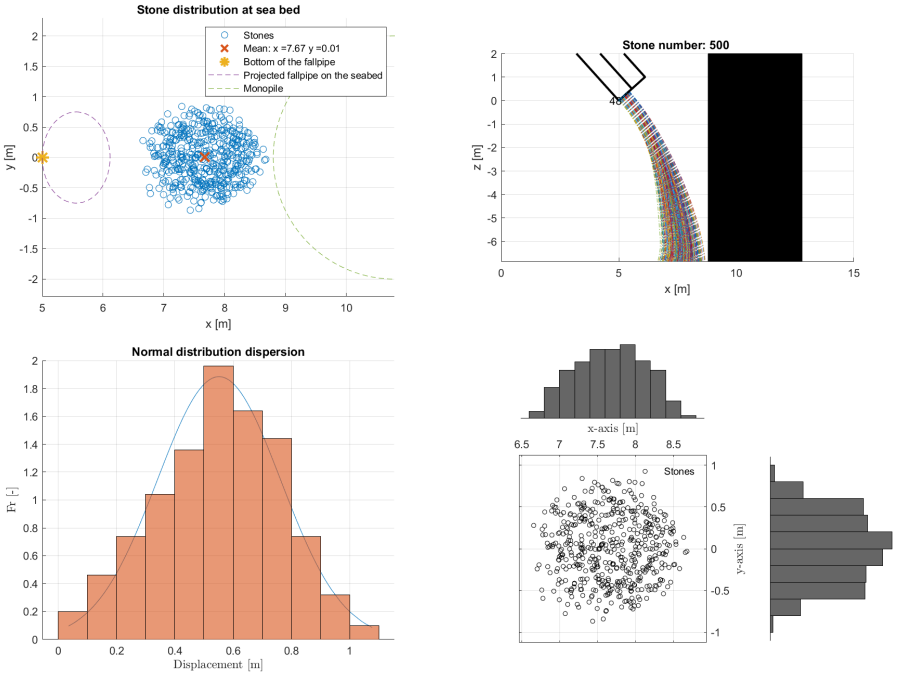

Figure D.4: Stone dispersion results in Matlab case 2 with a monopile

D.1.2. Simulation results including an ambient cross current

This section contains the simulation results after applying a cross current to **case 1**.

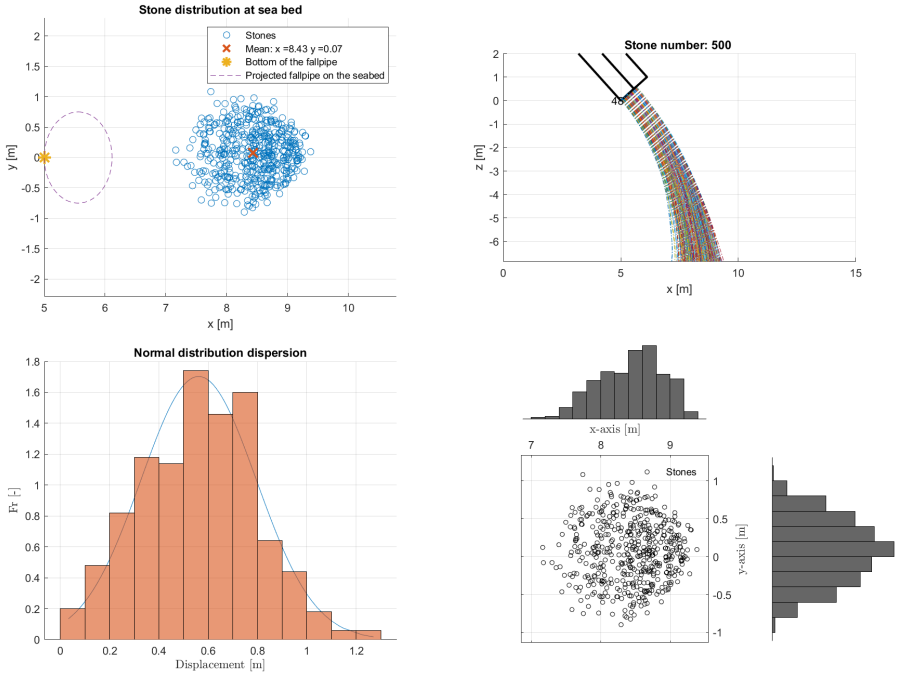

Figure D.5: Stone dispersion results in Matlab cross current of $u_{current} = 0.1 m/s$

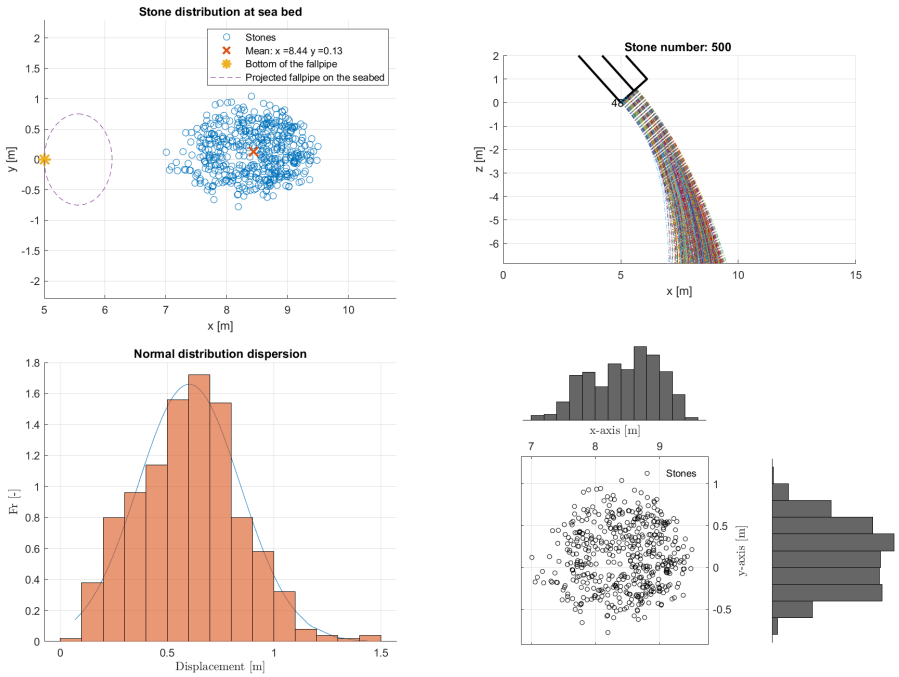

Figure D.6: Stone dispersion results in Matlab cross current of $u_{current} = 0.2 m/s$

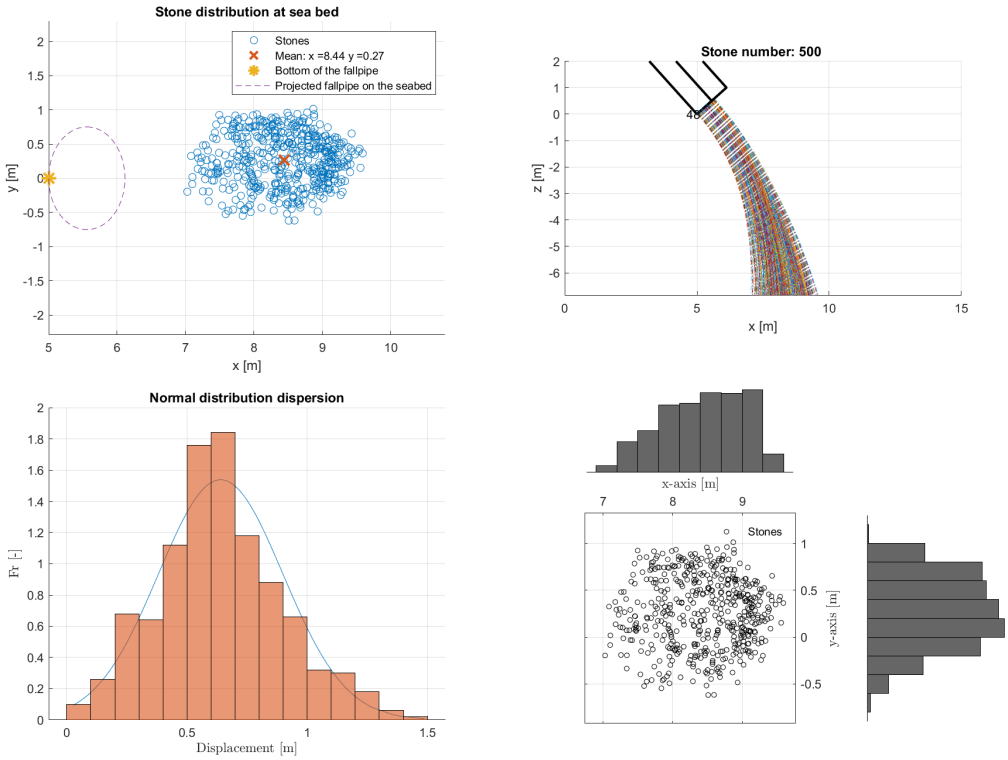

Figure D.7: Stone dispersion results in Matlab cross current of $u_{current} = 0.35 m/s$

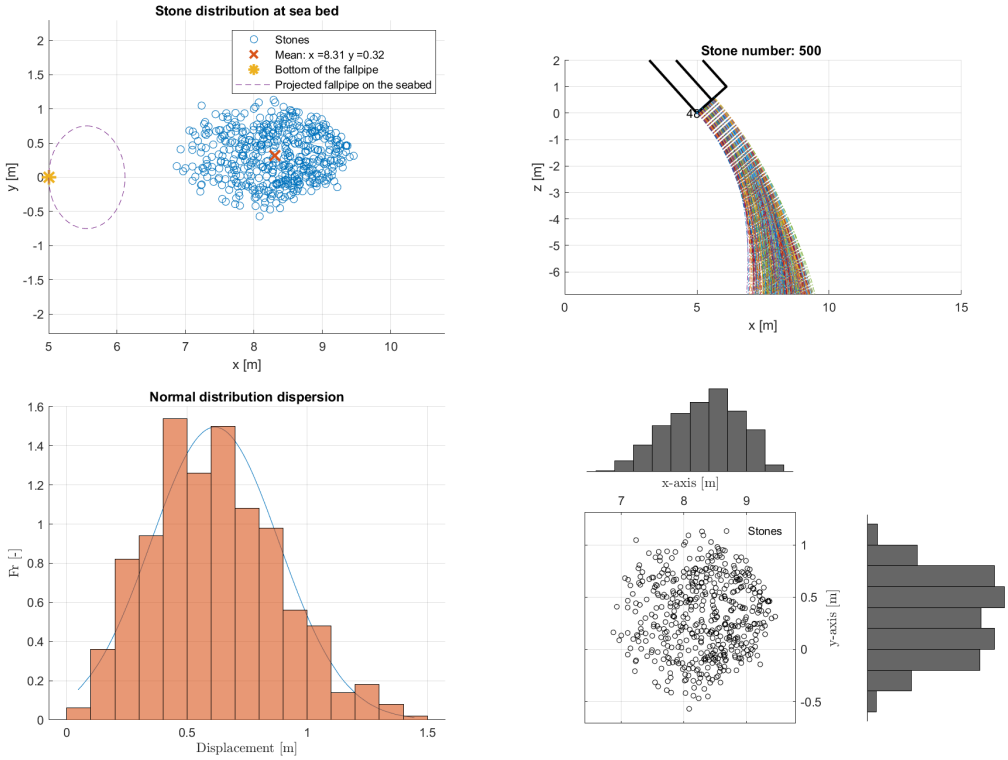

Figure D.8: Stone dispersion results in Matlab cross current of $u_{current} = 0.5 m/s$

D.1.3. Simulation results including an ambient parallel current

This section contains the simulation results after applying a parallel current to **case 1**.

Results current directed in the same horizontal direction as the jet

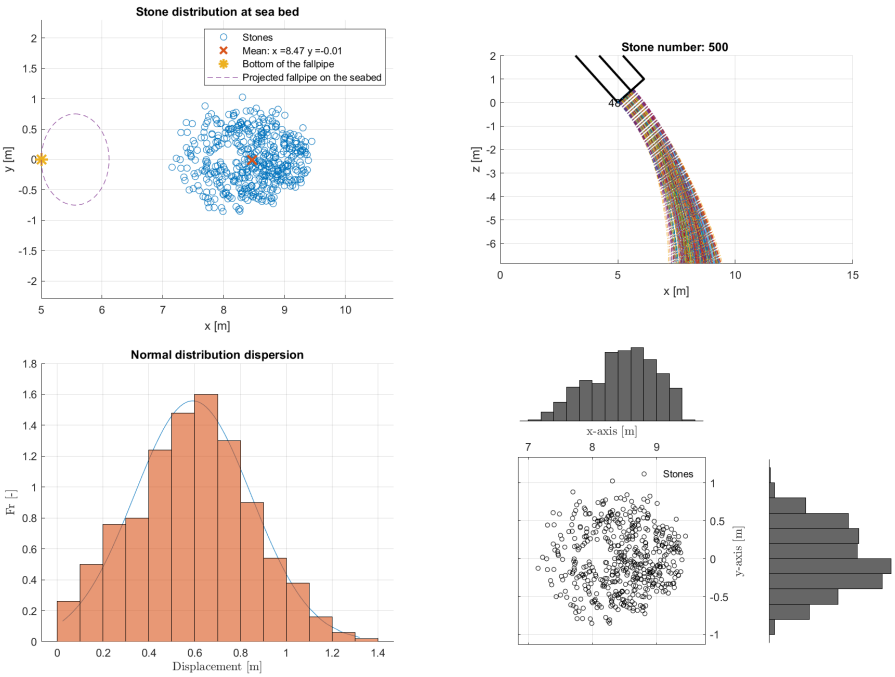

Figure D.9: Stone dispersion results in Matlab cross current of $u_{current} = 0.1 m/s$

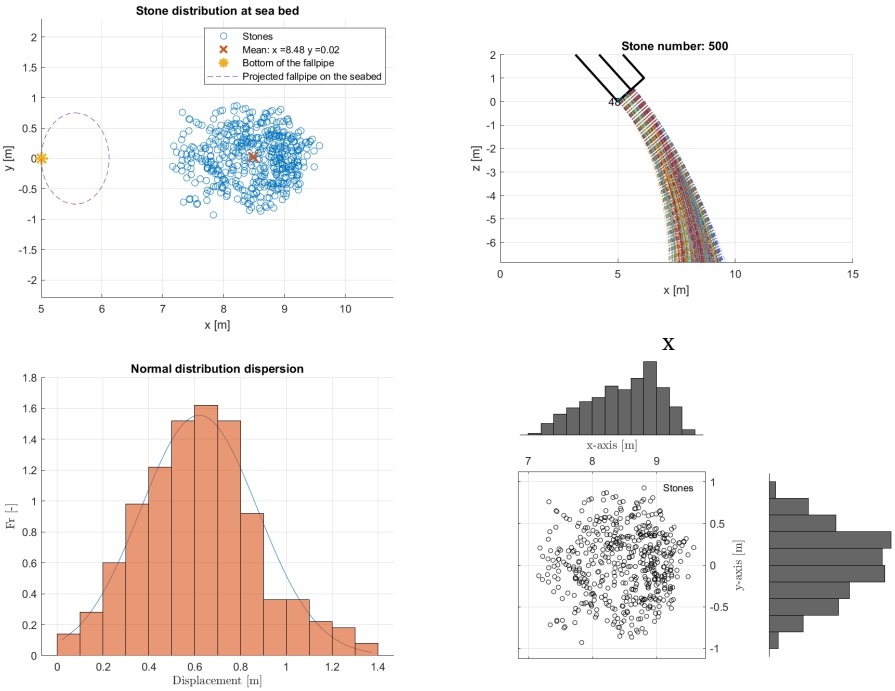

Figure D.10: Stone dispersion results in Matlab cross current of $u_{current} = 0.2 m/s$

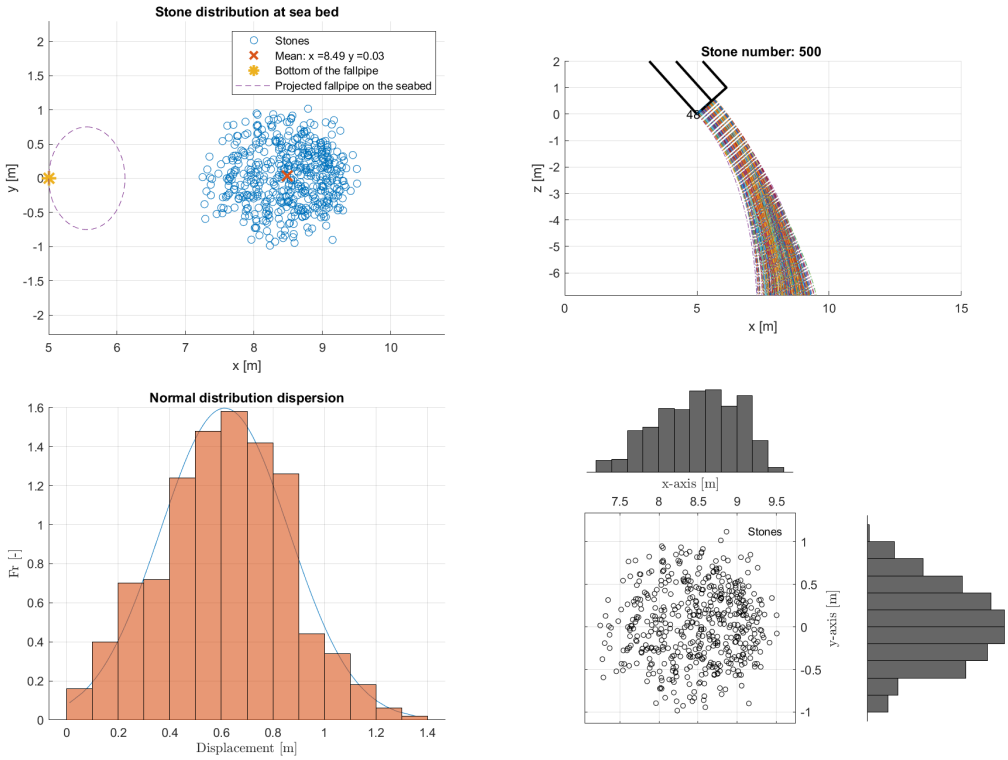

Figure D.11: Stone dispersion results in Matlab cross current of $u_{current} = 0.35 m/s$

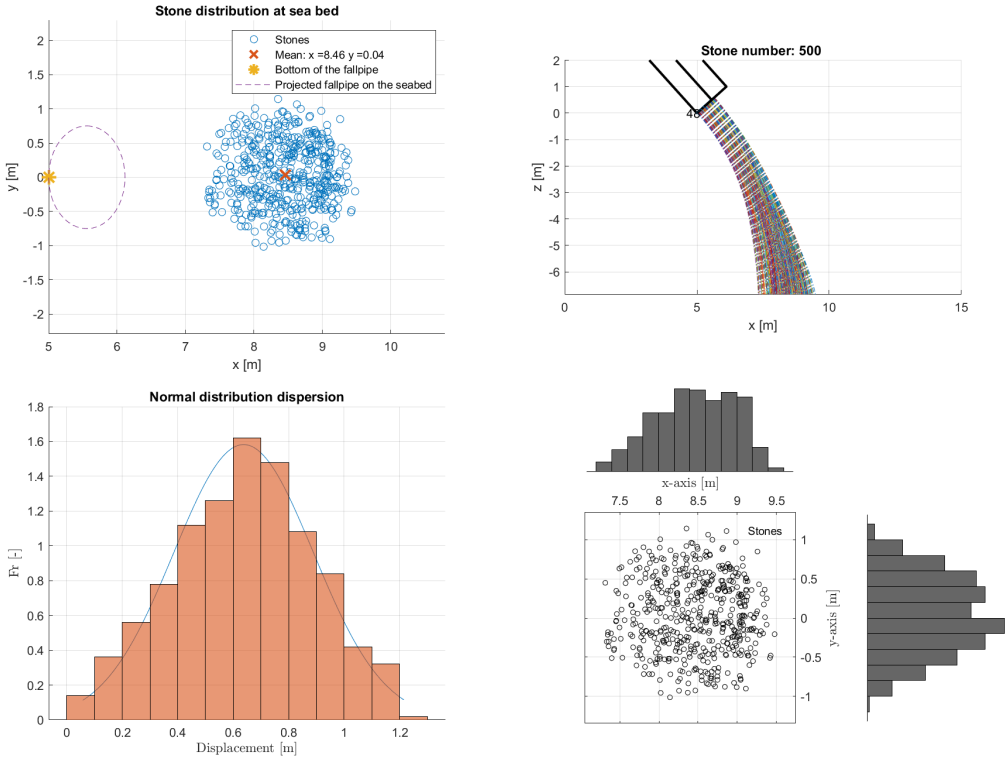

Figure D.12: Stone dispersion results in Matlab cross current of $u_{current} = 0.5 m/s$

Results Current directed in the opposite horizontal direction as the jet

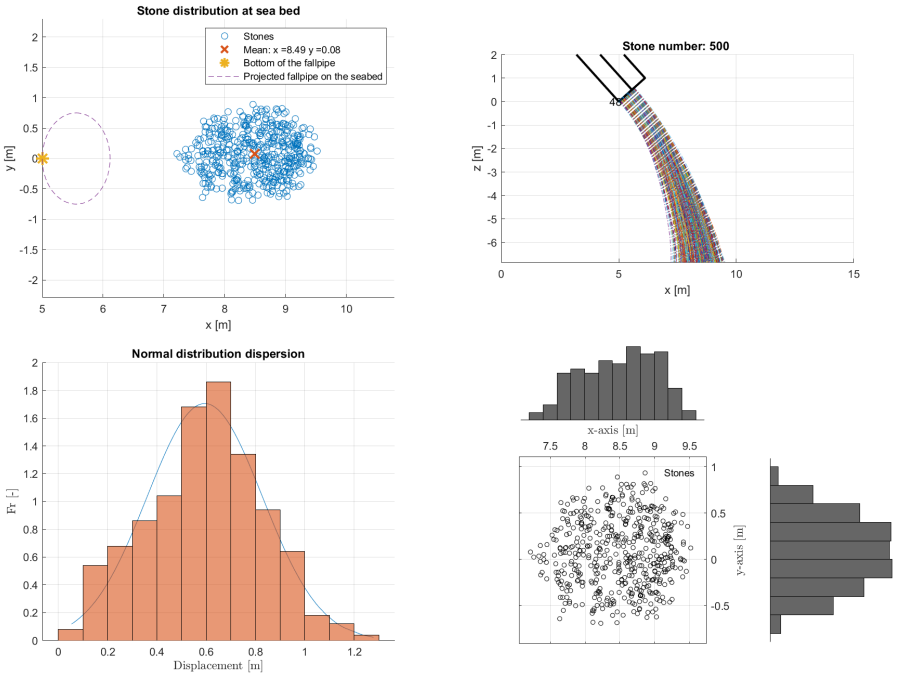

Figure D.13: Stone dispersion results in Matlab cross current of $u_{current} = -0.1 m/s$

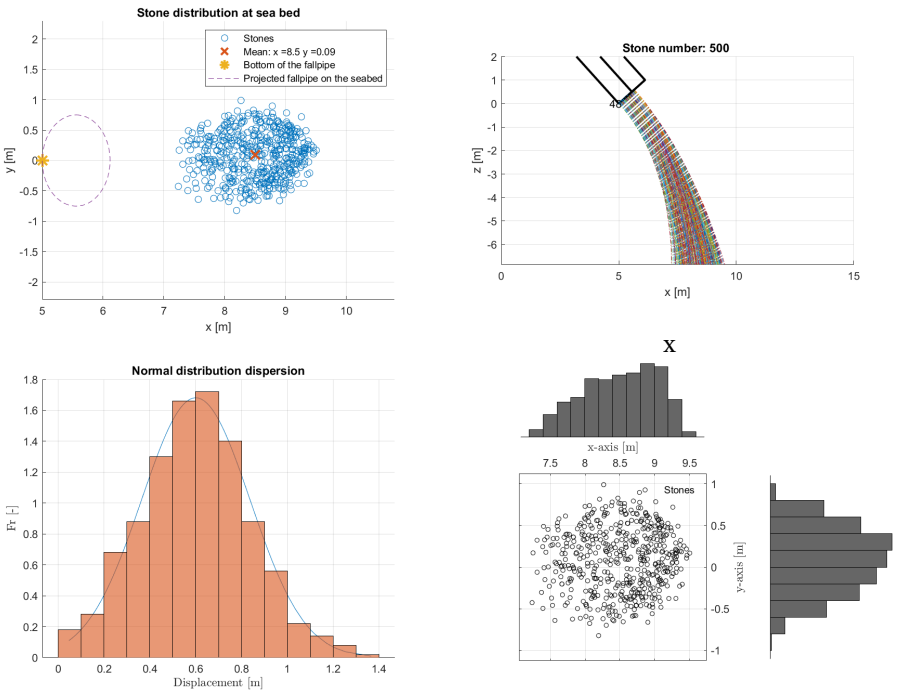

Figure D.14: Stone dispersion results in Matlab cross current of $u_{current} = -0.2 m/s$

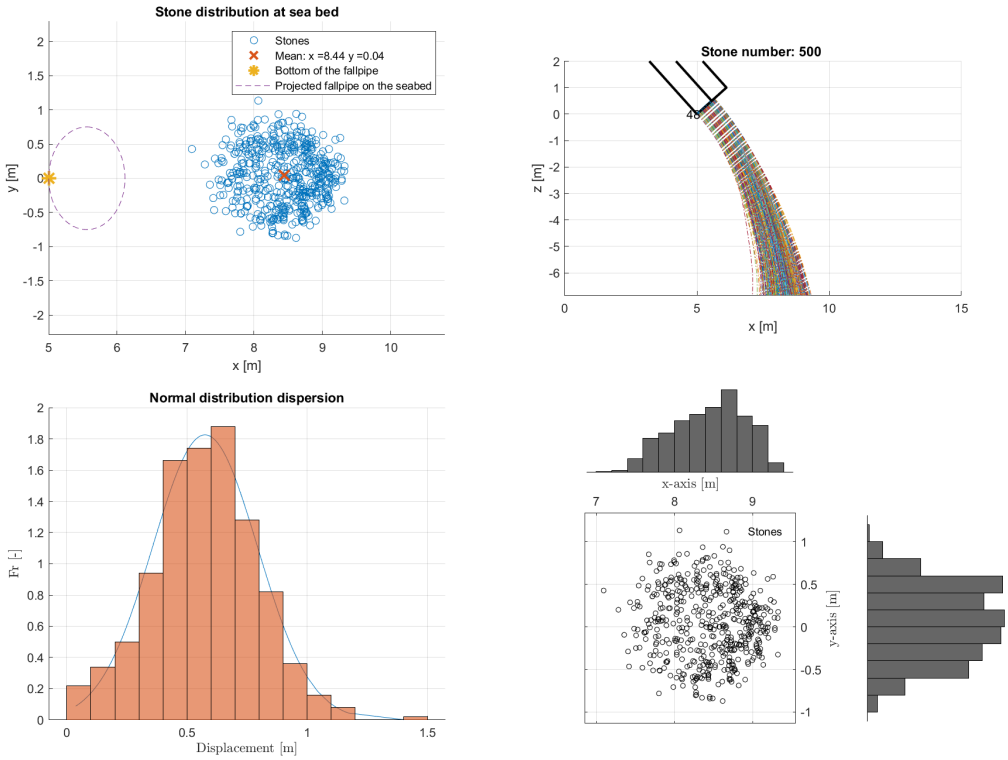

Figure D.15: Stone dispersion results in Matlab cross current of $u_{current} = -0.35 m/s$

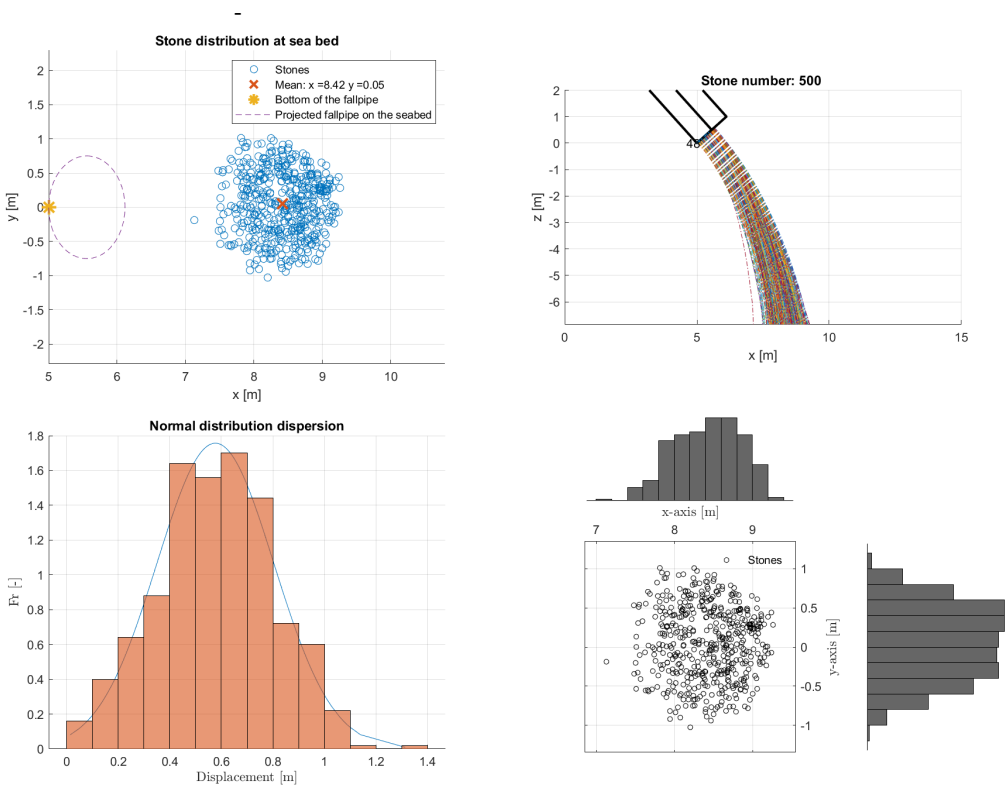

Figure D.16: Stone dispersion results in Matlab cross current of $u_{current} = -0.5 m/s$

D.1.4. Interpolation results

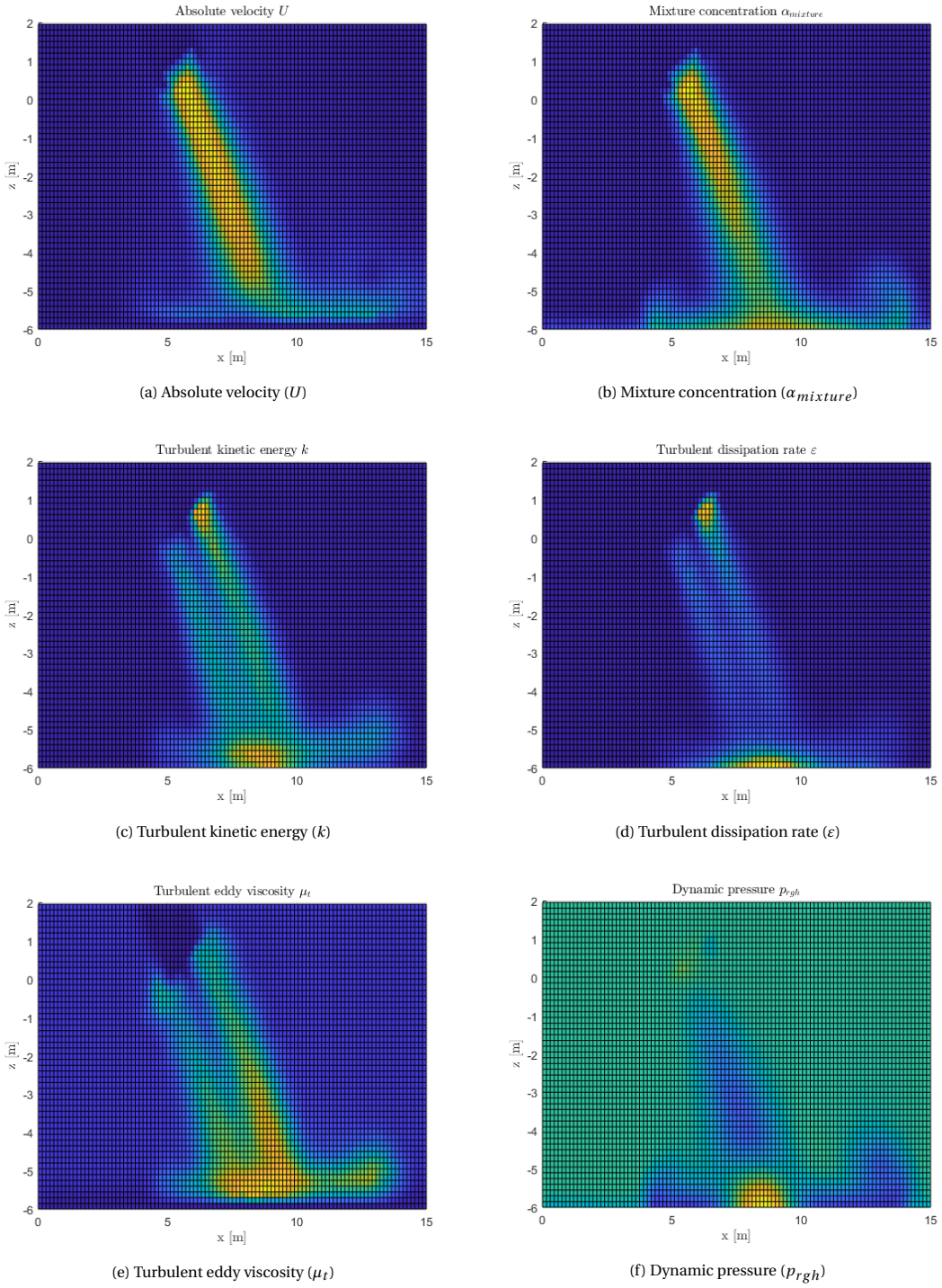

(a) Absolute velocity (U)

(b) Mixture concentration ($\alpha_{mixture}$)

(c) Turbulent kinetic energy (k)

(d) Turbulent dissipation rate (ε)

(e) Turbulent eddy viscosity (μ_t)

(f) Dynamic pressure (p_{rgh})

Figure D.17: Results from interpolated data in Matlab

D.2. MATLAB code

Function in MATLAB

```
1 % Matlab code used for modeling the dispersion of stones during subsea
```

```
% stone installation. The model combines the Single Stone Model by Manni
% & Vrijling and the Discrete Random Walk model described in ANSYS FLUENT
% 2021.

clear all;clc; close all

%% Initialize water depth and monopile

Monopile = 1;        % 1 turn on monopile, 0 turn off monopile.
h = 6.846;           % Water depth measured from the bottom of the fallpipe

%% Variables used for saving multiple figures at once

SIM = -0.5; % Used for saving figures and data
UU = 'Ux';  % Used for saving figures and data
number = 1; % Used for saving figures and data

%% Reading OpenFOAM files

if Monopile == 1
    M = csvread('SIM1_MP.csv');
else
    M = csvread('SIM1.csv');
end

Box = [0 15; -5 5; -h 2];   % x,y,z Dimensions of the box used
dx = 0.2;                   % Grid size

xLoc = M(:,1);
yLoc = M(:,2);
zLoc = M(:,3);
Ux = M(:,4);
Uy = M(:,5);
Uz = M(:,6);
alpha_sludge = M(:,7);
eps = M(:,8);
k = M(:,9);
nut = M(:,10);
p = M(:,11);
p_rgh = M(:,12);

%% Variables

%Lx=5; %[m], domain length x
%Ly=5; %[m], domain length y
%Lz=-6; %[m], domain length z

No_of_stones = 10;
Fallpipe_angle = 48;
D_pipe = 1.5;                       % Pipe diameter
d = 245/1000;                       % 0.3; %15 / 1000; %Diameter stones
L=d/0.54;                           % To have mean Cd = 1.42, choose L=d/0.54. Otherwise pick L=d;
INITIAL_velocity = 4.65;             % Initial velocity [m/s]
Beta = 1.76;                         % Beta [Rad]

n = 2.4;                            % Hindered settling exponent [-]
c = 0.11;                           % Concentration [-]
St = 0.2;                           % Strouhall number [-] Determines the effect of the random walk
    according to the Single Stone Model
C_mu = 0.09;                        % Turbulence model [-] constant k-eps model
N = 2800;                           % Number of timesteps [-]
Time = 10;                          % Total time [s]
dt = Time/(N-1);                    % Timesteps [s]
rho_f = 1020;                       % Water density [kg/m^3]
rho_s = 2650;                       % Stone density [kg/m^3]
rho_r = ( rho_s-rho_f ) /rho_f ;    % Relative density [kg/m^3]
g = 9.81;                           % Gravitational constant [m/s^2]
```

```
kvisc = 1.42*10^-6;                 % Kinematic viscosity water [m^2/s]
Radius_monopile = 2;                % Radius from the monopile [m]
Safety_Margin = 2.5;                % Safety margin [m] (Fallpipe will be positioned at the safety margin wrt to the monopile)

Lz=Box(3,1);                        % Water depth [m]

Eps = 1;                            % Shape factor stones cube 1, sphere pi/6
mu = 1;                             % Shape factor stones cube 1, sphere pi/4
lambda = 3.5;                       % 2 times the shape factor of a stone psi (F=0.5*psi *rho_f*v^2*D^2*CL -> F=lambda *rho_f*v^2*D^2*CL) This factor is uncertain as it depends on the shape of the stone. This also influences the drag coefficients.


%% Scaling variables.

I_SSM = 1;              % Coefficient depending on the direction of the flow in connection with the orientaion of the stone and on the sharpness of the edges of the stone
Scale_T_SSM = 1;        % Scale time duration for each directional change of the single stone model
EH=1;                   % Scales the fluid field characteristics from OpenFOAM
CoR = 0.7;              % Coefficient of restitution, used to estimate the loss in energy upon impact with the monopile

I_startloc = 1;         % 0: starting location stones at the bottom of the fallpipe, 0.5: at the middle, 1: uniformly distributed below the bed height.

sig = 1;                % Standard deviation of the DRW model Unit-variance -> tends towards 1. Lowering it leads to less dispersion

HinderedSettling = 1;   % 1 turn on, 0 turn off.

%% Basic calculations

gamma =sqrt(2*mu/Eps);
mean_Cd = 0.54*L/d + 0.42;
sigma_Cd = 0.30;
Cd = normrnd(mean_Cd,sigma_Cd,1,No_of_stones);  % Cd
CL = 0.95 * sqrt(0.5*Cd);                       % Dragcoefficient in the horizontal direction
Cd_ver = sqrt(0.5*Cd);                          % Drag coefficient in the vertical direction

A = pi*d^2;                                     % Object area
As = 0.5*pi*d^2;                                % Object area
%V = pi/6 * d^3;                                % Volume sphere
V = d^3;                                        % Volume cube
Beta_height = (1-cos(Beta))*D_pipe/2;           % Bed height in meters

M = rho_s * V; % Mass of a single stone
Ma = rho_f * V/2; % Added mass (Ravelli)

HS = 1;

if HinderedSettling == 1
    HS = (1-c)^n;
end

PosNeg = [-1 1];    % Can be used with PosNeg(randi([1 numel(PosNeg)])) to pick either -1 or 1 randomly

%% Implementing openFoam velocity field data


FUx = scatteredInterpolant(xLoc,yLoc,zLoc,Ux,'linear');
FUy = scatteredInterpolant(xLoc,yLoc,zLoc,Uy,'linear');
FUz = scatteredInterpolant(xLoc,yLoc,zLoc,Uz,'linear');
FU = scatteredInterpolant(xLoc,yLoc,zLoc,sqrt(Uz.^2+Uy.^2+Ux.^2),'linear');

Fk = scatteredInterpolant(xLoc,yLoc,zLoc,k,'linear');
```

```
127 Feps = scatteredInterpolant(xLoc,yLoc,zLoc,eps,'linear');
128 Fnut = scatteredInterpolant(xLoc,yLoc,zLoc,nut,'linear');
129
130 xBox = (Box(1,1):dx:Box(1,2));
131 yBox = (Box(2,1):dx:Box(2,2));
132 zBox = (Box(3,1):dx:Box(3,2));
133 [xq,yq,zq] = meshgrid(xBox,yBox,zBox);
134
135 u_wx = FUx(xq,yq,zq)*EH;
136 u_wy = FUy(xq,yq,zq)*EH;
137 v_w = FUz(xq,yq,zq)*EH;
138 U_w = FU(xq,yq,zq)*EH;
139
140
141 k = Fk(xq,yq,zq)*EH;          % k = 1.5*(U*I)^2;;
142 eps = Feps(xq,yq,zq)*EH;      % eps = C_mu^(3/4) * k^(3/2) / Le; %Turbulent dissipation rate
143 nut = Fnut(xq,yq,zq)*EH;
144
145 X = reshape(xq(1,:,1),[],1);
146 Y = reshape(yq(:,1,1),[],1);
147 Z = reshape(zq(1,1,:),[],1);
148
149 %% Initiate fallpipe plot
150
151 Pipe_start_x = 5;
152
153 %hold on
154 figure(1)
155 hold on
156 grid on
157 xlabel('x [m]')
158 ylabel('y [m]')
159 zlabel('z [m]')
160
161 text(Pipe_start_x-0.4,-0.2, num2str(Fallpipe_angle)) %Display pipe angle
162 view([22, 25.5]) % give a 3d view
163
164
165 % Calculate and assign starting location of the stones
166 R = D_pipe/2;
167 x0 = 0; % Center of the circle in the x direction before rotation.
168 y0 = 0; % Center of the circle in the y direction before rotation.
169
170 theta = asin((Beta_height-D_pipe/2)/(D_pipe/2));
171 t = 2*pi*rand(1,No_of_stones);%t = (-pi/2+theta)*rand(1,n);
172 rx = R*sqrt(rand(1,No_of_stones));
173 x = x0 + rx.*sin(t);
174 y = y0 + rx.*cos(t);
175 z = zeros(1,No_of_stones);
176
177 for i=1:No_of_stones
178     while x(i) >= Beta_height-R          % Rerolls values above the beta height to have random
          values below beta height
179         t = 2*pi*rand(1);
180         rx = R*sqrt(rand(1));
181         x(i) = rx*sin(t);
182         y(i) = rx*cos(t);
183     end
184 end
185 xyz = [x;y;z];
186 RStonesxyz = roty(Fallpipe_angle-90)*xyz;
187
188 RStonesxyz(1,:) = RStonesxyz(1,:) + Pipe_start_x + sind(Fallpipe_angle)*D_pipe/2;
189 RStonesxyz(3,:) = RStonesxyz(3,:) + cosd(Fallpipe_angle)*D_pipe/2;
190
191 plot3(RStonesxyz(1,:),RStonesxyz(2,:),RStonesxyz(3,:),'.'); axis equal;
192
```

```
193 % Drawing pipe outline
194 % (fallpipe circle)
195 x_pipe = x0 + R*sin(2*pi*linspace(0,100,100));
196 y_pipe = y0 + R*cos(2*pi*linspace(0,100,100));
197 z_pipe = zeros(1,100);
198
199 xyz_pipe = [x_pipe;y_pipe;z_pipe];
200 xyz_pipe_rotated = roty(Fallpipe_angle-90)*xyz_pipe;
201
202 xyz_pipe_rotated(1,:) = xyz_pipe_rotated(1,:) + Pipe_start_x + sind(Fallpipe_angle)*D_pipe/2;
203 xyz_pipe_rotated(3,:) = xyz_pipe_rotated(3,:) + cosd(Fallpipe_angle)*D_pipe/2;
204
205 plot3(xyz_pipe_rotated(1,:),xyz_pipe_rotated(2,:),xyz_pipe_rotated(3,:),'k','LineWidth',2); axis
      equal;
206
207 %(Fallpipe length)
208 x1 = [0 Pipe_start_x];
209 y1 = [0 0];
210 z1 = [-Pipe_start_x*tand(Fallpipe_angle) 0];
211
212 plot3(x1,y1,-z1,'k','LineWidth',2)
213 plot3(x1 + sind(Fallpipe_angle)*D_pipe,y1,-z1 + cosd(Fallpipe_angle)*D_pipe,'k','LineWidth',2)
214
215 plot3(x1 + sind(Fallpipe_angle)*D_pipe/2,y1+D_pipe/2,-z1 + cosd(Fallpipe_angle)*D_pipe/2,'k','
      LineWidth',2)
216 plot3(x1 + sind(Fallpipe_angle)*D_pipe/2,y1-D_pipe/2,-z1 + cosd(Fallpipe_angle)*D_pipe/2,'k','
      LineWidth',2)
217
218 % Drawing Bed height and width of the pipe
219
220 Beta_width = D_pipe/2*sqrt(2*(1-cos(pi-2*theta)))/2;
221
222 x_beta_height = [Pipe_start_x + sind(Fallpipe_angle)*Beta_height,  Pipe_start_x + sind(Fallpipe_angle
      )*Beta_height];
223 y_beta_height = [Beta_width, -Beta_width];
224 z_beta_height = [cosd(Fallpipe_angle)*Beta_height, cosd(Fallpipe_angle)*Beta_height];
225
226 plot3(x_beta_height,y_beta_height,z_beta_height,'b')
227
228 % Draw monopile
229
230 if Monopile==1
231     x_monopile = Pipe_start_x+Radius_monopile+sind(60)*D_pipe+Safety_Margin + Radius_monopile*sin(
          linspace(0,-pi,100));
232     y_monopile = y0 + Radius_monopile*cos(linspace(0,-pi,100));
233     z_monopile = zeros(1,100);
234
235     %plot3(x_monopile,y_monopile,z_monopile,'m','LineWidth',8)
236     hold on
237
238     [Xm,Ym,Zm]=cylinder(2,1000);
239     x_mp_center = Pipe_start_x+Radius_monopile+sind(60)*D_pipe+Safety_Margin;
240     surf(Xm+x_mp_center,Ym,Zm*(Box(3,2)-Box(3,1))+Box(3,1))
241 end
242
243  %% Discretized
244 for j=1:No_of_stones
245
246     x_s=0; y_s=0; z_s=0;  u_sx=0; u_sy=0; u_sz=0; t_turb=0; t_eddie=0;
247     t_cross=0; count=0; T_SSM=0; count_SSM=0; u_randx=0; u_randy=0;
248     v_rand=0;
249
250     x_s(1) = RStonesxyz(1,j);
251     y_s(1) = RStonesxyz(2,j);
252     z_s(1) = RStonesxyz(3,j);
253
254     w = gamma*sqrt(rho_r *d*g/Cd_ver(j));
```

```
255
256     if I_startloc == 0
257         x_s(1) = 5;
258         y_s(1) = 0;
259         z_s(1) = 0;
260     end
261
262     if I_startloc == 0.5
263         x_s(1) = 5 + (Beta_height*sind(Fallpipe_angle))/2;
264         y_s(1) = 0;
265         z_s(1) = (Beta_height*cosd(Fallpipe_angle))/2;
266     end
267
268     index1 = interp1(X,1:length(X),x_s(1),'nearest');
269     index2 = interp1(Y,1:length(Y),y_s(1),'nearest');
270     index3 = interp1(Z,1:length(Z),z_s(1),'nearest');
271
272     v0 = -INITIAL_velocity*sind(Fallpipe_angle) + v_w(index2,index1,index3)*EH; % Outlet velocity
         VERTICAL + Fluid velocity
273     u0x = INITIAL_velocity*cosd(Fallpipe_angle) + u_wx(index2,index1,index3)*EH; % Initial HORIZONTAL
          x velocity
274     u0y = u_wy(index2,index1,index3); % Initial HORIZONTAL y velocity
275
276     u_sx(1)=u0x;
277     u_sy(1)=u0y;
278     v_s(1)=v0;
279
280         for i=2:N
281
282             T_Lk(i,1) = 0.30*k(index2,index1,index3)/eps(index2,index1,index3); %Lagrangian integral
                  time
283             T_Lk(i,2) = k(index2,index1,index3);
284             T_Lk(i,3) = eps(index2,index1,index3);
285
286             index1 = interp1(X,1:length(X),x_s(i-1),'nearest');
287             index2 = interp1(Y,1:length(Y),y_s(i-1),'nearest');
288             index3 = interp1(Z,1:length(Z),z_s(i-1),'nearest');
289
290             U = sqrt((u_wy(index2,index1,index3)-u_sy(i-1))^2 + (u_wx(index2,index1,index3)-u_sx(i-1)
                  )^2 + (v_w(index2,index1,index3)-v_s(i-1))^2);
291
292             if count_SSM >= T_SSM       % When one timestep of the random walk model is finished,
                  start a new path.
293
294                 w = gamma*sqrt(rho_r *d*g/Cd_ver(j));       % Terminal velocity
295                 a_SSM = lambda*(rho_f/rho_s)*CL(j)*(w^2)/d; % Horizontal acceleration due to the lift
                       force
296                 u_SSM = dt*a_SSM *I_SSM;                    % Absolute horizontal velocity SSM
297
298                 R_SSM_uniform = rand(1)*2*pi;
299                 u_SSMx = cos(R_SSM_uniform) * u_SSM;
300                 u_SSMy = sin(R_SSM_uniform) * u_SSM;
301
302                 v_SSM = I_SSM*w;
303                 T_SSM = 2*pi*d/(St*w(1));
304
305                 count_SSM = 0;
306             end
307
308                 T_L = (1/4) * 0.30*k(index2,index1,index3)/eps(index2,index1,index3);   % Lagrangian
                       integral time
309                 r_uniform = rand(1);                                                    % Uniform
                       random number between 0 and 1 (from CHOI 2007)
310                 t_eddie = -T_L*log(r_uniform);                                          %
                       Characteristic time scale
311
312                 tau = (d^2 * rho_s) / (18*kvisc*rho_f);
```

```
313                 le = (C_mu^0.75 * k(index2,index1,index3)^1.5) / eps(index2,index1,index3);
314                 t_cross = -tau * log(1-(le/(tau*abs(U))));
315
316                 pit(i,1) = t_eddie;
317                 pit(i,2) = t_cross;
318                 pit(i-1,3) = t_turb;
319
320             if count >= t_turb
321                 u_checkx = u_randx;
322                 u_checky = u_randy;
323                 v_check = v_rand;
324
325                 t_turb = min(t_eddie,t_cross);
326                 R_rand_uniform = rand(1)*2*pi;
327                 u_rand = normrnd(0,sig) * sqrt(2*k(index2,index1,index3)/3);
328
329                 u_randx = cos(R_rand_uniform) * u_rand;
330                 u_randy = sin(R_rand_uniform) * u_rand;
331
332                 v_rand = normrnd(0,sig) * sqrt(2*k(index2,index1,index3)/3);
333                 count = 0;
334             end
335
336         v_s(i) = HS*((As*Cd(j)*rho_f*abs(U)*((v_w(index2,index1,index3) + v_rand) - v_s(i-1)))/8 -
                V*(rho_s-rho_f)*g) * dt/(M+Ma) + v_s(i-1);
337         u_sx(i) = ((As*CL(j)*rho_f*abs(U)*((u_wx(index2,index1,index3) + u_randx + u_SSMx) -u_sx(i
                -1)))/2) * dt/(M+Ma) + u_sx(i-1);
338         u_sy(i) = ((As*CL(j)*rho_f*abs(U)*((u_wy(index2,index1,index3) + u_randy + u_SSMy) -u_sy(i
                -1)))/2) * dt/(M+Ma) + u_sy(i-1);
339
340         x_s(i) = x_s(i-1) + u_sx(i)*dt;
341         y_s(i) = y_s(i-1) + u_sy(i)*dt;
342         z_s(i) = z_s(i-1) + v_s(i)*dt;
343
344         if Monopile == 1
345             [ab,bc] = min(abs(y_s(i)-y_monopile));
346
347             if x_s(i) >= x_monopile(bc)
348
349                 I1 = atand(y_s(i)/(abs(x_s(i)-x_mp_center)));
350                 I2 = atand((y_s(i)-y_s(i-1))/(x_s(i)-x_s(i-1)));
351
352                 Theta = I1+I2;
353
354                 I3 = 2*Theta - I2;
355
356                 U_s = sqrt(u_sx(i)^2 + u_sy(i)^2);
357
358                 U_sx = U_s * cosd(Theta + I3);
359                 U_sy = U_s * sind(Theta + I3);
360
361                 v_s(i)= CoR*v_s(i);
362                 u_sx(i) = -CoR*U_sx;
363                 u_sy(i) = CoR*U_sy;
364
365                 x_s(i)= x_s(i-1);
366                 y_s(i)= y_s(i-1);
367             end
368         end
369
370         if z_s(i) >= Lz
371             time = dt*(i-1);
372         end
373
374         if z_s(i) <= Lz
375             r(j,1) = x_s(i-1);
376             r(j,2) = y_s(i-1);
```

```
377                 r(j,3) = z_s(i-1);
378                 r(j,4) = u_sx(i-1);
379                 r(j,5) = u_sy(i-1);
380                 r(j,6) = v_s(i-1);
381                 r(j,7) = U;
382                 r(j,8) = time;
383                 r(j,9) = St*h/(2*pi*d);
384                 r(j,10)= time/T_SSM;
385                 break
386             end
387 
388             count = count+dt;
389             count_SSM = count_SSM+dt;
390         end
391 
392     figure(1);
393     title(['Stone number: ',num2str(j),' '])
394     hold on
395     plot3(x_s,y_s,z_s,'-.')
396 
397     end
398     axis([Box(1,:) Box(2,:) Box(3,:)])
399     %axis([-0.70 0.70 -0.70 0.70 -h 0])
400 
401     % Table containing stone values at the seabed
402     Seabed_stones = table(r(:,1),r(:,2),r(:,3),r(:,4),r(:,5),r(:,6),r(:,7),r(:,8),r(:,9),r(:,10), '
            VariableNames', {'x [m]' 'y [m]' 'z [m]' 'ux [m/s]' 'uy [m/s]' 'v [m/s]' 'U [m/s]' 't [s]' 'N (
            approx) [-]' 'N (calc) [-]'});
403     %%
404     %figure()
405     hold on
406     xslice = [];
407     yslice = [];
408     zslice = [];
409     slice(xq,yq,zq,U_w,xslice,yslice,zslice)
410 
411     view([0 0])
412 
413      %% Stone distribution
414         figure()
415         hold on
416         grid on
417         plot(r(:,1),r(:,2),'o')
418         plot(mean(r(:,1)),mean(r(:,2)),'x','MarkerSize',12,'LineWidth',2)
419         plot(Pipe_start_x,0,'*','MarkerSize',12,'LineWidth',2)
420         plot(xyz_pipe_rotated(1,:),xyz_pipe_rotated(2,:),'--')
421         title('Stone distribution at sea bed')
422         xlabel('x [m]')
423         ylabel('y [m]')
424         legend('Stones',strcat('Mean: x =',num2str(round(mean(r(:,1)),2)),' y =',num2str(round(mean(r
                (:,2)),2))),'Bottom of the fallpipe','Projected fallpipe on the seabed')
425         if Monopile == 1
426             plot(x_monopile,y_monopile,'--')
427             legend('Stones',strcat('Mean: x =',num2str(round(mean(r(:,1)),2)),' y =',num2str(round(mean(r
                    (:,2)),2))),'Bottom of the fallpipe','Projected fallpipe on the seabed','Monopile')
428         end
429         axis([5.0000 10.7990 -2.2869 2.2869])
430         %axis equal
431 
432     %% Particle interaction time
433     figure()
434     hold on
435     plot(pit(:,1))
436     plot(pit(:,2))
437     plot(pit(:,3),"_")
438 
```

```
439 legend('Characteristic lifetime $\tau_e$','Eddy crossing time $t_{cross}$','Minimum time scale used',
        'interpreter','latex')
440 xlabel('time steps [n]','interpreter','latex')
441 ylabel('Time scale [s]','interpreter','latex')
442 title('Particle interaction times at each time step $n$','interpreter','latex')
443
444 %% Bivariate histogram
445 figure()
446 hh = scatterhist(r(:,1),r(:,2),'Location','NorthEast',...
447                  'Direction','out',...
448                  'Color','k',...
449                  'LineStyle',{'-'},...
450                  'Marker','o',...
451                  'MarkerSize',4);
452 %axis([-0.70 0.70 -0.70 0.70])
453 axis square
454 xlabel('x-axis [m]','interpreter','latex')
455 ylabel('y-axis [m]','interpreter','latex')
456 legend('Stones')
457 legend boxoff
458 grid on
459
460 %% Cumulative Rayleigh distribution
461 %{
462 dev_x = r(:,1)-mean(r(:,1));
463 dev_y = r(:,2)-mean(r(:,2));
464
465 dev = sort(sqrt((dev_x).^2 + (dev_y).^2));
466
467 Rayleighcdf = raylcdf(dev,mean(dev)/1.623);
468
469 figure()
470 plot(dev,Rayleighcdf)
471 xlabel('deflection [m]','interpreter','latex')
472 ylabel('Fr [-]','interpreter','latex')
473 title('Rayleigh distribution validation')
474 grid on
475
476 std(dev);
477 0.685*sqrt(h*d);
478
479 mean(r(:,8))/T_SSM;
480 r(1,9);
481 %}
482 %% Normal distribution
483
484 dev_x = r(:,1)-mean(r(:,1));
485 dev_y = r(:,2)-mean(r(:,2));
486
487 dev = sort(sqrt((dev_x).^2 + (dev_y).^2));
488
489 Mean_normal = mean(dev);
490 SD_normal = std(dev);
491
492 dev_norm = normpdf(dev,Mean_normal,SD_normal);
493
494 figure()
495 hold on
496 plot(dev,dev_norm)
497 histogram(dev,'Normalization','pdf')
498 xlabel('Displacement [m]','interpreter','latex')
499 ylabel('Fr [-]','interpreter','latex')
500 title('Normal distribution dispersion')
501 grid on
502 %% Histogram with fit normal distribution
503  figure()
504  hold on
```

```
505  nbins = 10;
506  %h = histogram(r(:,1),nbins)
507  histfit(r(:,1))
508
509 %% Stone velocity vectors at the seabed
510 figure()
511 quiver3(r(:,1),r(:,2),r(:,3),r(:,4),r(:,5),r(:,6))
512 title('Stone velocity vectors at the seabed')
513 xlabel('x [m]')
514 ylabel('y [m]')
515 zlabel('z [m]')
516 axis equal
517
518 %% Histogram 3D
519 figure()
520 histogram2(r(:,1),r(:,2), 20)
521 %% Density scatter plot
522 figure()
523 d = densityScatterChart(r(:,1),r(:,2), "XLabel", "x [m]", "YLabel", "y [m]", "Title", "Density
      scatter chart");
524 d.DensityExponent = 2;
525
526 %% Slice represetation of the fluid field created in OpenFOAM
527 figure()
528 hold on
529 xslice = [];
530 yslice = [0];
531 zslice = [];
532 slice(xq,yq,zq,v_w,xslice,yslice,zslice)
533 view([0 0])
534
535 %% Saving Figures
536 %{
537 figHandles = findall(0, 'Type', 'figure');  % Get handles of all open figures
538
539 if Monopile == 0
540     figure(figHandles(4));  % Switch focus to the figure
541     saveas(gcf, fullfile('Ambient current',['Current' UU num2str(SIM) 'ms side.png']));  % Save the
          figure as PNG
542
543     figure(figHandles(3));  % Switch focus to the figure
544     saveas(gcf, fullfile('Ambient current',['Current' UU num2str(SIM) 'ms top.png']));  % Save the
          figure as PNG
545
546     figure(figHandles(2));  % Switch focus to the figure
547     saveas(gcf, fullfile('Ambient current',['Current' UU num2str(SIM) 'ms histogram.png']));  % Save
          the figure as PNG
548
549     figure(figHandles(1));  % Switch focus to the figure
550     saveas(gcf, fullfile('Ambient current',['Current' UU num2str(SIM) 'ms normal dist.png']));  %
          Save the figure as PNG
551 end
552
553 if Monopile == 0
554     figure(figHandles(4));  % Switch focus to the figure
555     saveas(gcf, fullfile('Monopile results',['SIM' num2str(SIM) 'side.png']));  % Save the figure as
          PNG
556
557     figure(figHandles(3));  % Switch focus to the figure
558     saveas(gcf, fullfile('Monopile results',['SIM' num2str(SIM) 'top.png']));  % Save the figure as
          PNG
559
560     figure(figHandles(2));  % Switch focus to the figure
561     saveas(gcf, fullfile('Monopile results',['SIM' num2str(SIM) 'histogram.png']));  % Save the
          figure as PNG
562
563     figure(figHandles(1));  % Switch focus to the figure
```

```
564     saveas(gcf, fullfile('Monopile results',['SIM' num2str(SIM) 'normal dist.png']));  % Save the
            figure as PNG
565 end
566 %}
567
568 %% Saving mean values
569
570 fprintf('Mean_r = %s\n',Mean_normal)
571 fprintf('SD_r = %d\n',SD_normal)
572
573 fprintf('Mean_dev_x = %s\n',mean(r(:,1)))
574 fprintf('SD_dev_x = %d\n',std(r(:,1)))
575
576 fprintf('Mean_y = %s\n',mean(r(:,2)))
577 fprintf('SD_y = %d\n',std(r(:,2)))
578
579 dev_x = r(:,1)-mean(r(:,1));
580 dev_y = r(:,2)-mean(r(:,2));
581
582 dev = sort(sqrt((dev_x).^2 + (dev_y).^2));
583
584 Mean_normal = mean(dev);
585 SD_normal = std(dev);
586
587 Dispersion(number,:) = ([Mean_normal SD_normal mean(r(:,1)) std(r(:,1)) mean(r(:,2)) std(r(:,2))]);
```